UNIVERSITÀ DEGLI STUDI DI GENOVA

SCUOLA POLITECNICA

TESI DI LAUREA IN INGEGNERIA MECCANICA
ENERGIA E AERONAUTICA

Physical analysis of the electroactive morphing effects around a supercritical wing at high Reynolds number by means of High-Speed PIV

Supervised by:

Prof. Alessandro Bottaro
Dr. Marianna Braza (IMFT)
Dr. Johannes Scheller (IMFT)

Author:

Marco Tonarelli
Mat. 3720455

2015/2016

Physical analysis of the electroactive morphing effects around a supercritical wing at high Reynolds number by means of High-Speed PIV

Contents

Abstract

The need to improve the aerodynamic performance of air vehicles is the origin of intense research on the real-time optimization of the wing shape instead of the actual fixed wing design with discrete control surface like flap and slat. This real time optimization can be achieved by morphing the airfoil using adequate materials and actuators (Smart-Materials).

The object of this thesis is to study how this type of actuator could modify the performance optimization on different time scales (low-frequent and high-frequent actuation).

The effect of the distinct actuation types, low-frequent large-displacement shape memory alloys (SMAs) and high-frequent low-displacement piezoelectric, on the flow past a prototype wing are analysed using particle image velocimetry (PIV) measurement.

The designed prototype NACA 4412 airfoil, with embedded surface actuated SMAs and trailing edge MFC piezo-actuator, has been tested in the wind tunnel.

The PIV measurement conducted behind the piezoelectrically actuated trailing edge showed that the actuation interact with flow and leads to a reduction of the shear-layer instabilities modes and the loss of momentum past the wing. An optimum actuation frequency at 60 Hz has been identified.

The experiment also showed the deformation capacity of the SMA technology under realistic aerodynamics loads.

Sommario

La necessità di incrementare le performance aerodinamiche dei velivoli è alla base di un'intensa ricerca, in particolare riguardo l'ottimizzazione in tempo reale della forma del profilo alare ad oggi caratterizzato da un design fissato e superfici di controllo discrete come flap e slat. L'ottimizzazione in tempo reale può essere effettuata deformando il profilo alare utilizzando particolari materiali e attuatori detti Smat-Materials.

L'obbiettivo di questa tesi è di studiare come questo tipo di attuatori possono modificare le performance aerodinamiche relativamente a due scale temporali differenti, una a bassa frequenza e con elevato spostamento ottenuta attraverso SMAs ed una ad alta frequenza con piccolo spostamento realizzata da attuatori piezoelettrici.

Il prototipo studiato, basato su un profilo NACA 4412, è caratterizzato da attuatori SMA inseriti al di sotto della superfice che ne modificano la curvatura e degli attuatori piezoelettrici (MFC) al bordo di uscita. Il prototipo è stato studiato in galleria del vento, in particolare con misure di velocità a valle del profilo, in corrispondenza del bordo di uscita, utilizzando un Particle Image Velocimetry (PIV).

I risultati ottenuti mostrano come l'attuazione ad alta frequenza interagisce con il flusso riducendo la turbolenza e la perdita di quantità di moto causata dalla scia. A seguito dei risultati ottenuti è stata individuata una frequenza ottimale di 60 Hz. Inoltre gli esperimenti hanno dimostrato la capacità degli attuatori SMAs di sopportare carichi aerodinamici reali.

Introduction

For thousands of years, humans have been observing birds from the ground with interest. This curiosity to understand how birds are able to fly in the air has motivated humans' desire to fly, and ultimately the development of airplanes. Since birds are the source of inspiration for airplane development, airplanes should, supposedly, look more like birds in order to become more energy efficient. However, airplanes today look quite different from birds in many aspects particularly in the wing shape as shown in Figure 1.1.

Figure 1.1: Differences in appearance between a bird wing and an airplane wing

Airplanes can achieve better efficiency if they can "behave" more like birds in flight, and morphing technology makes it possible.

Today the airplanes have a conventional fixed-wing design. Nowadays these rigid, fixed wing airfoil geometries are usually the results of a design compromise optimizing the shape for some parts of the mission profile. Control surfaces are used to adapt the aerodynamic profile of the wing to the current mission segment.

While these control surfaces are certainly able to modify the aerodynamic characteristics of the wing and extending the mission profile, they are usually characterized by poor aerodynamic performance and efficiency. Morphing wing hold the potential to solve this problem by changing the shape significantly in order to fulfill different mission requirement in flight.

Bird are the best example of morphing at work, they change their wing structure in flight to perform specific manoeuvres. The change in wing-shape allow the bird to reduce the drag, thus increasing its energy efficiency. Through the morphing wing technology, airplanes are able to behave more similarly to birds, which improve their performance in different flight conditions.

The idea of morphing wing is far from new. In 1903, the Wright brothers emulated the flight of the birds and developed the idea of wing warping, which used pulleys and cables to warp the wings to make turns and provide roll control, essential ability to stabilize an airplane after getting disturbed by external force such as wind (Figure 1.2).

The technique was then abandoned as soon as metals substituted fabric and became the primary material for airplanes, as metals did not have the flexibility of a fabric wing.
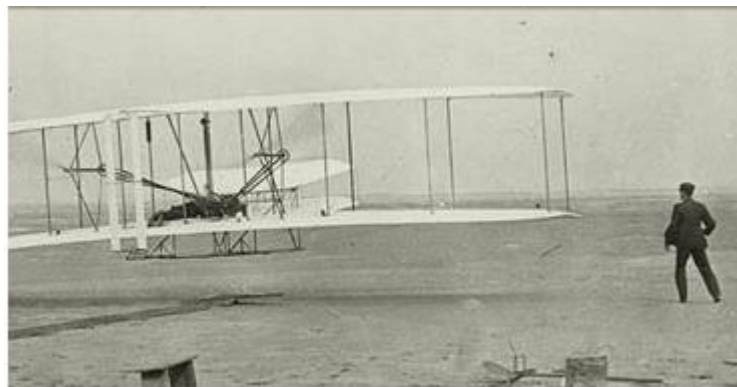
Figure 1.2: The 1903 Wright Flyer

Today with the development of the Smart-Material the wing warping idea surfaced again and morphing wings have the potential to revolutionize aircraft design. The main benefit of morphing wings is to reduce drag and noise and improve energy efficiency.

This work has been conducted during a stage at Istitut de Meanique des Fluides de Toulouse (IMFT) in the research group EMT2 under the supervision of Dr. Marianna Braza and Dr. Johannes Scheller.

Chapter 1. Electroactif materlials

1.1 Shape memory alloys

Shape memory alloys (SMAs) are a unique class of metallic materials with the ability to recover their original shape after being heated above a specific temperature (shape memory effect). They are characterized by thermo-mechanical coupling in which heating induces a phase transformation of the crystalline structure of the materials.

The material is able to return to its original geometry, even after reaching large inelastic deformations, near 10 % strain. Furthermore, an increase temperature can result in shape recovery ever under high applied loads, which results in high actuation energy densities. In these cases, the actuation mechanism is controlled by the heating process.

The shape recovery is associated with the existence of two stable crystalline phases, each stable at a high or low temperature, respectively Austenite and Martensite, the reversible phase transformation between these two crystal structures is the basis for the material behaviour.

The temperature at which the alloy recovers its shape can be modified by small changes in composition of the materials and through heat treatments (Table 1.1).

Alloy	Composition	Transformation range (°C)
Ag-Cd	44-49 % Cd	-190 to - 50
Au-Cd	46.5-50 % Cd	30 to 100
Cu-Al-Ti	14-41.5 % Au; 3-4.5 % Ni	-140 to 100
Cu-Au-Zn	23-28 % Au; 45-47 % Zn	-190 to 40
Cu-Sn	15 at. % Sn	-120 to 30
Cu-Zn-Al	3-8% Al 4-6% Al; 22-28% Zn	0 to 150 Room temperature
In-Ti	18-23 % Ti	60 to 100
Ni-Al	36-38 % Al	-180 to 100
Ni-Ti	49-51 % Ni	-50 to 110
Fe-Pd	30 % Pd	-100
Mn-Cu	5-35 % Cu	-250 to 180
Fe-Mn-Si	32 % Mn; 6 % Si	-200 to 150
Fe-Pt	25 % Pt	-130

Table 1.1: Typical SMA alloy.

1.1.1 SMAs thermo-mechanical behaviour and phase transformations

Shape memory alloys are characterized by a solid state phase transformation, in which both the starting phase (or parent phase, called Austenite) and the final phase (or product phase, called Martensite) are solid structures, although with different crystallographic arrangements.

These two phases consist of a body-centered cubic structure for Austenite, and a face-centered cubic structure for Martensite. The transformation between these phases is known as the 'martensitic thermoplastic transformation'. Due to the different crystalline structure, Austenite behaves like many metals and has higher Young's modulus, whereas the Martensite phases behaves more like an elastomer, with lower stiffness and large 'plateau' in its stress-strain curve.

The stable phase at any moment depends on the temperature, applied mechanical loads and thermos-mechanical history of the material.

The crystal structure of Martensite is obtained from austenite following the application of mechanical load or a decrease in temperature. Then, by heating or reducing the load, the Austenite phase is recovered.

Also by varying the temperature in absence of applied loads, the phase of the material changes. The SMA composition is expressed in terms of the fraction of Martensite (ξ). In particular, before cooling, the material will start from a single phase composition of 100% Austenite (with $\xi=0$) to reach a condition of co-existence of both the phases in different proportions, and finally a 100% Martensite phase (with $\xi=1$).

As result of this transformation, the macroscopic mechanical behaviour of SMA can be separated in two categories:

- The 'shape memory effect' (SME) in which an SMA exhibits a large residual strain, and after increasing the temperature the alloy can completely recover this residual deformation.

- The 'pseudo-elastic' effect in which the SMA exhibits a very large deformation that can be recovered by means of hysteretic loop when unloading.
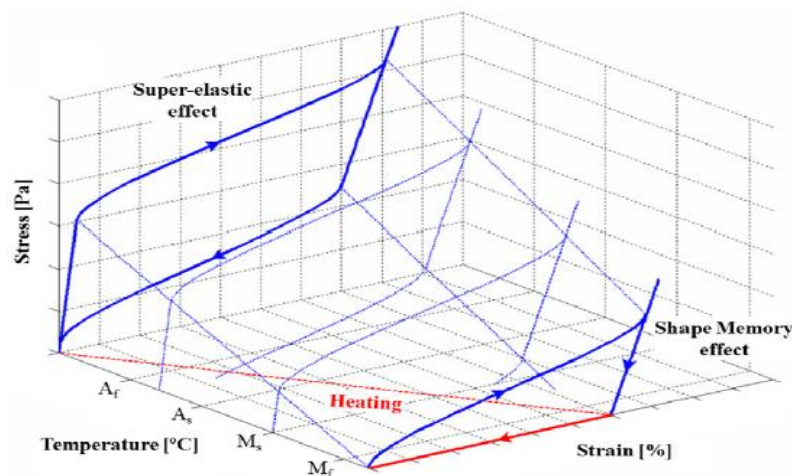
Figure 1.1: SMA stress-strain behaviour [S. Barbarino et al.,2014]

The fist property (SME) is particularly useful and is due to the specific crystalline structure of the Martensite phase, which is the typical phase of the Austenite at low temperature.

It consist in a dense arrangement of crystal planes placed with an opposite orientation and with a very high relative mobility. When the material is loaded above the yield point in Martensite phase the crystal phase gradually unfold the lattice accommodating the strain without significant atomic displacements. This phenomenon is called 'detwinning' (Figure 1.2).
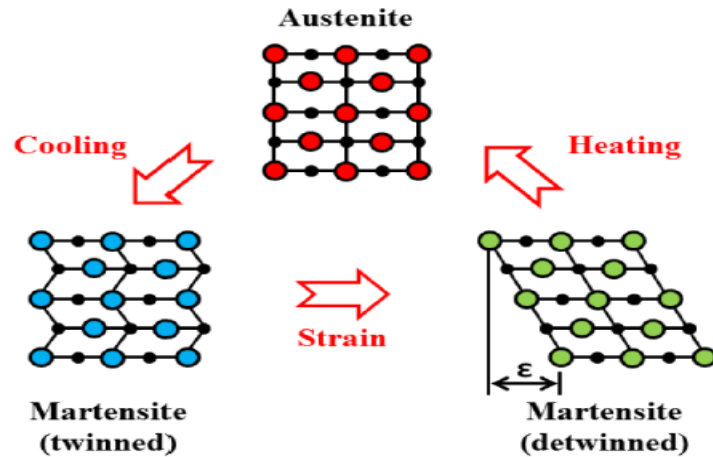
Figure 1.2: Microscopic phenomenology associated with the SME effect [S. Barbarino et al.,2014]

The second property, pseudo-elesticity, of the martensitic transformatin is related to the possibility of a phase transformation occurring by applying a suitable stress state under appropriate temperature condition, $T>A_f$).

The alloy can reach the same higly deformable crystalline structure during the application of an external force, directly going from austenite phase to the deformed martensite phase, without permanently damaging the crystal structure. Compared to the previsous case there is no twinned martendite phases (generated due to temperature decrease).
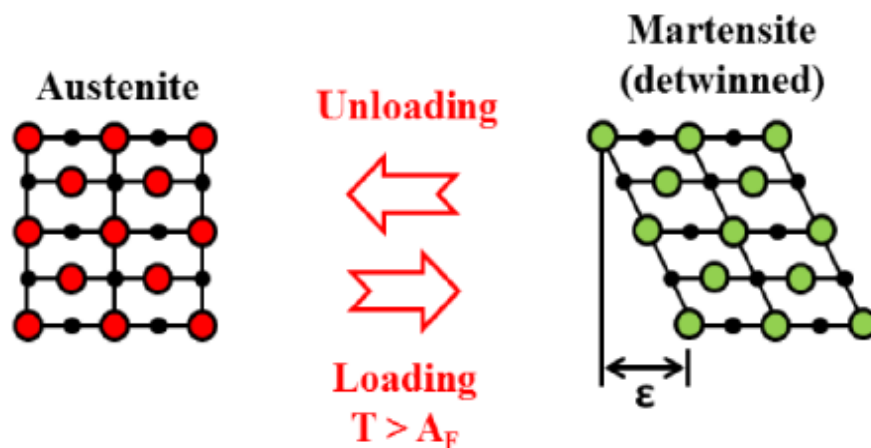
Figure 1.3 : Microscopic phenomenology associated with the pseudoelastic effect. [S. Barbarino et al.,2014]

However, since the phase transformation occours in a temperature range where the martensite phase is not stable (T>Af where the only stable phase in austenite), as soon as the external force is removed the alloy reverts instantly to the parent phase, promoting an immediate shape recovery.

Both the effect, SME and pseudoelasticity, can be summarized in the same stress-strain diagram (Figure 1.4).
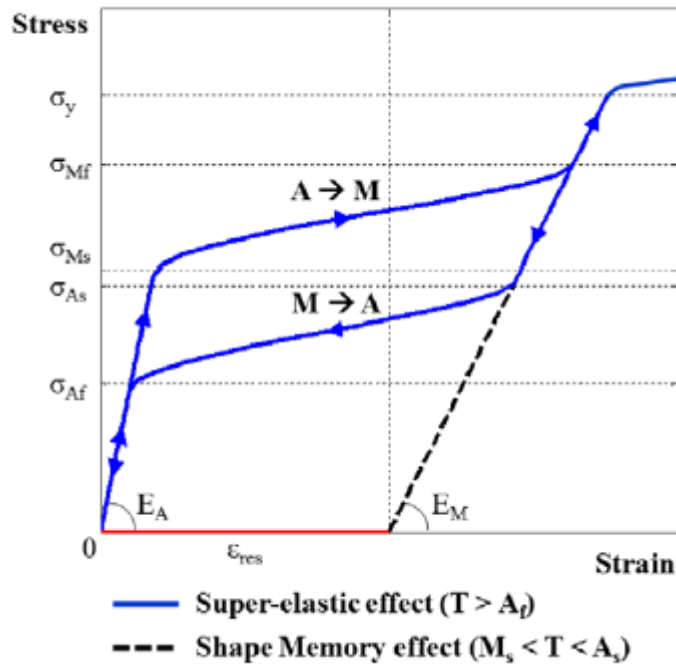
Figure 1.4: Typical SMA stress-strain diagram [S. Barbarino et al. , A review on shape memory alloys]

The pseudoelastic effect can be observed for a SMA at a temperature T>Af, which is represented by the solid line. The SME is shown as a segmented line.

Aditionally, the shape memory effect can be of two diffenret types:

- One-way shape memory
- Two-way shape memory

The first category refers to the material for which a deformed shape must be imposed and upon thermal activation the initial configuration is attained.

The second category relates to those materials that can 'remember' two shape, each of which can be retrieved at different temperature, without requiring an applied deformation. The two-way shape memory effect is usually achieved with SMAs that exhibit lower mechaincal properties and also have lower performance as actuator.

As SMAs are both capable of creating high stresses and strain they seems to be an ideal candidate material to be used in electric actuators. The phase transformation from Martensite to Asustenite can be induced by heating the material via electrical resistive heating exploiting the Joule effect. Than the Austenite-Martensite phase transformation can be achieved by cooling down the mateial.

4

For instance, the NiTi SMA alloy displays one of the highest work density at $10 \, ^J/_{cm^3}$ (see Table 1.2), which is a factor of 25 times greater than the work density of electric motors and is able to lift more than 100 times of its weight.

NiTi SMA alloy is the choice for designers for actuators that provide significant displacement and forces.

Actuator Type	Stress (MPa)	Strain (%)	Efficiency (%)	Bandwidth (Hz)	Work per Volume (J/cm³)	Power per Volume (W/cm³)
NiTi SMA	200	10	3	3	10	30
Piezoceramics	35	0.2	50	5000	0.035	175
Single crystal piezoelectric	300	1.7	90	5800	2.55	15000

Table 1.2: Comparison of actuator performance.

1.1.2 Constitutive models for SMAs

Many constitutive models have been developed to describe the thermomechanical behaviour of SMA materials. Some are based primarily on micromechanics, others on a combination of micro and macromechanics (SMA phenomenology), statistical mechanics or kinetic methods.

The first and most popular one-dimensional model is due to Tanaka. In this model the second law of thermodynamics is written in terms of the Helmhotz free energy in variational form. Here, it is assumed that the mono-axial deformation ε, temperature T and volume fraction of martensite ξ are the only state variables.

The constitutive equation is expressed as:

$$(\sigma - \sigma_0) = E(\xi)(\varepsilon - \varepsilon_0) + \theta(T - T_0) + \Omega(\xi)(\xi - \xi_0) \qquad (1.1)$$

Where the subscript 0 represents the initial condition. This equation shows that the total stress, $(\sigma - \sigma_0)$, is constituted by three quantities. There are the mechanical stress, $E(\xi)(\varepsilon - \varepsilon_0)$, the thermos-plastic stress, $\theta(T - T_0)$, and the stress induced by the phase transformation, $\Omega(\xi)(\xi - \xi_0)$. Moreover the Young's module E and the phase transformation coefficient Ω are function of the martensite volume fraction ξ. These are expressed as:

$$E(\xi) = E_A + \xi(E_M - E_A) \quad \text{and} \quad \Omega(\xi) = -\varepsilon_L \cdot E(\xi) \qquad (1.2)$$

Where ε_L is the maximum recoverable strain, and E_A and E_M represent the Young's moduli for the austenite and martensite phases. For the martensite volume fraction was developed an evolutionary equation, determined by the dissipation potential, which depend on the stress σ and the temperature T in an exponential equation:

$$\text{A} \rightarrow \text{M transformation (cooling): } \xi = 1 - \exp[a_M(M_S - T) + b_M \sigma] \qquad (1.3)$$

$$M \rightarrow A \text{ transformation (heating): } \xi = \exp[a_A(A_S - T) + b_A\sigma] \qquad (1.4)$$

The material constant are defined as:

$$a_A = \frac{\ln(0.01)}{(A_S - A_f)} \qquad\qquad b_A = \frac{a_A}{C_A} \qquad (1.5)$$

$$a_A = \frac{\ln(0.01)}{(A_S - A_f)} \qquad\qquad b_A = \frac{a_A}{C_A} \qquad (1.6)$$

The adopted coefficients E, θ and Ω, together with the parameters M_S, M_f, A_S, A_f, C_A, and C_M, are usually experimentally determined.

One of the major limitations of this simple model is that it only describe the stress-induced martensitic transformation (pseudo-elastic effect) and do not consider the transformation induced by strain (shape memory effect). Therefore they can't be applied to model the detwinning of Martensite that is responsible of the SME at low temperature.

1.2 Piezoelectric materials

The piezoelectric effect describes the capacity of certain materials to produce an electric charge under the application of mechanic stress. This is also called 'direct' piezoelectricity and was discovered in 1880 by brothers Curie.

The 'converse' effect, the deformation of the material when exposed to an electric field, was proven in 1881 by Lippman.

The piezoelectric effect is exhibited by a number of naturally-occurring crystal, for instance quartz, tourmaline and sodium potassium tartrate, and these have been used for many year as electromechanical transducers.

For a crystal to exhibit the piezoelectric effect, its structure should have no centre of symmetry. A stress (tensile or compressive) applied to such a crystal will alter the separation between the positive and negative charge sites in each elementary cells leading to a net polarization at the crystal surface. The effect is practically linear, i.e. the polarization varies directly with the applied stress, and direction-dependent, so that compressive and tensile stresses will generate electric fields and hence voltages opposite polarity. This effect it's also reciprocal, so that if the crystal is exposed to an electric field, it will experience an elastic strain causing its length to increase or decrease according to the field polarity. Besides the crystal mentioned above, an important group of piezoelectric materials are the piezoelectric ceramics, of which the lead zirconate titane (PZT) is an example. These are polycrystalline ferroelectric materials with a tetragonal/rhombohedral structure very close to a cubic.

Whereas these materials can be manufactured in large quantities, they not possess piezoelectric properties in their natural state. A polarization process is required in order to train the material, and this is done by application of a large electric field at a temperature below the Curie temperature (T_c) which leads to a realignment of the dipoles in the material. After removing the electric field the dipoles remain locked in position and a permanent polarization of the material is achieved (see Figure 1.5).

(a) unpolarised material   (b) polarization process by an electric field   (c) polarized material
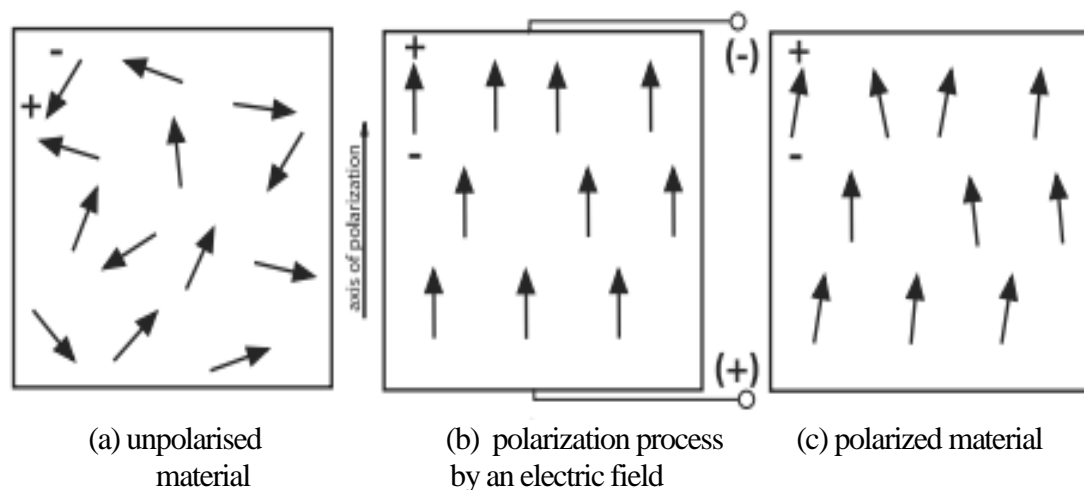
Figure 1.5: Polarization of a piezoelectric ceramic

1.2.1 Piezoelectric constitutive equation

The electromechanical properties of piezoelectric material is governed by linear equation based on the IEEE standard for piezoelectricity. It turns out that at low electric fields and at low mechanical stress levels piezoelectric materials have a linear profile.

The constitutive equation describing the piezoelectric properties are based on the assumption that the total strain is the sum of mechanical stress and controllable actuation strain caused by the applied electric voltage.

The describing electromechanical equations for a linear piezoelectric material are the follow:

$$\varepsilon_p = s_{pq}^E + d_{ip}E_i \tag{1.7}$$

$$D_i = d_{ip}\sigma_p + \epsilon_{ij}^\sigma E_j \tag{1.8}$$

where the index $i,j = 1\ldots3$ and $p,q = 1\ldots6$ refer to a different direction within the material coordinate system. The corresponding symbol and unit are given in Table 1.3.

Whereas the equations are given in matrix form, the majority of the actuators are using the d_{33} or d_{31} mode of actuation, defining the three direction refers to the direction of polarization. The piezoelectric coefficient d_{ij} are definite as the ratio of strain in the j-axis due to the electric field applied along the i-axis.

Property	Symbol	Unit
Strain	ε_p	$\dfrac{\Delta l}{l}$
Stress	σ_p	Pa
Electric field	E_i	$\dfrac{V}{m}$
Elastic compliance at constant electric field	s_{pq}^E	$\dfrac{1}{Pa}$
Piezoelectric change constant	d_{ip}	$\dfrac{m}{V}$
Constant electric displacement	D_i	$\dfrac{C}{m^2}$
Dielectric coefficient at constant stress	ϵ_{ij}^σ	-

Table 1.3: Symbol definitions for piezoelectric equations.

1.2.2 Principal piezoelectric materials

PZT   Lead zirconate titanate is an intermetallic inorganic compound, also called PZT, it is a ceramic perovskite material that shows a marked piezoelectric effect, meaning that the compound is used in a number of practical applications in the area of electroceramics. PZT is a white solid that is insoluble in all solvents. Exhibit a small active strain but a large maximum stress of 110 MPa, and PZT is capable to reach large actuation frequencies up to 100KHz.

PZT can be distinguished into hard and soft ceramic depending on the application type, whereas hard ceramic are used for application requiring a large electric field (i.e. actuator) and soft ceramics are mainly applied in low power application (i.e. sensor).

Piezoelectric polymers   The properties of polymers (Polyvinylidene fluoride PVDF) are very different from those of inorganics (see Table 1.4), and they are uniquely qualified to fill niche areas where single crystals and ceramics cannot perform as effectively. As noted in Table 1, the piezoelectric strain constant ($d31$) for the polymer is lower than that of the ceramic. However, piezoelectric polymers have much higher piezoelectric stress constants ($g31$) which indicates that they are much better sensors than ceramics.

Material	$d_{31}{}^a$, [pm/V]	$g_{31}{}^a$, [(mV·m)/N]	K_{31}	Salient features
PVDF Polyvinylidene flouride	28	340	0.12	Flexible, lighweight, low mechanical impedance
PZT Lead zirconium titane	175	11	0.34	Brittle, heavy, toxic

Table 1.4: Comparison of properties of standard piezoelectric polymer and ceramic materials

In contrast to PZT, PVDF and its copolymer require for a similar strain level a far larger electric field. In addition, PVDF react opposite to PZT, when PZT would elongate due to an electric field PVDF contracts. The major advantage of PVDF is the lower density of about $1470\,Kg/m^3$ compared to 7600 Kg/m^3 of PZT. The maximum stress is only 4.8 MPa.
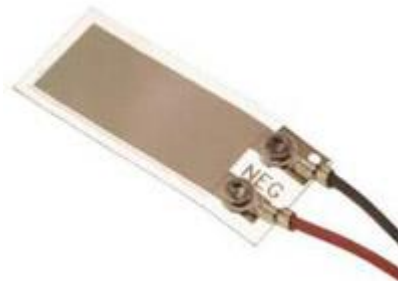
Figure 1.6: Example of PVDF actuator

Piezoelectric composites One inconvenient of using monolithic ceramics is there relatively fragile nature. Nevertheless their superior piezoelectric properties make them a preferred choice when compared to piezoelectric polymers.

This issue is tackled using piezoelectric fiber composite (PFCs) capable of generating large strain with a good blocking force. The nowadays commercial available composites are macro fiber composites (MFCs) that are the combination of PFCs and IDEs.

The PCFs are made of round piezoelectric fibers embedded into an epoxy matrix, actuation was achieved using the d_{31} mode of actuation. This construction allows to direct deformation along the direction of the fibres allowing a great flexibility. The inconvenient of this design was the reduced sustainable electric field. Contrariwise the IDEs allow to use the significantly higher d_{33} actuation coefficient.

Figure 1.7: MFC applied to the trailing edge of wing model
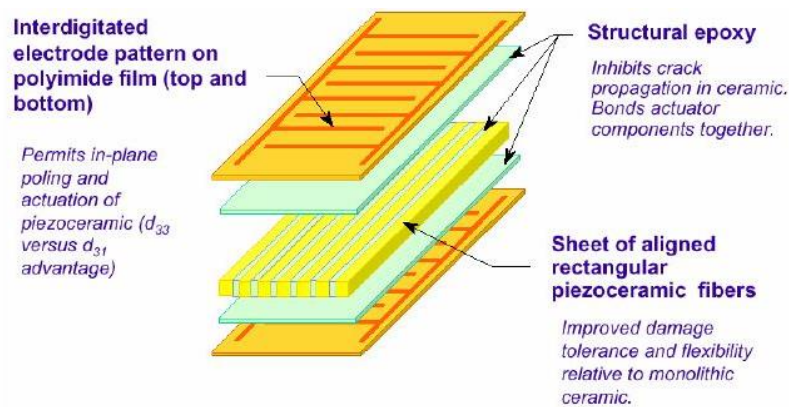
Figure 1.8: Schematic showing the order of different layers in the MFC actuator

1.3 Smart-materials comparison

This section introduces different smart-materials and provided an overview of their capacities, advantage and disadvantage. An interesting aspect is to compare the performance of the different materials to each other in terms of achievable stress and strain, actuation energy density and actuation frequency (see Figure 1.9).
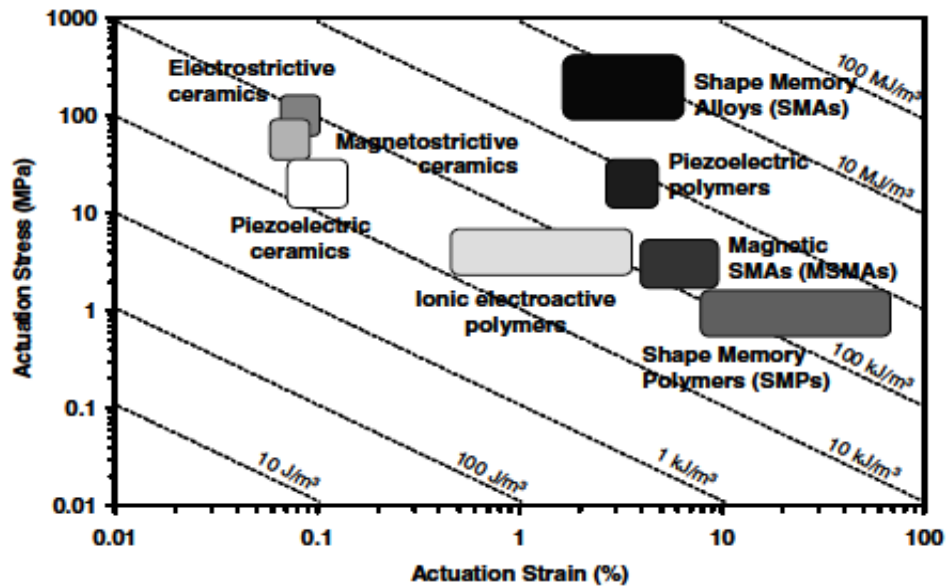
Figure 1.9: Actuation energy density diagram indicating typical ranges of actuation stress, actuation strain, and the actuation energy densities of different active materials [Lagoudas, 2008]

As can be seen in Figure 1.9 shape memory materials provide large actuation strain, whereas piezoelectric materials provide a limited amount of deformation but a stress level comparable with SMAs.
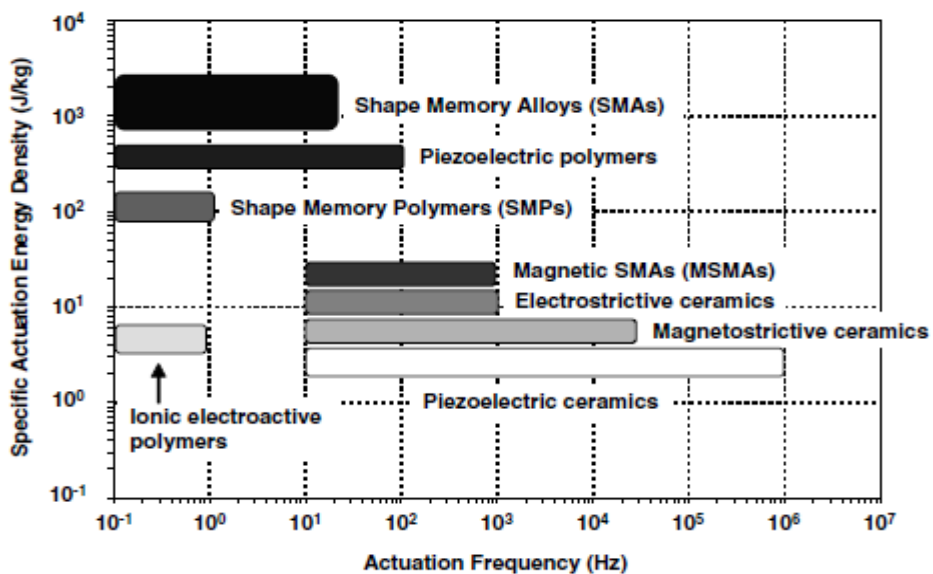
Figure 1.10: Actuation energy density vs. actuation frequency for typical material [Lagoudas, 2008]

As one can see in Figure 1.10, whereas the specific actuation energy density of SMAs is quite large they are limited to a low actuation frequency, on the other hand piezoelectric materials are capable to achieve high actuation frequency.

Based on the comparison done in Figure 1.9 and 1.10, two main materials groups can be distinguished, that are able to sustain elevated actuation stresses necessary to change the shape of an airfoil during lift under aerodynamic load:

- Smart-materials capable of a large displacement at limited actuation frequencies (SMA)

- Smart-materials capable of elevated actuation frequencies with limited displacement (Piezoelectric)

SMAs materials due to their elevated energy density but slow response time provide characteristics exploited for quasi-static shape control (camber deformation of the airfoil). On the other hand, piezoelectric actuation can be used in order to act on the higher frequency but small scale displacement (high frequency trailing edge actuation).

Material	Advantages	Inconveniences
SMAs	● large stress and strain	● limited actuation frequency ● isolation of outside temperature necessary ● large hysteresis
Piezoelectric ceramics	● large stress actuation frequency ● easy voltage based control ● low power consumption	● non-linearity at larger electric fields ● hysteresis ● limited strain ● risk of depolarization

Table 1.5 Comparison of smart-material advantages and inconveniences

1.3.1 Smart-materials for aeronautical application

The unique properties of the smart materials have gathered in aeronautical applications, which are subjected to high dynamic loads and geometric space constraints. Figure 1.11 shows all the possible application of smart materials on commercial aircrafts.
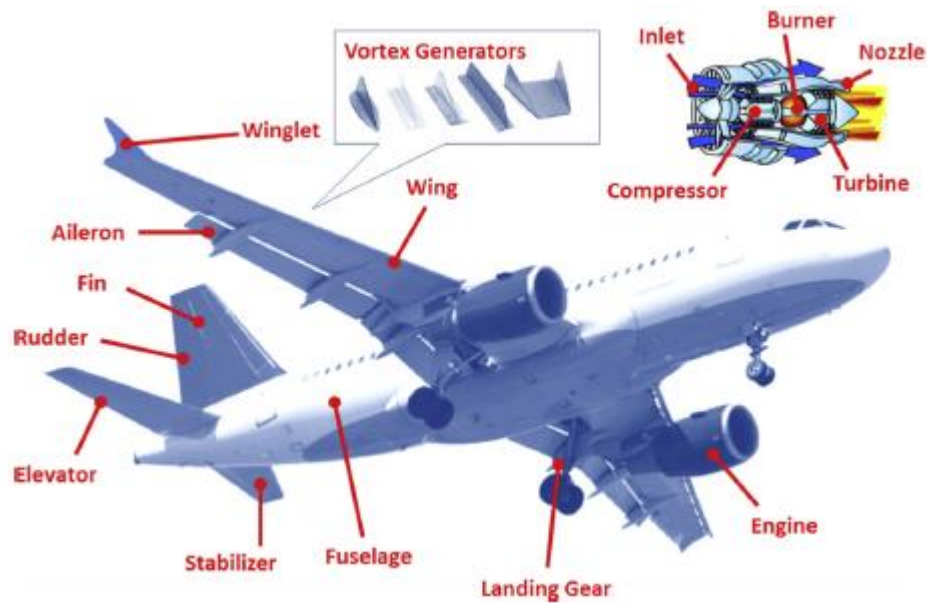
Figure 1.11: Existing and potential applications in the aerospace domain [J. M. Jani,A review of shape memory alloy research, applications and opportunities]

In particular for the wings application two different type of actuation can be differentiate:

- quasi-static control in order to optimize the lift over drag ratio and adapt the airfoil profile to the current mission

- dynamic shape control to act on the aeroelastic coupling coefficient and reduce both noise and drag

Today fixed wings airfoil are usually the result of a design that compromise optimizing the shape only for some parts of the mission profile. Control surface while modifying the aerodynamic profile of the wing are usually characterized by poor aerodynamic performance and efficiency (i.e. flap and slat). The object of the quasi-static shape control is to modify the airfoil shape according to the mission profile without the losses induced by discrete control surface. The modification of the wing shape (see Figure 1.12) leads to a modification of the lift to drag ratio, an increase of curvature leads to an increase of $L/_D$.
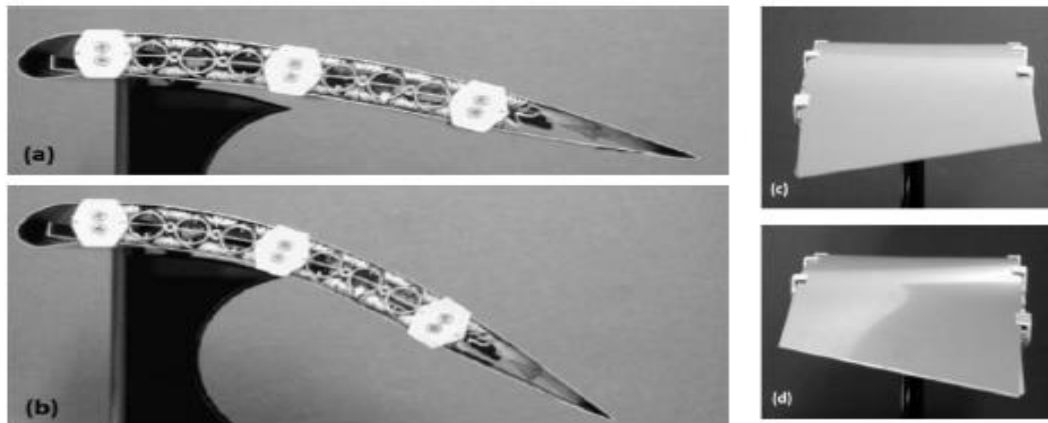
Figure 1.12: Wing morphing with SMA actuators, (a) (b) chord-wise bending and (c) (d) wing section twisting [Elzey et al., 2003]

In addition to the previously discussed function of adapting the airfoil shape in function of the current mission profile smart-materials actuated wings can also fulfill new and supplementary functions such as to modify the shape of the wing in 3D generating a twist (see Figure 1.12a d) or a spanwise bending which might be interesting for certain flight conditions.

Regarding the control of the airfoil shape at high frequencies, it should be noted that the inherent notion of dynamic shape control at elevated frequencies disqualifies SMAs actuator for these applications duo to their slow actuation frequency. The obvious choice in this case are piezoceramic based actuator due to their comparable energy density and high actuation frequencies (see Figure 1.9 and Figure 1.10).

I.e. Munday and Jacob [2002] used piezoelectric actuators in dynamic regime in order to control the separation over a NACA4415 airfoil. The test conducted at low Reynolds number shows that a significant reduction of the separation area can be achieved (see Figure 1.13). This separation reduction is potentially capable of a significant drag reduction.

In general high frequency actuation leads to a reduction of the drag at around 10%, and the attenuation of the vortex shedding could leads also to a reduction of the noise (as can be seen in the follow chapters).

| (a) 0° at 0 Hz oscillation | (b) 0° at 1.7 Hz oscillation |

| (c) 9° at 0 Hz oscillation | (d) 9° at 5 Hz oscillation |
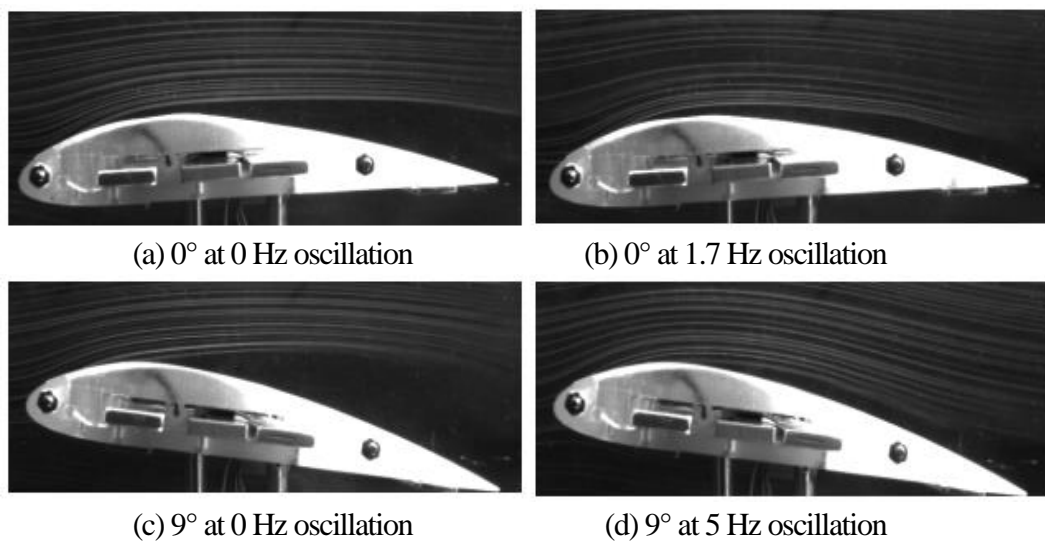
Figure 1.13 Oscillating camber wing [Munday and Jacob, 2002]

Chapter 2. Measurement technique

2.1 The particle image velocimetry method

Particle image velocimetry (PIV) is a non-intrusive optical technique, which allows to visualize the velocity in a plan of a fluid to be simultaneously measured throughout a region illuminated by a two-dimensional light sheet.

'Seeding' flow following particles are introduced into the flow and their motion used to estimate the kinematics of the local fluid. The tracers particles are chosen to be near neutrally buoyant and to efficiently scatter light.

These particles have to be illuminated in a plane of the flow at least twice within a short time interval. The light scattered by the particles has to be recorded either on a single frame or on a sequence of frames. The particle displacement between consecutive image can be determined through cross-correlation. In order to be able to handle the great amount of data which can be collected employing the PIV technique, sophisticated post-processing is required.
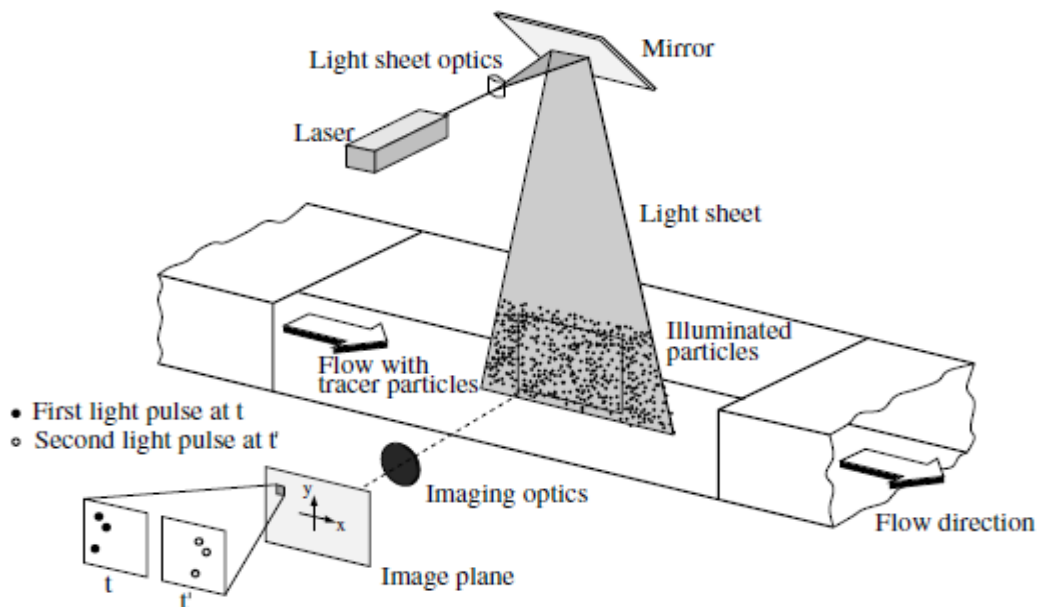
Figure 2.1: Experimental arrangement for particle image velocimetry in a wind tunnel [Raffel et al.,2007]

Figure 2.1 briefly sketches a typical setup for PIV recording in a wind tunnel. Small tracer particles are added to the flow. A plane (light sheet) within the flow is illuminated twice by means of a laser (the time delay between pulses depending on the mean flow velocity and the magnification at imaging). It is assumed that the tracer particles move with local flow velocity between the two illuminations. The light scattered by the tracer particles is recorded via a high quality lens either on a single frame (e.g. on a high-resolution digital camera).

The illumination is most commonly provided by a laser, shaped into a planar 'sheet' using cylindrical lenses. An advantage of using a laser is that many lasers have a pulsed output with a pulse duration and a repetition rate making them suitable as a strobe-scopic illumination source.

For evaluation, the digital PIV recording is divided in small subareas called "interrogation areas". The local displacement vector for the images of the tracer particles of the first and second illumination is determined for each interrogation area by means of statistical methods (auto- and cross-correlation).

It is assumed that all particles within one interrogation area have moved homogeneously between the two illuminations. The projection of the vector of the local flow velocity into the plane of the light sheet (two-component velocity vector) is calculated taking into account the time delay between the two illuminations and the magnification at imaging. The process of interrogation is repeated for all interrogation areas of the PIV recording.

Some general aspects of the PIV are discussed in the following:

- **Non-intrusive velocity measurement.** In contrast to techniques for the measurement of flow velocities employing probes such as pressure tubes or hot wires, the PIV technique being an optical technique works non-intrusively. This allows the application of PIV even in high-speed flows with shocks or in boundary layers close to the wall, where the flow may be disturbed by the presence of the probes.
- **Indirect velocity measurement.** PIV technique measures the velocity of a fluid element indirectly by means of the measurement of the velocity of tracer particles within the flow, which – in most applications – have been added to the flow before the experiment starts. In two phase flows, particles are already present in the flow. In such a case it will be possible to measure the velocity of the particles themselves as well as the velocity of the fluid (to be additionally seeded with small tracer particles).
- **Whole field technique.** PIV is a technique which allows to record images of large parts of flow fields in a variety of applications in gaseous and liquid media and to extract the velocity information out of these images. This feature is unique to the PIV technique.
  The spatial resolution of PIV is large, whereas the temporal resolution is limited due to current technological restrictions. Instantaneous image capture and high spatial resolution of PIV allow the detection of spatial structures even in unsteady flow fields.
- **Velocity lag.** The need to employ tracer particles for the measurement of the flow velocity requires us to check carefully for each experiment whether the particles will faithfully follow the motion of the fluid elements, at least to that extent required by the objectives of the investigations. Small particles will follow the flow better.
- **Illumination.** For applications in gas flows a high power light source for illumination of the tiny tracer particles is required in order to well expose the photographic film or the video sensor by scattered light. However, the need to utilize larger particles because of their better light scattering efficiency is in contradiction to the demand to

have as small particles as possible in order to follow the flow faithfully. In most applications a compromise has to be found.

- **Duration and time delay of illumination pulse.** The duration of the illumination light pulse must be short enough to "freeze" the motion of the particles during the pulse exposure in order to avoid blurring of the image ("no streaks"). The time delay between the illumination pulses must be long enough to be able to determine the displacement between the images of the tracer particles with sufficient resolution and short enough to avoid particles with an out-of-plane velocity component leaving the light sheet between subsequent illuminations.

- **Distribution of tracer particles in the flow.** For PIV a homogeneous distribution of medium density is desired for high quality PIV recordings in order to obtain optimal evaluation. No structures of the flow field can be detected on a PIV recording of high quality.

- **Number of components of the velocity vector.** Due to the planar illumination of the flow field only two (in plane) components of the velocity vector can be determined in standard two-component PIV (2C-PIV). Methods are available to extract the third component of the velocity vector as well (stereo techniques, dual plane PIV and holographic recording which itself is three-dimensional). This would be labelled 3C-PIV. Both methods work in planar domains of the flow field (2D-PIV).

- **Temporal and spatial resolution.** Most PIV systems allow to record with high spatial resolution, but at relative low frame rates. However, the recent development of high-speed lasers and cameras allows time resolved measurements of most liquid and low-speed aerodynamic flows. The size of the interrogation areas during evaluation must be small enough for the velocity gradients not to have significant influence on the results. Furthermore, it determines the number of independent velocity vectors and therefore the maximum spatial resolution of the velocity map which can be obtained at a given spatial resolution of the sensor employed for recording.

The use of the PIV technique is very attractive in modern aerodynamics, because it helps to understand unsteady flow phenomena as, for example, in separated flows over models at high angle of attack. PIV enables spatially resolved measurements of the instantaneous flow velocity field within a very short time and allows the detection of large and small scale spatial structures in the flow velocity field.

2.1.1 Measurement concept

Particle image velocimetry is based on the calculation of particle motion through the imaging of particles using a camera. Understanding of the relationship between the observed particle motion in the measurement field and the corresponding particle image properties of the corresponding image recording is critical to the accurate representation of the flow.

In order to produce accurate PIV measurement was established a dimensionless number critical, called image density, that have a direct correlation to the probability of making a valid PIV flow measurement through image processing using auto and cross correlation techniques.

The dimensionless number is based on the calculation from the number of particles images captured in an interrogation region (N_I), and fraction of the particles that remain within interrogation region and light sheet during their displacement from the first and the second exposure.

With proper measurement conditions, the number of lost image pairs is minimized and the dimensionless number is essentially represented by the number of particle images captured in an interrogation region. It was found that for an image density greater than 10, the probability of making a valid PIV measurement approaches unity.

For PIV measurements, the number of images captured per interrogation region (N) should exceed the value of 10 to virtually eliminate the probability of an invalid correlation calculation:

$$N \geq 10 \tag{2.1}$$

There are other important parameters that can affect the quality of a measurement by PIV. In particular the particle pair loss, gradient, curvature and acceleration parameters for flow inside the interrogation region must be minimized.

The maximum velocity gradient within an interrogation region should be low enough to maintain the shape of the particle group within an interrogation region between frames. An acceptable gradient in the flow velocity for an interrogation region can be expressed as:

$$\frac{M|\Delta u|\Delta t}{d_I} < 0.05 \tag{2.2}$$

Where M is the magnification factor, Δu is the velocity gradient within the interrogation region, Δt is the time separation between frames, and d_I is the length of interrogation region the image sensor.

The magnification factor produced by the camera lens can be measured by the ratio of the interrogation region size on the image sensor to the size of the region in the measurement plane represented by the interrogation region.

$$M = \frac{d_I}{d_1} \tag{2.3}$$

The number of lost pairs between frames can be reduced by minimizing particle displacement within the interrogation region. However, the significance of displacement measurement errors are reduced with large particle displacements. As a compromise, a target particle displacement between frames relative to the interrogation region size is given by the following equation where ΔX is the particle displacement in the flow field between frames is and d_1 is the length of the interrogation region projected into the measurement plane:

$$\frac{|\Delta X|}{d_1} < 0.25 \tag{2.4}$$

The same target ratio is established as a compromise for out of plane particle loss and measurement accuracy where ΔZ is the transverse particle displacement between frames and ΔZ_0 is the laser light sheet thickness.

$$\frac{|\Delta Z|}{\Delta Z_0} < 0.25 \tag{2.5}$$

When using auto correlation processing for doubly exposed single frame images, the minimum particle displacement is critical. Displacement of particle image on CCD camera chip should be greater than twice the particle's image diameter to avoid particle superpositioning. If the particles are super-positioned on a doubly exposed image, the centre of the particle at each exposure time is indeterminable. Therefore, the minimum acceptable velocity can be established from the particle displacement give the following equitation where d_ζ is the particle image diameter.

$$\frac{M|\Delta X|}{2} < d_\zeta \tag{2.6}$$
$$d_\zeta = particle\ image\ diameter$$

The particle image diameter can be defined by the magnification factor M, and the actual particle diameter d_p:

$$d_\zeta = M d_p \tag{2.7}$$

The particle image diameter should be greater than three times the cell size on the image sensor, allowing for a sub pixel calculation the particle's center based on a Gaussian distribution of the light scattered by the particle.

2.1.3 Light sources

In PIV flow studies, illumination is usually provided by a laser sheet. A narrow sheet of light is used to define the plane of investigation.
A laser is used because can deliver a bright sheet with almost constant thickness and without aberration or diffusion, due to coherent and monochromatic character of the emitted light.
The light beam produced by a laser is usually transformed into a sheet by converging it with a weak positive lens and subsequently make the beam fan out in one plane to a sheet by an additional

cylindrical lens (Figure 1.3). This results in a sheet with a slightly converging thickness, that must be tuned to the experimental conditions.
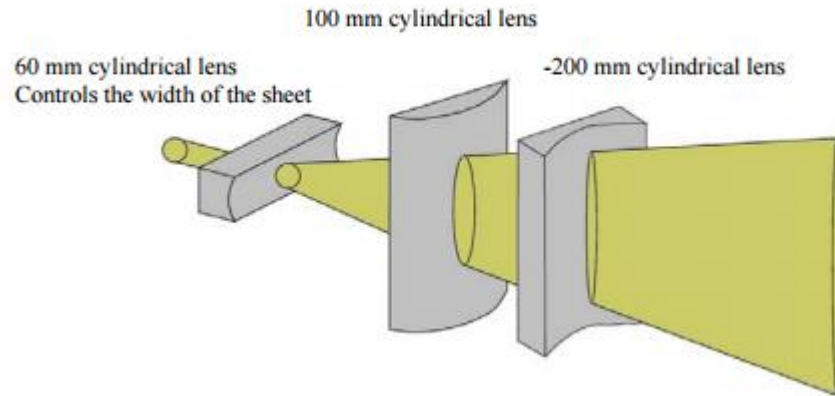
Figure 2.2: Example of a typical light sheet generating optical setup, the first lens is a diverging cylindrical lens that is used to spread the beam into a sheet. The second and third lenses are used to control the location of the beam's waist

The types of lasers used for PIV illumination can be divided in two categories: continuously emitting laser called CW (continuous weight) and pulsating lasers. The CW lasers, e.g. Helium-Neon-Argon laser, produce relatively low power light ($P_{max} = 0.01$-50 W) of a good beam quality and are easy to set up and maintain.

Pulse laser, e.g. Nd:YAG lasers (Neodymium Yttrium Aluminum Garnet), can produce higher illumination level per pulse with very short interval between two pulse. In general the pulse have a duration time of 5-10 ns and the energy in one pulse can be up to 400mJ. This laser type is highly recommended in high speed application where short illumination time and a high pulse frequency are required. Pulsed laser are usually more expensive and more difficult to set up due to added timing and synchronisation equipment compared to CW laser.

Nd:YAG lasers emit light with a wavelength of 1064 nm which is in the infrared range. For PIV-purposes light with this wavelength is not very useful since most cameras have their maximum sensitivity in the blue-green part of the spectrum. It is also disadvantageous not to be able to see the light sheet when positioning it in the measurement section. For these reasons the wavelength of the Nd:YAG laser is halved, using a device called a harmonic generator, so that it becomes 532 nm (green). The harmonic generator is not 100% efficient and therefore a separator and an IR-dump is needed to get rid of the remaining IR-light. The laser beam coming out from the laser has an axisymmetric shape which need to the shaped with a cylindrical lens in order to form a planar light sheet.
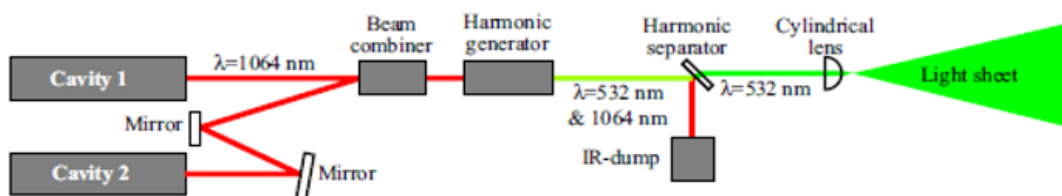
Figure 2.3: example of double cavity laser

2.1.4 PIV camera

The PIV method puts special demands on the camera the is going to be used, especially if the flow velocity is high, the image area is small and the particles are small. The first two circumstances requires the camera to be able to take two images within a short period of time in order to avoid particles pair loss.

The most common image recording devices used in indoor airflow measurements are Coupled Charged Devices (CCD) cameras and Complementary Metal Oxide Semiconductor (CMOS) cameras.

CCD cameras have been widespread used in PIV experiments for their increased spatial resolution, convenience data transmission and image processing, minimum exposure time, high light sensitivity at 532nm and low background noise. In general, a CCD element is an electronic sensor that can convert photons into electrons. A CCD sensor in the camera normally consists of an array of many individual CCD elements, which also called pixels. For example, a high-resolution CCD camera is necessary for the large-scale measurement in a full-size room, which aims to obtain the complete airflow structures. Contrarily, a high frequency CMOS camera is more suitable for studying the small-scale turbulent characteristics of airflows.

When it comes to the time-resolved (TRPIV) measurement for acquiring accurate turbulent information, using a high-speed CMOS camera is a better choice than a CCD camera. High-speed recording based on recently developed CMOS sensors even allows for acquisition in the kHz range, which is very promising for turbulence study. Using a CMOS sensor allows for the recording and handling of up to a few thousand frames per second at acceptable noise levels, but in trade of the sensor resolution.

Though as a more advanced image recording technique, the low spatial resolution has become the main obstacle for CMOS cameras to completely replace the CCD cameras. This critical drawback limits the applications of CMOS cameras only to small-scale measurements.
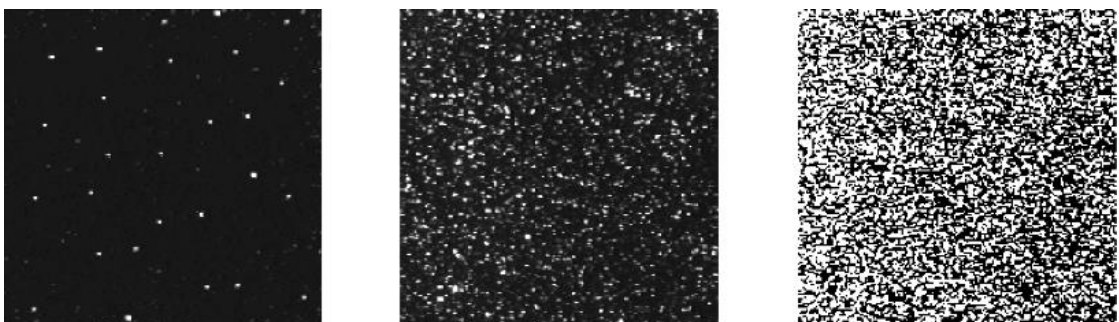
Figure 2.4: Example of PIV image and different particle density (from left to right: low density, medium density and high density).

2.1.5 Tracer particles

2.1.5.1 Fluid mechanical proprieties

PIV measurement technique is indirect as it determines the particle velocity instead of the fluid velocity. Therefore, fluid mechanical properties of the particles have to be examined in order to avoid significant discrepancies between fluid and particle motion.
The effectiveness of the particles in following the flow can be determined from a knowledge of particle dynamics in two-phase flow conditions.
Treatments of the behaviour of seeding particles use the argument of Stokes for low Reynolds's number flow around a sphere as a starting point. Particle inertial force terms are neglected and the drag force taken as:

$$D = 3\pi\mu d_p U \tag{2.8}$$

Where μ is the viscosity, d_p is the diameter of the particles sphere and U_s is the relative velocity between the sphere and the fluid (slip velocity).
A small particle moving in a fluid is described by the equation of motion, that consider only the viscous frag and not added mass and buoyancy:

$$\frac{1}{6}\pi d_p^3 \rho_p \delta = 3\pi\mu d_p U \tag{2.9}$$

$$U_s = U_p - U_f = \frac{d_p^2(\rho_p - \rho_f)}{18\mu}\delta \tag{2.10}$$

Where ρ_p is the particle density and δ is the particle acceleration. In presence of spatial or temporal gradients in the fluid the ability of the particles to follow the gradients may be estimated from this equation.
As the flow accelerates, the inertia of the particles causes a delay in their response. Comparing the slip velocity with the fluid velocity gives an estimate of the measurement error. The particles have a characteristic response time and assume the velocity of the local flow exponentially, if the density of the particle is much greater than the fluid density:

$$U_p(t) = U_f\left[1 - \exp\left(-\frac{t}{\tau_s}\right)\right] \tag{2.11}$$

With the relaxation time τ_s given by:

$$\tau_s = d_p^2 \frac{\rho_p}{18\mu} \approx \left(\frac{d^2}{\nu}\right)$$

(2.12)

If the fluid acceleration is not constant the equation of the particle motion became more difficult to solve, and the solution is no longer a simple exponential decay of the velocity. Nevertheless, τ_s remains a convenient measure for the tendency of particles to attain velocity equilibrium with the fluid.

The results of the equation is illustrated in figure, where the time response of particles with different diameters is shown for a strong deceleration in an air flow.
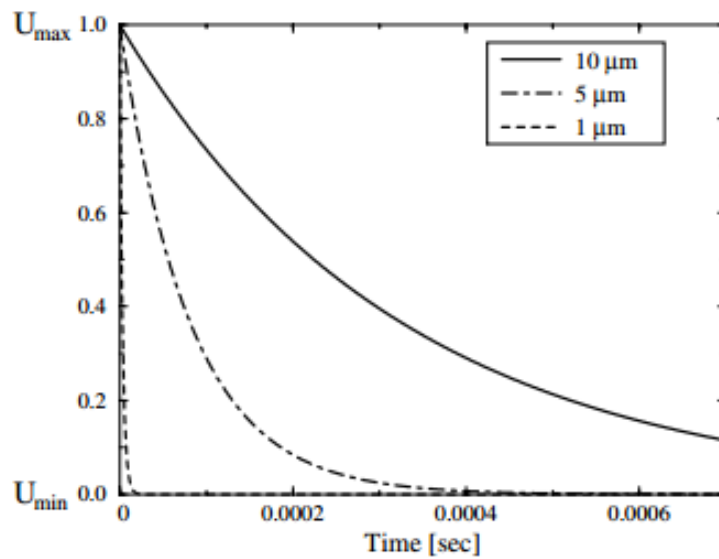
Figure 2.5. Time response of particles with different diameters in decelerating air flow.

From these equation it can be seen that due to the difference in density between the fluid and the tracer particles, the diameter of the particles should be very small in order to ensure good tracking of the fluid motion. On the other hand, the particle diameter should not be too small as light scattering properties have also to be taken into account. Therefore, it is clear that a compromise has to be found.

2.1.5.2 Light scattering behaviour

An other important characteristic of the seeded particles is the scattering behaviour. Since the obtained particle image intensity and therefore the contrast of the PIV recordings is directly proportional to the scattered light power, it is often more effective and economical to increase the image intensity by properly choosing the scattering particles than by increasing the laser power.

In general it can be said that the light scattered by small particles is a function of the ratio of the refractive index of the particles to that of the surrounding medium, the particles size, their shape and orientation. Furthermore, the light scattering also depends on polarization and observation angle. For spherical

particles with diameters, d_p, larger than the wavelength of the incident light λ, Mie's scattering theory can be applied.

The Mie scattering can be characterized by the normalized diameter, q, defined by:

$$q = \frac{\pi d_p}{\lambda} \qquad (2.13)$$

If q is larger than unity, approximately q local maxima appear in the angular distribution over the range from 0◦ to 180◦. For increasing q the ratio of forward to backward scattering intensity will increase rapidly.
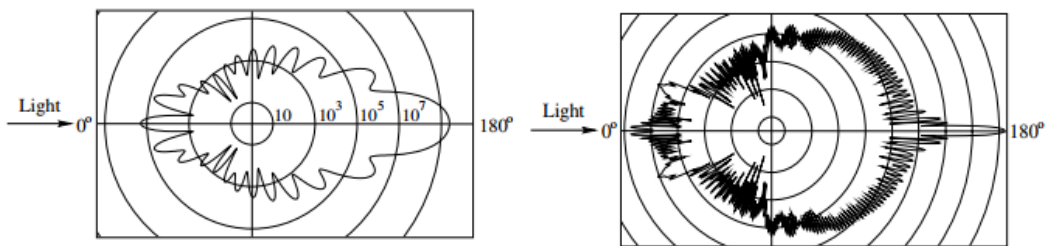
Figure 2.6: Light scattering by a 1μm particle in air (left), and by a 10μm particle (right, with the same scales).

Hence, it would be advantageous to record in forward scatter, but, due to the limited depth of field, recording at 90◦ is most often used. In general, the light scattered paraxially (i.e. at 0◦ or 180◦) from a linearly polarized incident wave is linearly polarized in the same direction and the scattering efficiency is independent of polarization. In contrast, the scattering efficiency for most other observation angles strongly depends on the polarization of the incident light. Furthermore, for observation angles in the range from 0° to 180° the polarization direction can be partially turned. This is particularly important if image separation or image shifting depending on polarization of the scattered light has to be applied. Therefore, such a technique works well only for certain particles, for example 1 μm diameter particles in air.

There is a clear tendency for the scattered light intensity to increase with increasing particle diameter(figure). However, if we recall that the number of local maxima and minima is proportional to q, it becomes clear, that the function of the light intensity versus particle diameter is characterized by rapid oscillations if only one certain observation angle is taken into account.

2.1.6 PIV analysis

The principle of the PIV analysis of a pair of images recorded successively from one illuminated plane of a particle seeded flow is depicted.

Figure 1.6 describe how the images acquisition is realized. The acquisition of the first image start at the time t_{c1} for a duration of T_1 (usually 15μs) and correspond at the fist laser pulse at the time t_{l1}.
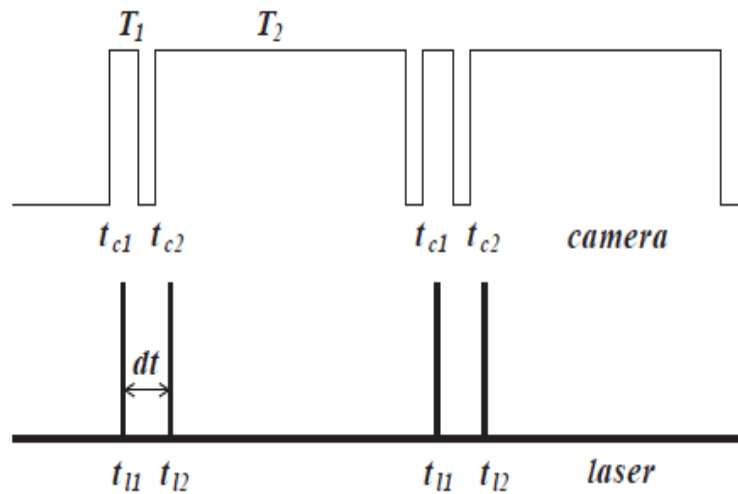
Figure 2.7: PIV chain synchronization

The second image is acquired at the time t_{c2} for a duration of T_2, that correspond at the time necessary for the acquisition of the image. The time between two next laser pulse $dt = t_{l2} - t_{l1}$ is settled by the flow speed and the dimension of the investigation area.

The steps in the analysis process are:

- Selection of area or sub-images for the analysis (interrogation windows)

- Correlation analysis

- Finding the displacement peak

- Calculating the velocity vector

- Repeat the procedure for all the sub-images

To map local flow velocity, the interrogation windows are selected containing relatively small number of particles. The probability for good analysis result is highest when the interrogation area contain about 8-10 particles image.

To get the most probable displacement of the particle pattern in the interrogation area, a mathematical correlation procedure is applied. The preferred method in PIV is to perform cross-correlation analysis, such as that as shown in Figure. First, image subsamples, $f(i,j)$ and $g(i,j)$, are extracted at the same location within the images using an interrogation window. Then, a cross-correlation procedure is performed on these two interrogated regions. This procedure results in a cross-correlation distribution with the pixel domain within the interrogated regions with a dominant peak corresponding to the shift of the particles, (Figure 2.8) designated by (dx,dy). Lastly, the pixel shift (dx,dy) is converted into a velocity through calibration parameters (see Figure 2.8d).
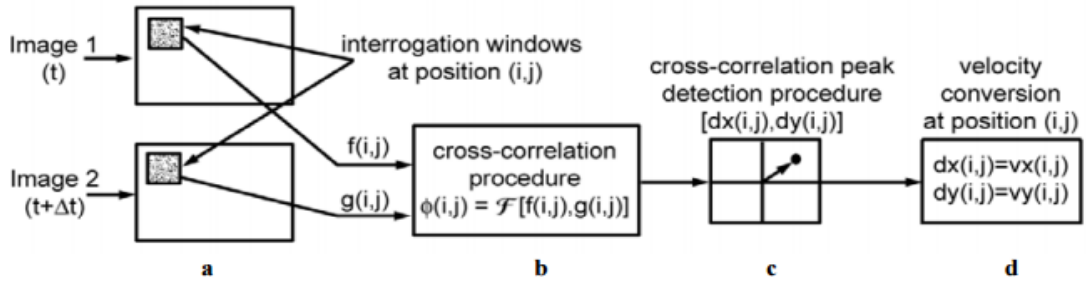
Figure 2.8: PIV analysis

The discretized cross-covariance can therefore be mathematically expressed within a discrete domain as:

$$(r,s) = \frac{1}{M*N} \sum_{m=1}^{M} \sum_{n=1}^{N} [f(m,n) - \bar{f}][g(m+r,n+s) - \bar{g}] \qquad (2.14)$$

Where $f(m,n)$ and $g(m,n)$ represent the first and the second subsampled image respectively, M and N represent the number of rows and columns within the images, $C(m,n)$ represents the discretized correlation function, (r,s) represents the location at which the correlation is calculated and $\bar{f}$ and $\bar{g}$ represent the mean image intensity of the interrogation windows, f and g respectively.

2.2 Proper orthogonal decomposition

The proper orthogonal decomposition is a procedure for extracting a basis for a modal decomposition from an ensemble of signals.

The goal of the POD is to decompose the flow in coherent structures embedded within the flow or events containing the majority of the information describing the physics of the flow. It has proven to be an effective method in identifying the dominant features in both experimental and numerical data. This procedure may be also adopted to provide a temporal reconstruction of the flow from non-time resolved, statistically independent data.

Nowadays the POD is not only used to identify coherent structures and events but also in data reduction in order to construct low-dimensional models. The key idea of the POD is to reduce a large number of interdependent variables to a much smaller number of uncorrelated variables while retaining as much as possible of the variation in the original variables, in order to reduce the computational cost and the storage requirement.

An orthogonal transformation to the basis of the eigenvectors of the sample covariance matrix is performed, and the data are projected onto the subspace spanned by the eigenvectors corresponding to the largest eigenvalues. This transformation de-correlates the signal components and maximizes variance.

From the mathematical point of view, the POD decomposes the flow U (X, t) in N spatial φ_i (X) and temporal modes a_i (t) according to their energy content as illustrated in the follow equation:

$$\bar{U}(X, t) = \sum_{i=1}^{N} \varphi_i \, (x) \cdot a_i \, (t) \tag{2.15}$$

The decomposition can be done using several methods, in this case the results are based on the Snapshots Method (suggested by [Sirovich,1987]) which is especially suitable for applications with experimental data from a PIV measurement characterized by a moderate time history and high spatial resolution.
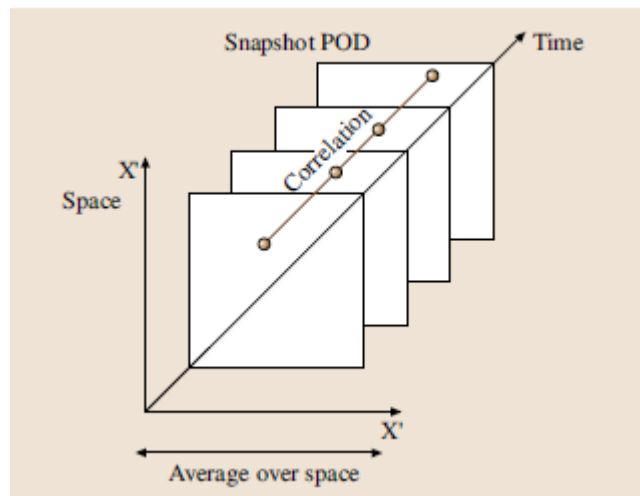
Figure 2.9: Schematic view of the snapshot POD [Kerschen et al., 2005]

Given a set of N instantaneous velocity fields (snapshots) u_i obtained via PIV, where Nx = $n_x \cdot n_y$ is the number of point in the cartesian coordinate system.

$$u_i^T = [u_1 \ u_2 u_3 \ ... \ u_{Nx} \ v_1 \ v_2 \ v_3 \ ... \ v_{Nx} \ ] \tag{2.16}$$

The problem is reduced in finding the eigenvalues $\lambda^{(k)}$ and the associated eigenvectors $\chi^{(k)}$ of a cross-correlation matrix C [N×N] defined as the surface integral of a vector field.
The advantage of this procedure is that the eigenvalues and the eigenvectors, and hence the POD modes calculated, are ordered by their energy contents.
For simplicity, the cross-correlation matrix is written for the scalar u stream-wise velocity:

$$C_{ij} = \frac{1}{N} \iint u_i(x,y)u_j(x,y)dxdy \tag{2.17}$$

In such way C is a symmetric square matrix of size [N×N]. The eigenvalues of the matrix C are then real and non-negative and its eigenvectors are orthogonal.
The k-th POD spatial mode $\varphi_u^{(k)}$ is than computed as:

$$\varphi_u^{(k)} = \sum_{i=1}^{N} \chi_i^{(k)} u_i(x,y) \tag{2.18}$$

where $\chi_i^{(k)}$ is the i-th element of the eigenvector $\chi^{(k)}$.
From a more practical point of view we can construct a snapshot matrix M that contains in each columns a instantaneous velocity field u^N :

$$M = [u^1 \ u^2 \ u^3 \ ... \ u^N] = \begin{bmatrix} u_1^1 & u_1^2 & \cdots & u_1^{N-1} & u_1^N \\ u_1^1 & u_1^2 & \cdots & u_1^{N-1} & u_1^N \\ \vdots & \vdots & \vdots & \vdots & \vdots \\ u_{Nx}^1 & u_{Nx}^2 & \cdots & u_{Nx}^{N-1} & u_{Nx}^N \\ v_1^1 & v_1^2 & \cdots & v_1^{N-1} & v_1^N \\ v_2^1 & v_2^2 & \cdots & v_2^{N-1} & v_2^N \\ \vdots & \vdots & \vdots & \vdots & \vdots \\ v_{Nx}^1 & v_{Nx}^2 & \cdots & v_{Nx}^{N-1} & v_{Nx}^N \end{bmatrix}$$

The decomposition can be performed on the correlation matrix R written as:

$$R = \frac{1}{N} M^T \cdot M \tag{2.19}$$

Then the eigenvalue problem, with λ the eigenvalues and A the matrix of eigenvectors, is given as:

$$RA = \lambda A \tag{2.20}$$

Sorting the eigenvalues in increasing mode, we can calculate the spatial modes φ_i as:

$$\varphi_i = \frac{\sum_{j=1}^{N} A_j^i u^j}{\left\| \sum_{j=1}^{N} A_j^i u^j \right\|} \tag{2.21}$$

The temporal modes now can be calculated by projecting the snapshot matrix onto the previously calculate spatial modes as:

$$a_i = \varphi_i M \tag{2.22}$$

At the end both the temporal and the spatial modes can be used in order to reconstruct a snapshot u^n :

$$u^n = \sum_{i=1}^{N} a_i \varphi_i \tag{2.23}$$

See Appendix I for the Matlab code that implement the Snapshot method for POD calculation.

Chapter 3. Experimental setup

3.1 Prototype description

The hybrid prototype is based on a NACA 4412 airfoil with a chord length of 425 mm, with embedded surface actuated SMAs and trailing edge MFC piezo-actuator.

Piezoelectric actuator based high-frequency and low-amplitude actuation in order to reduce the shear layer's turbulent energy; large-amplitude and low-frequency actuation in order to optimize the shape of the airfoil according to the current mission profile achieved using SMAs actuators.
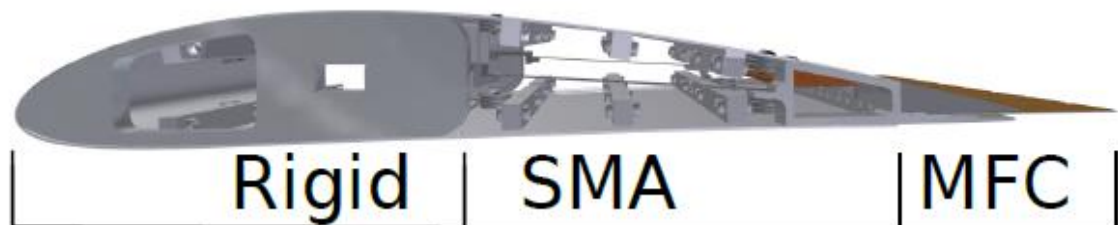
Figure 3.3: Prototype actuation concept

The actuation concept is shown in Figure 3.3, the prototype wing is made out of three distinct section. The first part accounts for the rigid leading edge of the wing. The second part, the SMA part, is being actuated by the surface distributed SMAs with large amplitude bi-directional deflection, correspond to the quasi-static camber control. The final part is the high frequency vibrating trailing edge.

The airfoil is made out of an aluminium alloy, the camber deflection cause a contraction of either intrados or extrados and the resulting differences in length that has to be compensated. This compensation is done by a sliding mechanism witch also provides the clamping of the MFCs trailing edge. The mechanism is shown in Figure 3.4. As can be seen in the figure, the distance between the sliding mechanism and the rigid part of the airfoil is fixed using a flexible centre bar that avoid the change of overall length during the bending. The intrados and the extrados are decoupled each other.

Figure 3.4: Trailing edge sliding mechanism

3.1.1 Macro-fibre composite (MFC) trailing edge actuator

In contrast to the other piezoelectric material, MFC are more flexible allowing an easier integration in the structure. They can also exploit the significantly lager d_{33} mode (as shown in the previous chapter) of piezoelectric fibres by directing the electric field along the direction of polarization, as shown in Figure 3.5.
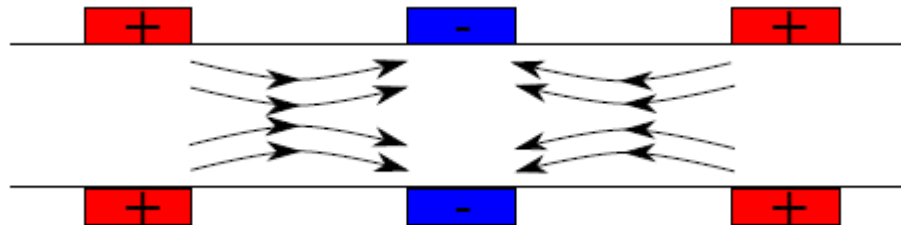
Figure 3.5: Illustration of the field in MFC

In order to guarantee a two-way actuation, is necessary a bimorph MFC type, that consist in two MFCs active layer glued on opposite side of a substrate elastic material, as illustrated in Figure 3.6.
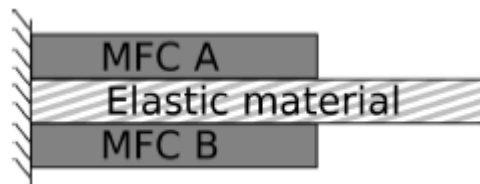
Figure 3.6: Bimorph MFC

The MFC actuator embedded at the trailing edge parallel to the intrados allow a modification of the trailing edge by $\pm$ 1 mm at the frequencies up to 100 Hz.
No strain-gauges are installed in the prototype, hence no closed-loop control of the position of the trailing edge is feasible. The trailing edge position is reconstructed by the optical PIV measurement setup.
The MFC are controlled using a rectangular signal with an amplitude of 1000 V, and the two active layer are activated with a 180° phase shift with respect to each other.

3.1.2 Shape-memory alloys

The camber control system is achieved by SMA Ni-Ti wire embedded under the surface. The activation of the SMAs induces a bending moment in the corresponding section of the airfoil skin. The insertion of SMAs wire in both the intrados and extrados have two effects: first to ensure the correct return to zero position and second to increase airfoil's control authority by not only allowing to increase but also to decrease the camber radii of curvature.

The heating of the SMAs is done by Joule effect, governed by the follow differential equation that combines Joule heating with natural convection.

$$m_{SMA}c_p\dot{T} = I^2R - h_cA_c(T - T_\infty) \qquad (3.1)$$

In this equation m_{SMA} is the mass per unit of length of the SMA wire, A_c is the surface area, I is the current applied, c_p is the specific heat, T is the temperature of the SMA, T_∞ is the ambient temperature and h_c is the coefficient of heat convection.
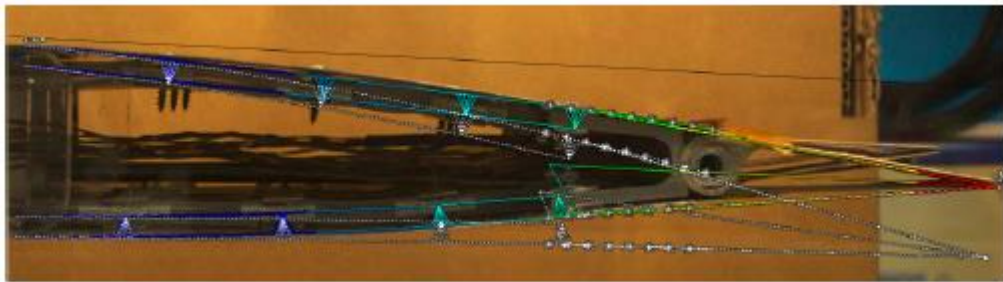
Figure 3.7: Prototype deflection

The SMAs are activated using a 3s 8A current pulse triggered at the beginning of the measurement, that enable a deformation of about 40 mm.

Figure 3.8 show the displacement of the trailing edge tracked by PIV image.
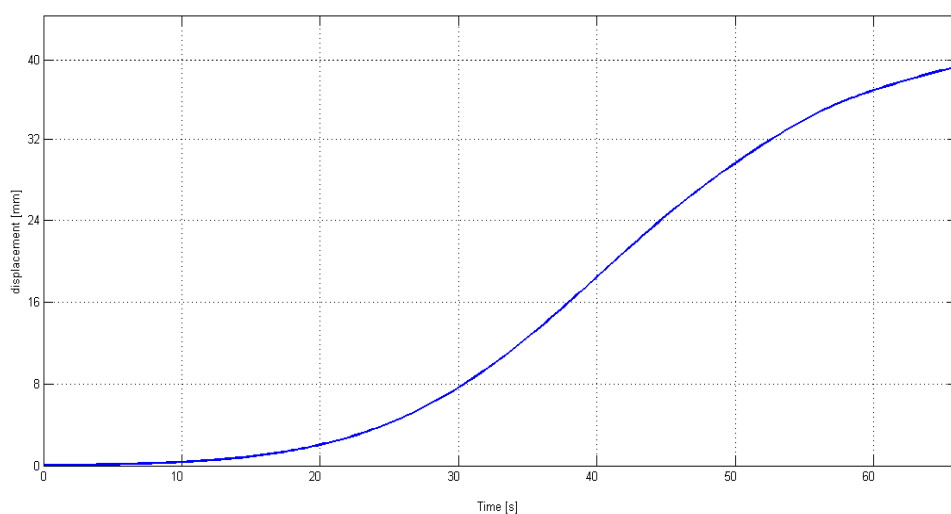
Figure 3.8: trailing edge displacement

3.2 Experimental facilities

The experiment were conducted in the S4 wind tunnel of the IMFT laboratory. It's a closed loop wind tunnel with the dimension of the test section of 670x715 mm. The upstream turbulence intensity is 0.1%.

The prototype is mounted on the transversal axis of the wind tunnel, with the flow directed along the *x*-axis.

The upstream velocity is 8 m/s, the chord length is 425 mm so the Reynolds number is about 218,000, that corresponds to a low-subsonic aileron's flight phase like landing.
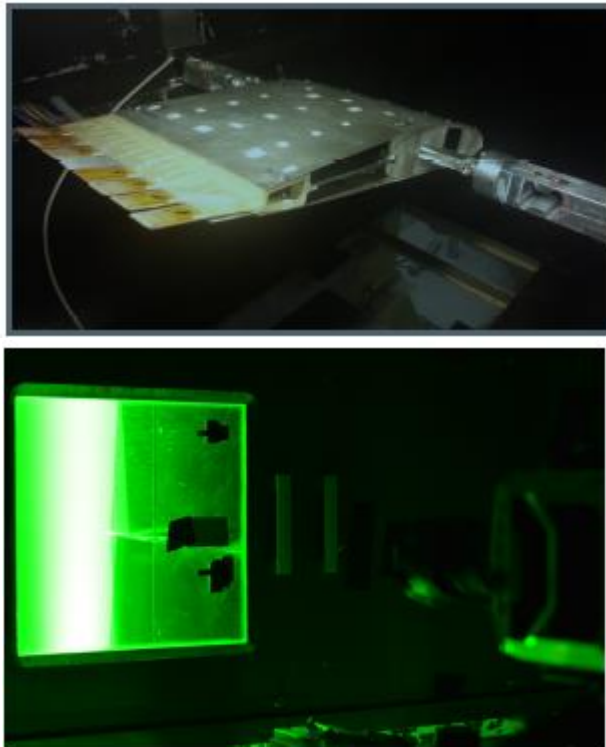
Figure 3.6: Wind tunnel installation of the prototype

In order to evaluate the effect onto the flow, the prototype is attached to a four-component strain-gauge force balance (Figure 3.6) in order to evaluate the macroscopic properties, lift and drag. In addiction Particle image velocimetry (PIV) were used to show the microscopic effect on the flow. The experimental setup is summarized in Figure 3.7.

In order to measure the velocity field by TRPIV (Time-resolved PIV) smoke particles are seeded in the wind tunnel flow by a smoke engine located in the upstream convergent part of the wind tunnel. The smoke particles diameter is about 1.5 μm. A Phantom v1210 equipped with 105 mm lens high speed camera is used to capture the particles displacement in the flow field in a measurement zone placed close to the trailing edge. The optical depth of field is focussed on the illuminated laser sheet which corresponds to the *x-y* plane.
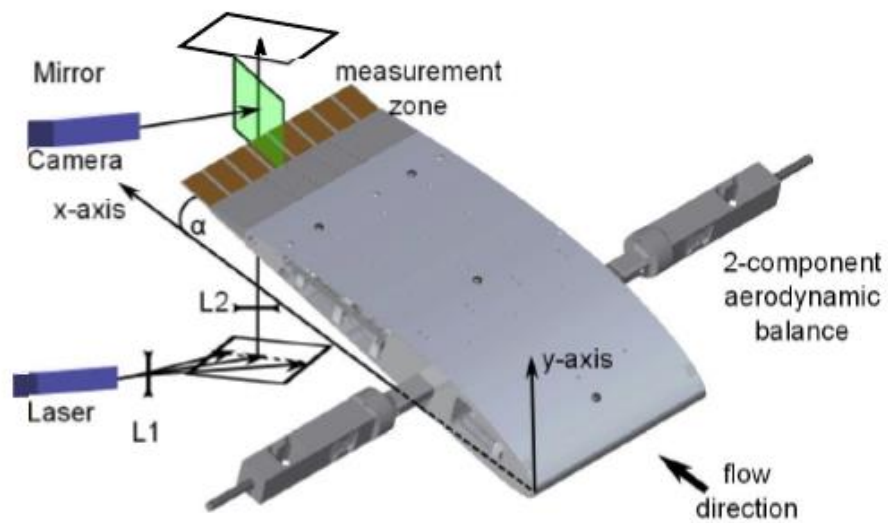
Figure 3.7: TRPIV setup

The laser pulsation are generated by two cavities Nd:YLF (527 nm) laser Quantronix Darwin Duo. A laser sheet is produced, by a laser sheet generator, in the *x-y* plane and focalised on the investigation area. An additional mirror reflects the generated laser sheet so that intersects with the midsection of the structure. The thickness of the laser sheet is about 1.5 mm.

Particle images are recorded during the duration of the experiment by the high speed camera. The recorded image are divided in "interrogation windows" of 16x16 pixel which corresponds to 2.3x2.3 mm^2, with an overlap of 50%. The most probable displacement of the particles between consecutive images for a selected interrogation window is obtained form the cross-correlation. The particle velocities are calculated from the value of the displacement and the time delay between two consecutive laser pulses.

Chapter 4. Experimental results

The experimental results are split in two parts, in a first part the effects of the high-frequency low amplitude actuation on the flow are analysed by means of time-averaged velocity and Reynolds stresses tensor component, and also with a POD analysis.

In a second part the effect of both high-frequency and low-frequency large amplitude actuation are investigated using phase-averaged velocity and Reynolds stresses components.

4.1 MFC high-frequency low amplitude actuation

This chapter will study the effects of high-frequency piezoelectric actuation embedded at the trailing edge of a prototype aileron on the flow past the trailing edge. The experimental study allows tracking of the actuation induced modifications of the shear-layer dynamics.

The actuation's effects on the flow past the trailing edge of the prototype airfoil will be investigated for three different actuation frequency 30 Hz, 60 Hz, 90 Hz and compared with the static case.

The results are organized as follow: the static case at 10° of incidence is compared with the actuated cases by means of temporal averaged velocities components and Reynold stresses.

Then a closer look is taken at the dynamics of the wake structure past the trailing edge especially the influence of the actuation frequency. All the value are made adimensional using the upstream velocity and the chord length of the prototype.

4.1.1 Normalized iso-longitudinal velocity components

Figure 4.1a and Figure 4.1b shows the temporal averaged iso-contours of the longitudinal (U) and vertical (V) velocity components normalized by the freestream velocity.

As can be seen in the Figure 4.1, the flow dynamic past the trailing edge are primarily contained into the shear-layer developed in the wake past the trailing edge.

The piezoelectric actuation leads to a reduction in the y-direction and x-direction of the wake dimension past the trailing edge, this is especially evident when comparing the zones of minimum velocity past the airfoil.

As shown in the velocity profile taken close to the trailing edge at $x/C = 1.02$ (see Figure 4.2 and Figure 4.3), the reduction of the minimum velocity area past the trailing edge is more evident for the actuation frequencies of 30 Hz and 60 Hz.
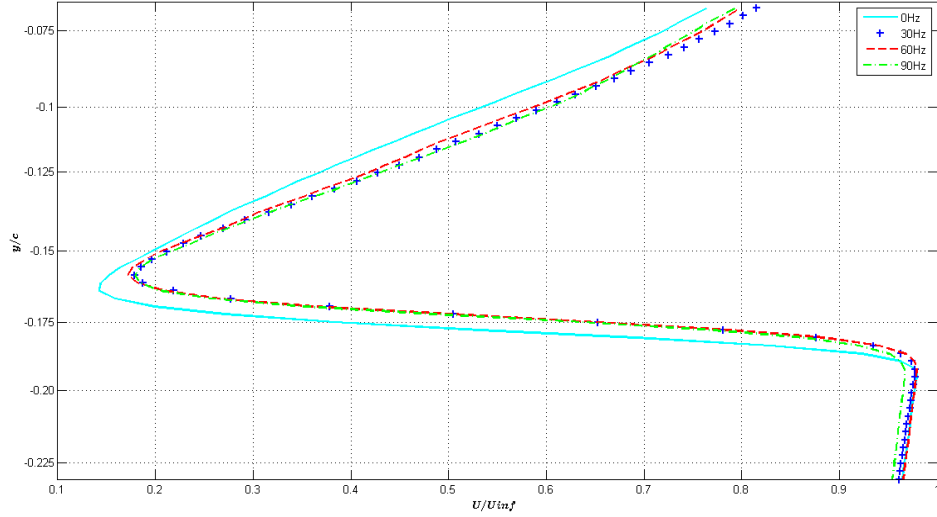
Figure 4.2: $\overline{U}/U_\infty$ velocity profile at $x/C = 1.02$
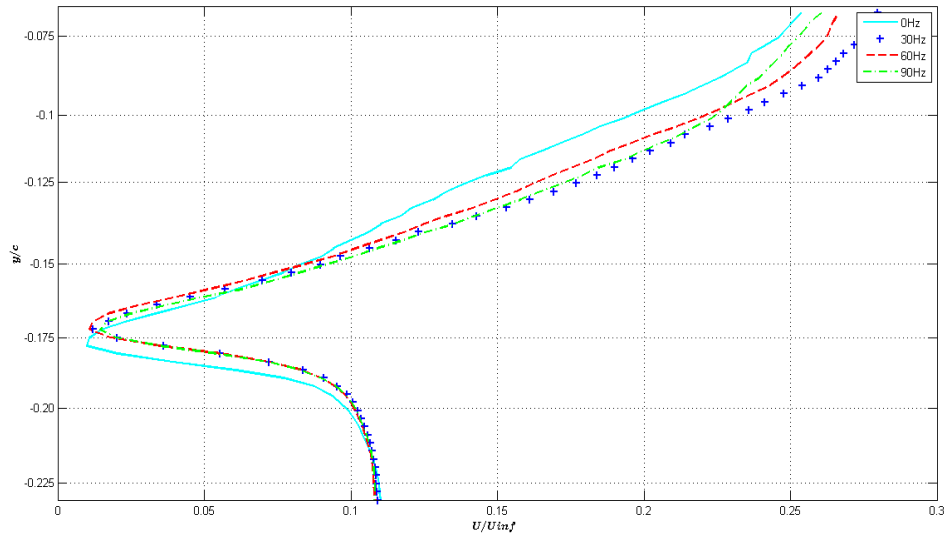
Figure 4.3: $\overline{V}/U_\infty$ velocity profile at $x/C = 1.02$

To a first approssimation, it's possible estimate the shape drag on a 2-D airfoil section by calculating the momentum loss in the wake. By looking at the change of momentum in streamwise direction, it can be shown that:

$$\int_1 U_\infty(\rho \cdot U_\infty)dy = D + \int_2 U_x(\rho \cdot U_x)dy$$

(4.1)

Where U_∞ is velocity of undisturbed flux, ρ is the air density and U_x is the velocity profile in a section past the airfoil.

Therefore, the drag force may be written as:

$$D = \int \rho\, U_\infty (U_x - U_\infty)\, dy \qquad (4.2)$$

The wake size reduction is more noticeable at the actuation frequency of 60 Hz, with a drag reduction up to 20% compared to the static case. Table 1.3 show a comparison between the actuation frequencies.

Actuation frequency	30 Hz	60 Hz	90 Hz
Drag reduction compared to the static case	17 %	20 %	10 %

Table 4.1: Drag reduction compared to the static case

4.1.2 Iso-contour of Reynolds stresses

Figure 4.1c show the time-averaged Reynold stress field of the u^2 component. The maximum $\bar{u}^2/U_\infty^2$ stress occurs in the shear-layer past the trailing edge.

As the actuation frequency increases, the size of the shear-layer is reduced (like is shown for the U and V component) which leads to a reduction of the maximum Reynolds stress past the trailing edge of the airfoil. As can be seen in the Figure 4.4 and Figure 4.5 this reduction of the shear layer is maximized for the actuated frequencies of 60 Hz.

Similar to the u^2 Reynolds stress compoment, also the $\bar{v}^2/U_\infty^2$ (see Figure 4.1d) experiances a reduction of the maximum past the trailing edge.

The shear-stress component shown in Figure 4.1d, shows a two-lobe structure that characterizes the turbulent wakes, with the increasing of the actuation frequencies the two wake decrease in size up to the frequency of 60 Hz (see Figure 4.6).

The reduction of both Reynolds stresses components lead to a reduction of the turbulent kinetic energy of the flow (TKE) defined as:

$$TKE = \frac{1}{2}\,[\overline{u'^2} + \overline{v'^2}] \qquad (4.3)$$

Where u' and v' are the velocity fluctuations in according to Reynolds depomposition. Calculating the mean turbulent kinetic energy in the wake for the different cases, the actuation frequency of 60 Hz lead a reduction of the mean TKE up to 16 % compared to unactuated case. Table 4.2 show a comparison between the actuation frequencies.
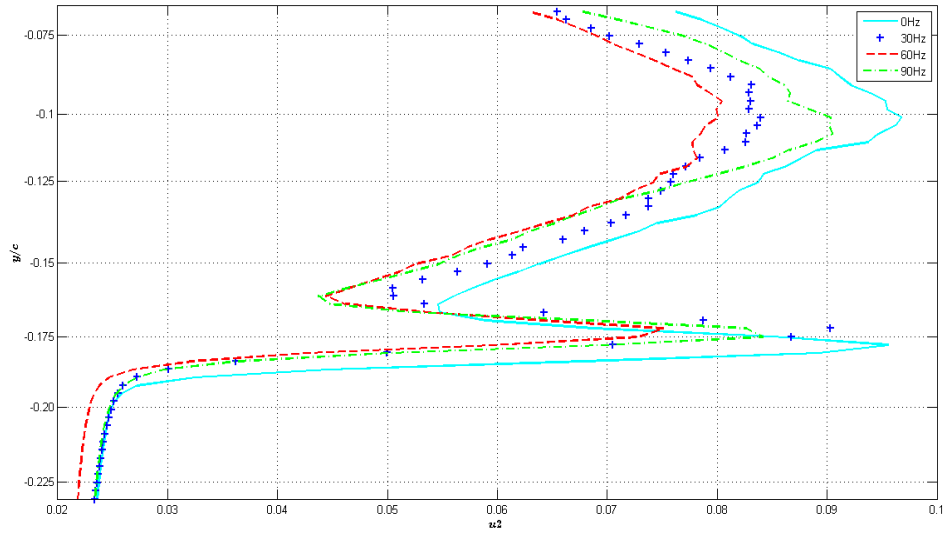
Figure 4.4: $\bar{u}^2/U_\infty^2$ profile at $x/C = 1.02$
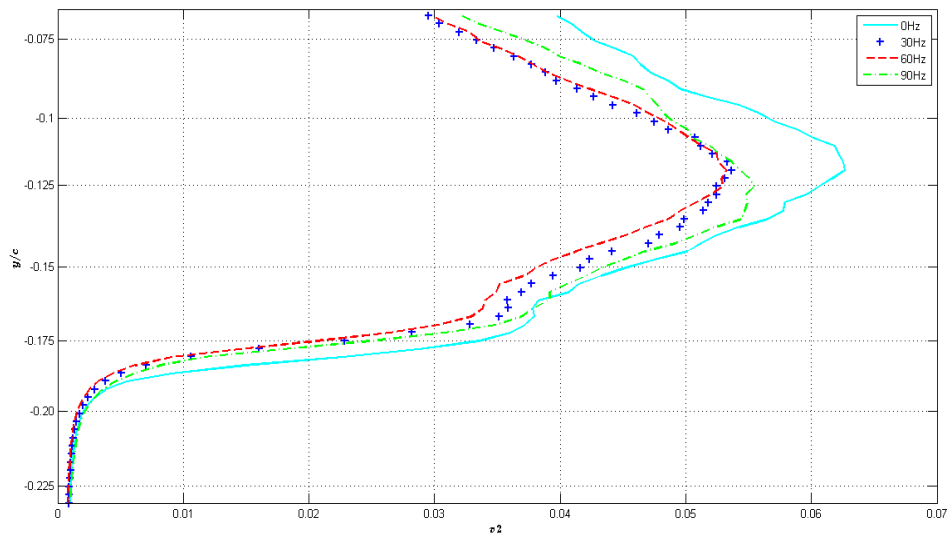
Figure 4.5: $\bar{v}^2/U_\infty^2$ profile at $x/C = 1.02$
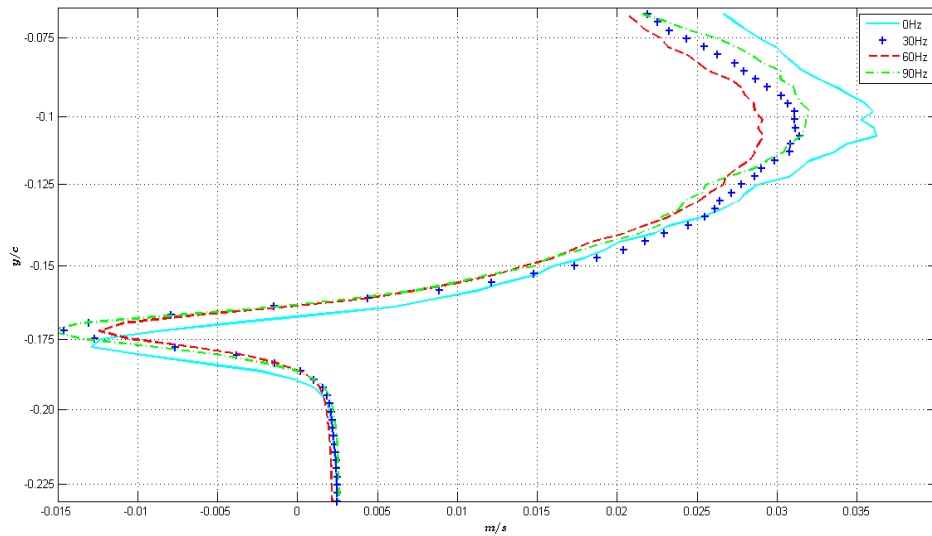
Figure 4.6: $\overline{uv}/U_\infty^2$ profile at $x/C = 1.02$

Actuation frequency	30 Hz	60 Hz	90 Hz
TKE reduction compared to the static case	12 %	16 %	10 %

Table 4.2: TKE reduction compared to the static case

4.1.3 Shear-layer dynamics past the tailing edge

Figure 4.7 shows the spectral density of the vertical velocity component V at points *x/c = 1.015; y/c = 0.125, x/c= 1.06; y/c = 0.15, x/c = 1.11; y/c = 0.175*. The spectra are calculated subtracting the average velocity and a comparison between the unactuated case and the actuated case is done.

The averaged spectra is realized doing a mean of the spectra of five near point, spatially speaking, in order to better show up the peacks of frequency. Nevertheless at 10° of incidence no characteristic Von Karman vortices can be observed(see Figure 6).

Comparison of the vortex motion of the unactuated case and the actuated cases at 30 Hz, 60 Hz and 90 Hz is shown in Figure 6. The first wavelet of the vortices past the trailing edge of the unactuated airfoil is of the order of 0.04 m as shown in the left column of Figure 4.9.

Comparing the vortex motion of the static case and the actuated cases we can see that the turbulent energy is reduced with the increasing of actuation frequency f_{act}. This leads to a reduction of the size and the number of the vortices caused by vortex splitting which increases the turbulent energy dissipation. This reduction is more noticeable for the frequencies of 60 Hz and 90 Hz, for the higher frequency the size and choerence of vortices is considerably reduced. This coincides well with the previously discussed Reynolds stress field.

This reduction of the turbolent energy can be explained looking at the energy spectra for different positions and actuation frequency (see Figure 4.7). With the increasing of the actuation frequency itself became predominant in the spectra, especially for the case at 90 Hz where the actuation frequency supersedes all the other frequencies (see Figure 4.7d). This effect can be explained considering the amount of kinetic energy seeded into the flow by the trailing edge actuation, that increase with the increasing of the actuation frequency. The energy seeded into the flow focuses the all energy of the flow onto the frequency of actuation.

In general the trailing edge actuation induces an attenuation of the frequences higher than the actuation frequency, and a reduction of the average value can be seen at the actuation frequency of 60 Hz, this also agree with the results obtained in the velocity analysis.
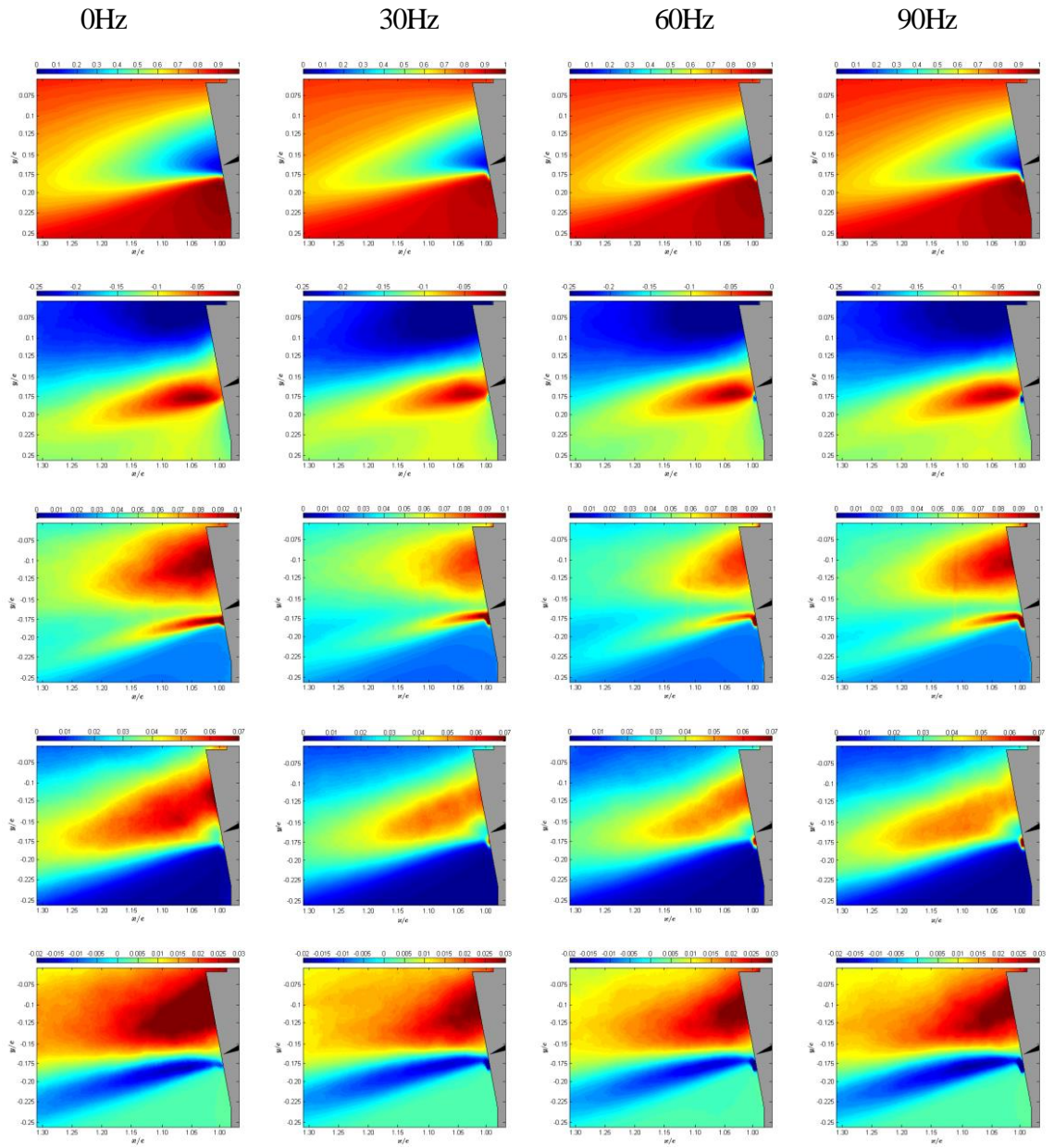
Figure 4.1: Time average velocity and Reynold stress components: from top to bottom of $\overline{U}/U_\infty$ (a), $\overline{V}/U_\infty$ (b), $\overline{u^2}/U_\infty^2$ (c), $\overline{v^2}/U_\infty^2$ (d), $\overline{uv}/U_\infty^2$ (e)

(a) 0 Hz   (b) 30 Hz   (c) 60 Hz   (d) 90 Hz
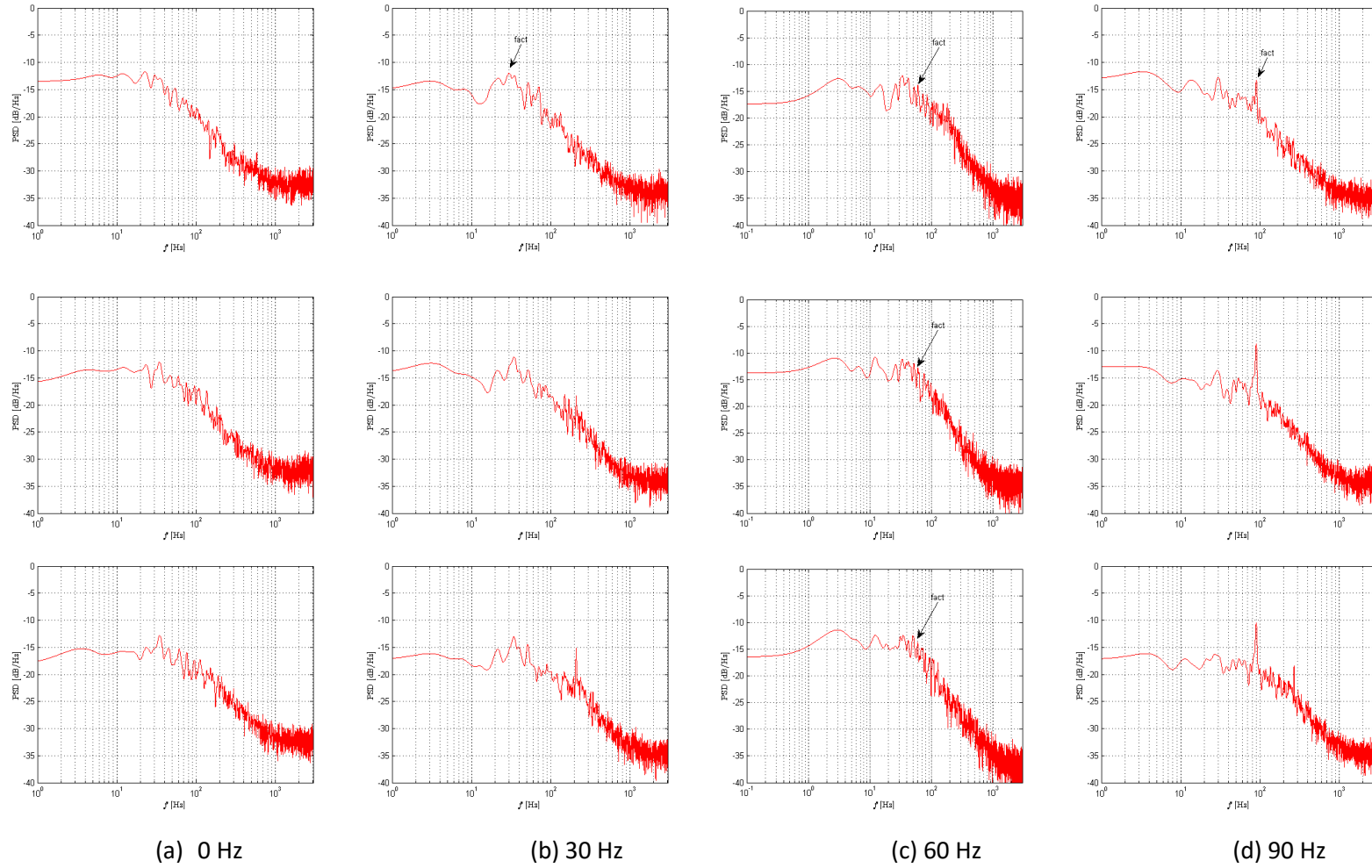
Figure 4.7: V velocity spectra, static case x/c = 1.015; y/c = 0.125, x/c= 1.06; y/c = 0.15, x/c = 1.11; y/c = 0.175 (from top to bottom)
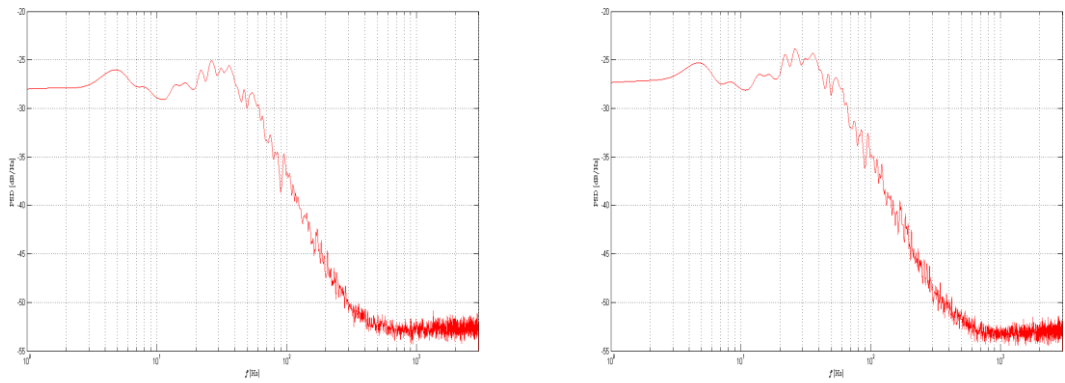
Figure 4.8a: V velocity averaged spectra, static case: x/c = 1.01; y/c = 0.15 (left), x/c = 1.05;y/c = 1.18 (right)
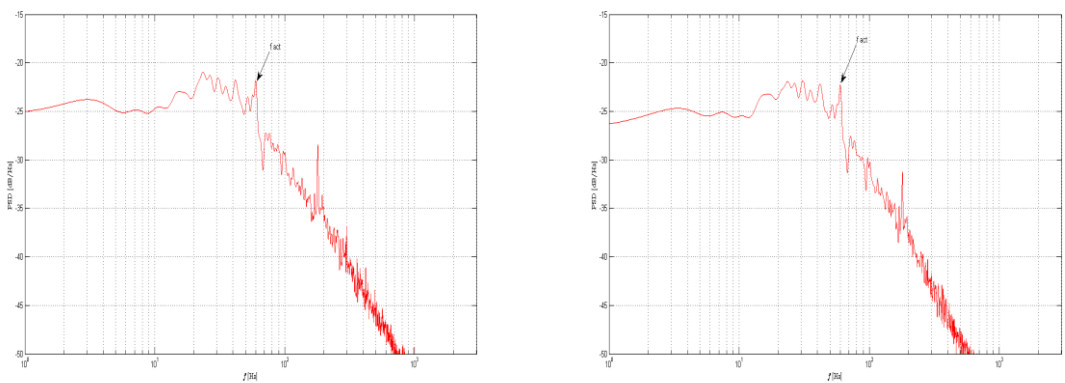
Figure 4.8b: V velocity averaged spectra, actuated case 60Hz: x/c = 1.01 ; y/c = 0.15 (left), x/c = 1.05 ,;y/c = 0.175(right)
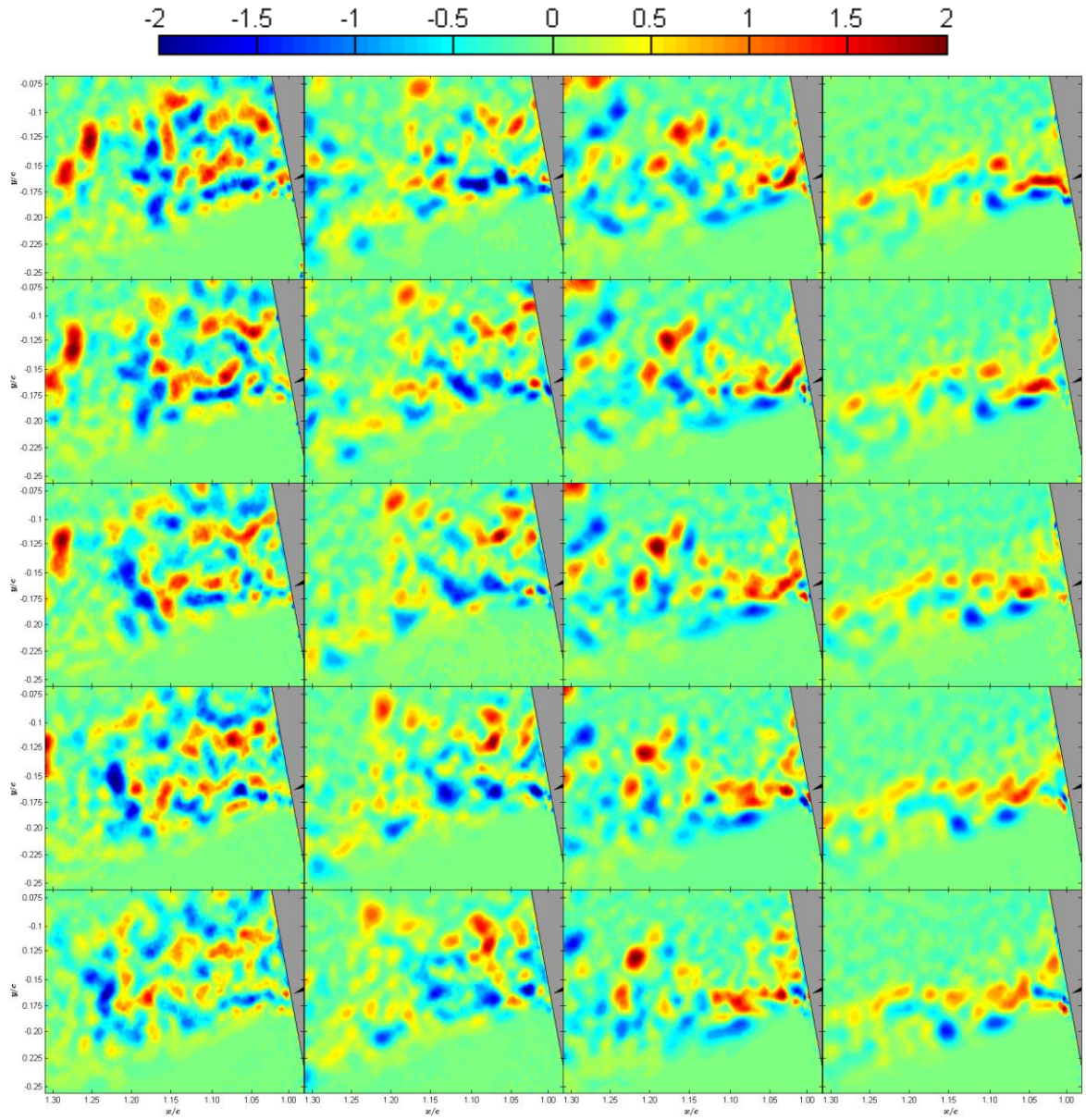
Figure 4.9: Sequence of vortex motion Δt=0.005 for the unactuated case and the frequencies 30 Hz, 60 Hz, 90 Hz (from left to right)

4.1.4 POD analysis

In this part, the behaviour of the flow at different actuation frequencies is analysed using POD decomposition, in order to in depth analyse the propagation of coherent structures within the flow.

The energy of the POD modes is a function of the mode order, there is an energy decade towards the higher mode, in according to the POD decomposition method. Considering the first 16 POD modes we can be able to reach up to the 50 % of the total energy.

As shows in the Figure 4.10 the energy content of first mode appears sensibly higher than the characterising the 2nd mode, the first two modes appears consequently uncoupled , while mode pairing seems to be re-established for the 2nd and the 3rd modes and so on.

The spatial distribution of the first four most energetic POD modes is represented in Figure 4.11 and Figure 4.12. Comparison with the spatial distribution of the POD modes, make clear that the first two modes are uncoupled, as suggested by the energy distribution.

The first mode identifies an extended region of positive values with almost uniform distribution, the modes uncoupling can be attributed to unsteady phenomena characterized by wavelength longer than the extension of PIV measurement area [Liu et al. (2001)]. Vortical structures can be observed in the following modes, as show in particular in the spatial V velocity modes.

The second and third modes, for the unactuated case and the 60 Hz actuated case, are also represented in vector form (Figure 4.11a). The spatial modes shows a counter-clockwise rotating vortex followed by a clockwise vortex. The distance between two counter vortices is equal to half of the wavelength, as represented.

The mode distribution appear similar, but they are characterized by a spatial shift, that correspond to a shift of $1/4$ of the wavelength, which is typical of vortex shedding phenomena [Wee et al.,2004].

This considerations are valid both for the unactuated and the actuated at 60 Hz case. It can be also observed that for the actuated case the wavelength seems to be smaller, this reduction can be also observed in vortex motion (Figure 4.9), caused by vortex splitting that reduce the choerence of vortices.

The temporal POD coefficients (see Figure 4.17) are in accordance with the spatial mode behaviour (see Figure 4.11, Figure 4.13 and Figure 4.15). As the order of the modes increase, a filling-up of the temporal coefficient signal by higher frequencies is noticed, due to increasing of turbulence.

The actuation of the trailing edge introduces additional mode, as can be seen in the higher POD modes (Figure 4.12, Figure 4.14 and Figure 4.16), whereas the first POD modes look similar each other at different frequencies.

Looking at the energy density spectra of the temporal modes (see Figure 4.18), we can see that the overall energy density level is reduced for the actuation frequencies 30 Hz and 60 Hz whereas for 90 Hz actuation the energy level is increased again with a clear peak for the actuation frequency.

This behaviour, as explained in the previous section, it's due to the energy seeded into the flow by the piezoelectric actuation that increases with the increases of the actuation frequency, at 90 Hz the actuation frequency itself became predominant and supersedes all the other frequencies. The actuation frequency of 60 Hz lead to a reduction of the overall energy density of about 22 % compared to the unactuated case.

4.1.5 Conclusion

The goal of this study was to show the effect of a low amplitude, high frequency piezoelectric actuation embedded in the trailing edge of an airfoil prototype on the flow.

By the actuation of the trailing edge it's possible attenuate the high frequency vortices, which are the major source of noise, and was identified an optimum actuation frequency of 60 Hz by comparing the Reynold stresses fields and the energy density spectra for the different actuation frequencies.

The actuation frequency of 60 Hz lead to a reduction of the overall energy density in the flow up to 22 %, as well as a reduction of the turbulent kinetic energy up to 16 %, and a reduction of wake size width that leads to a reduction of shape drag up to 20%.

0 Hz
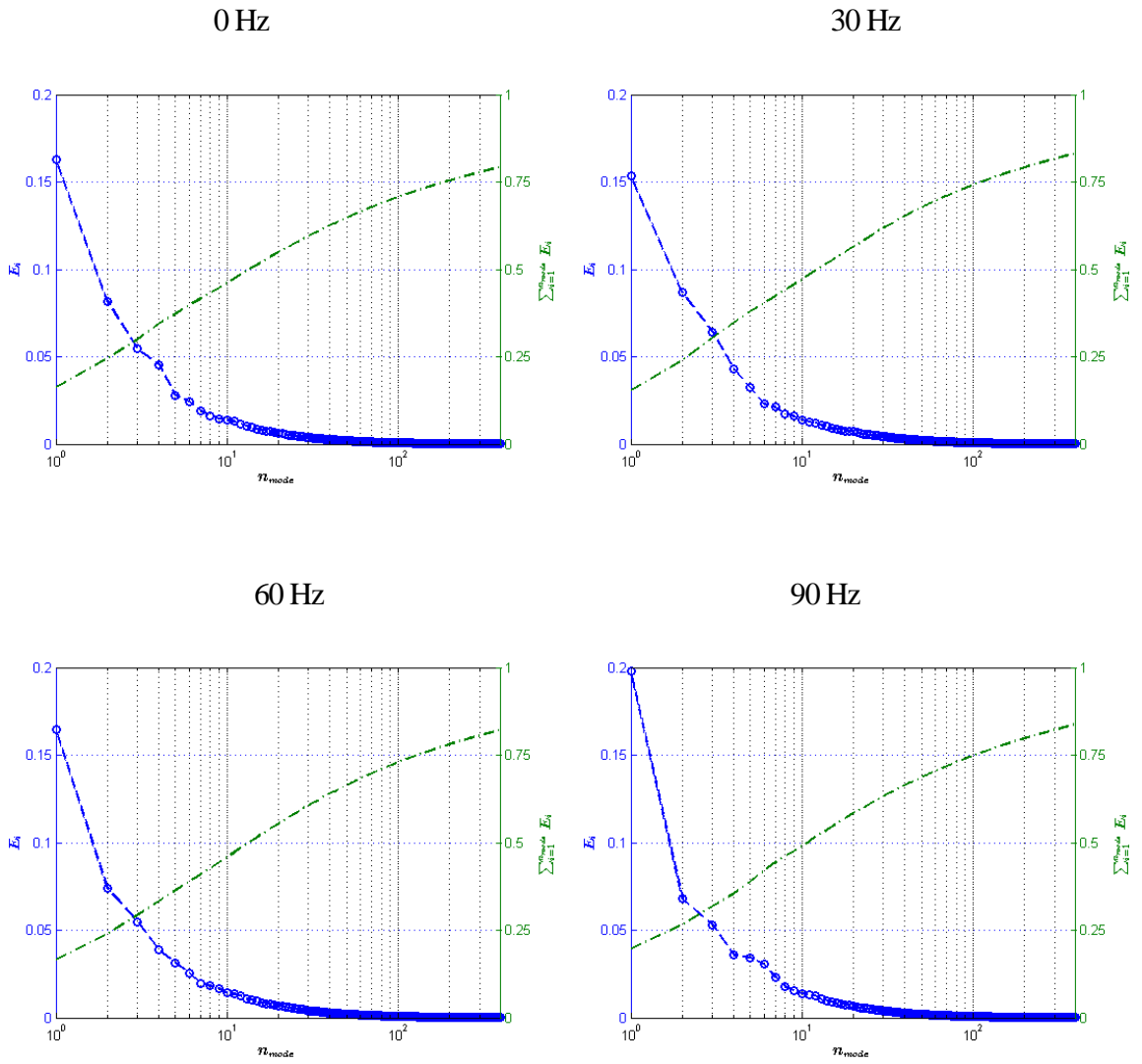
30 Hz

60 Hz

90 Hz

Figure 4.10: Energy of POD modes. Form left to rigth: 0Hz, 30Hz, 60Hz, 90Hz
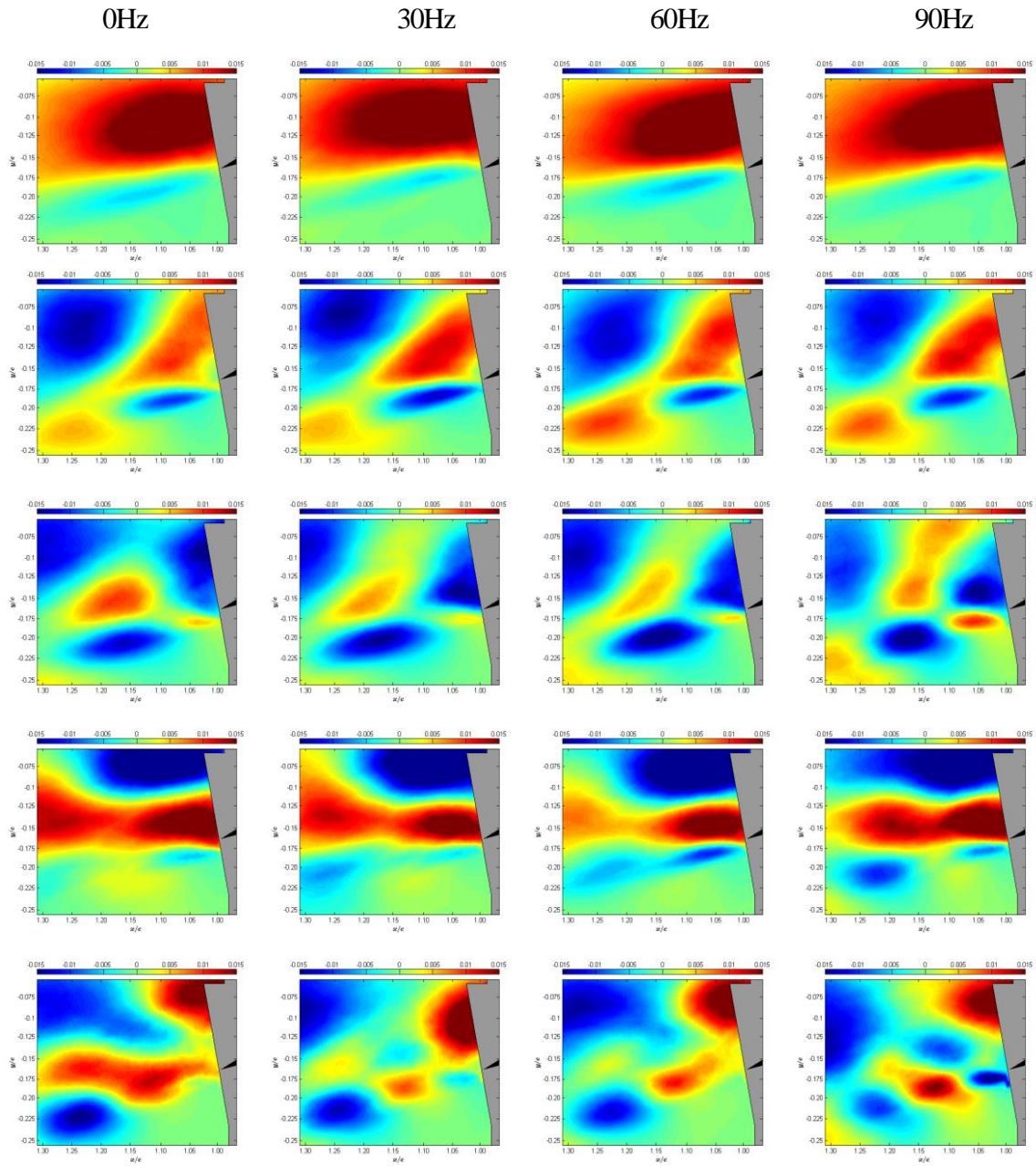
Figure 4.11: Comparing of the first five POD spatial U velocity modes (from top to bottom)
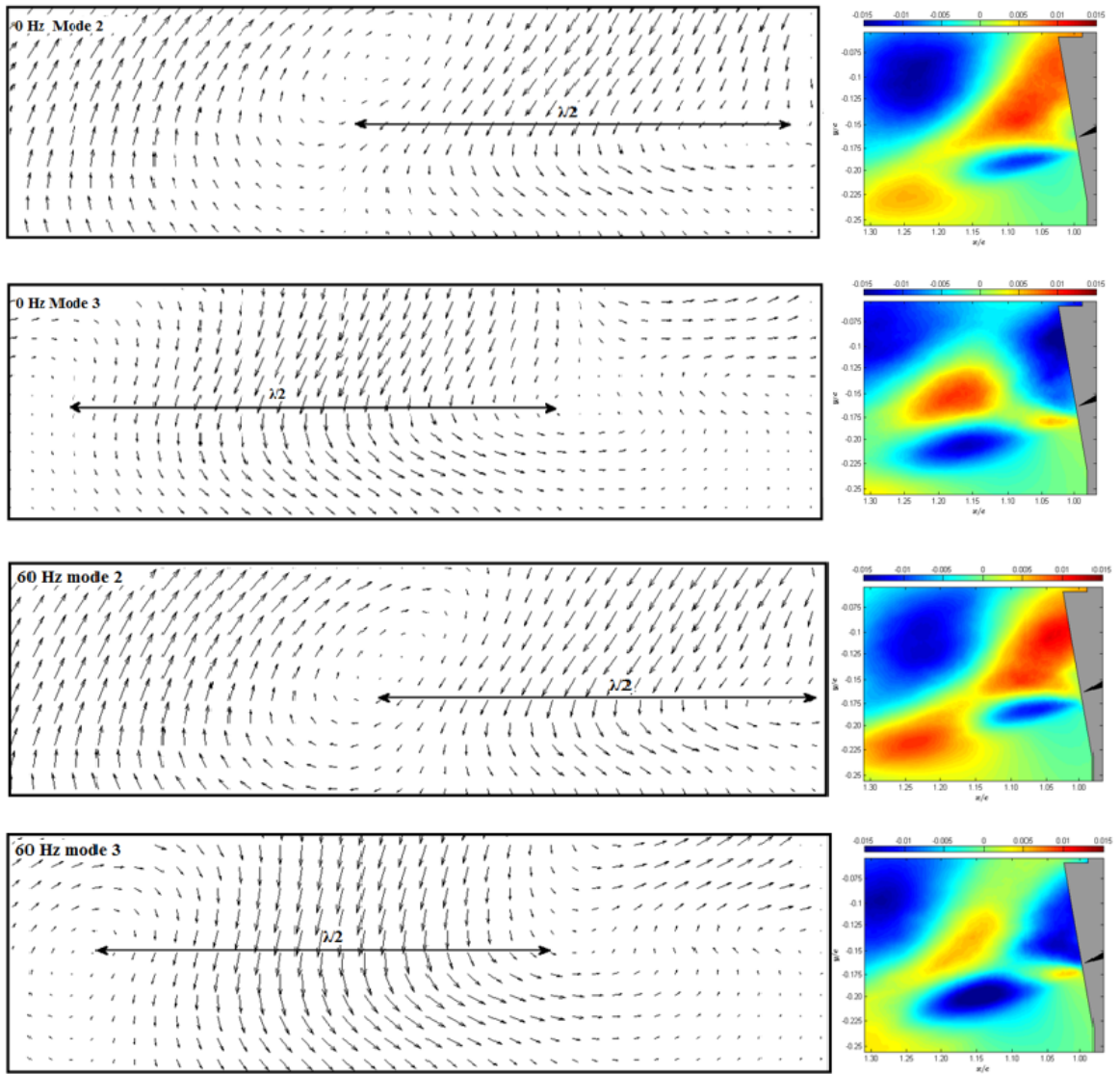
Figure 4.11a: Comparing of the second and third POD modes vector field (0 Hz top, 60 Hz bottom)
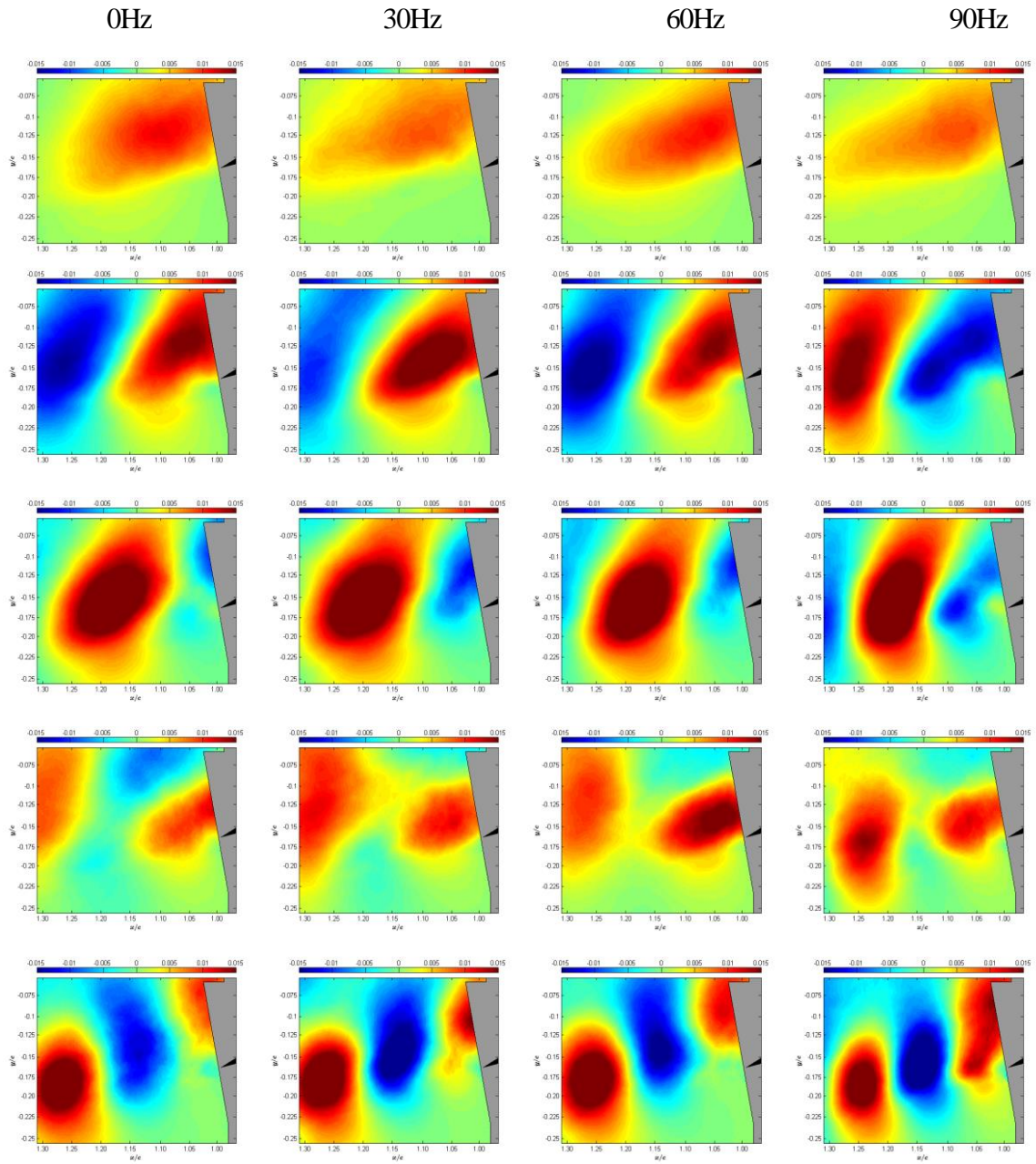
Figure 4.13: Comparing of the first five POD spatial V velocity modes (from top to bottom)
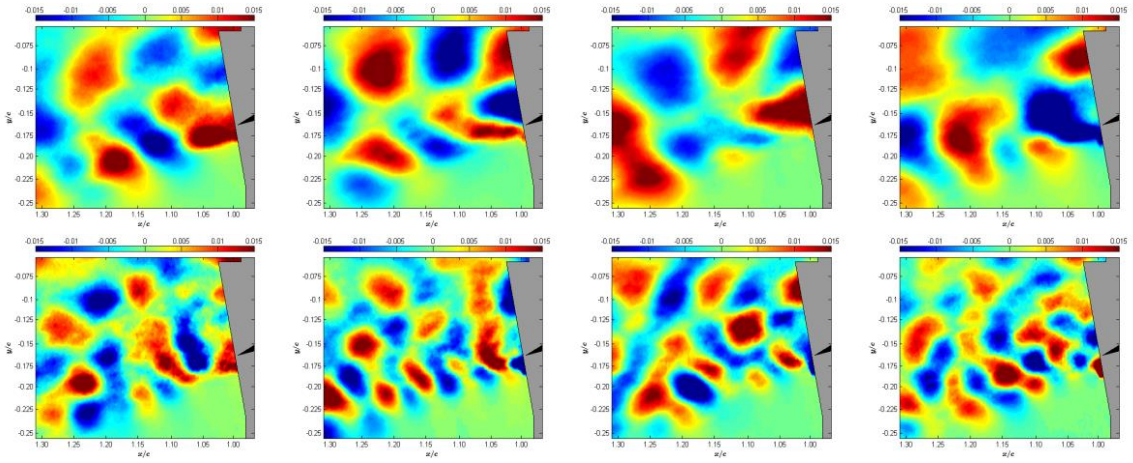
Figure 4.12: Higher POD spatial U velocity modes: mode 15; 50
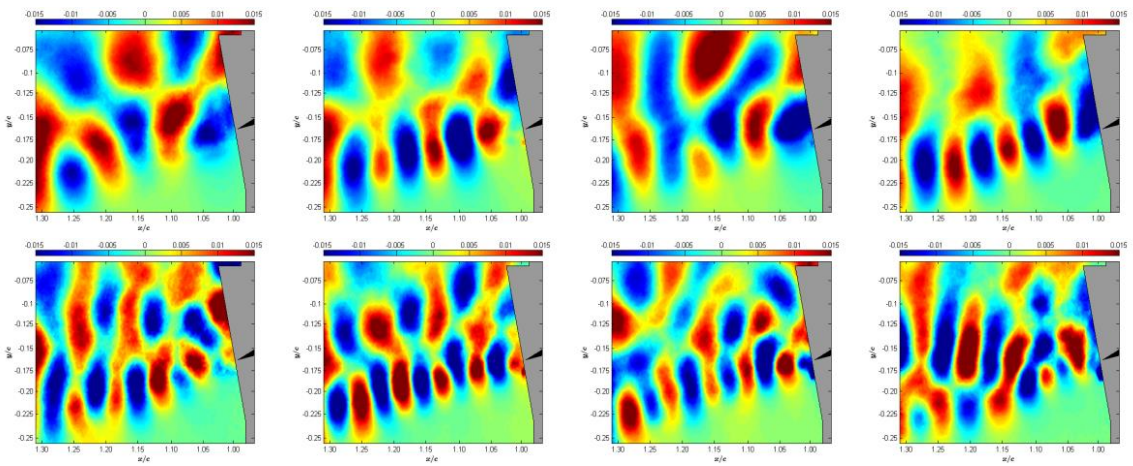
Figure 4.14: Higher POD spatial V velocity modes: mode 15; 50

0Hz 30Hz 60Hz 90Hz
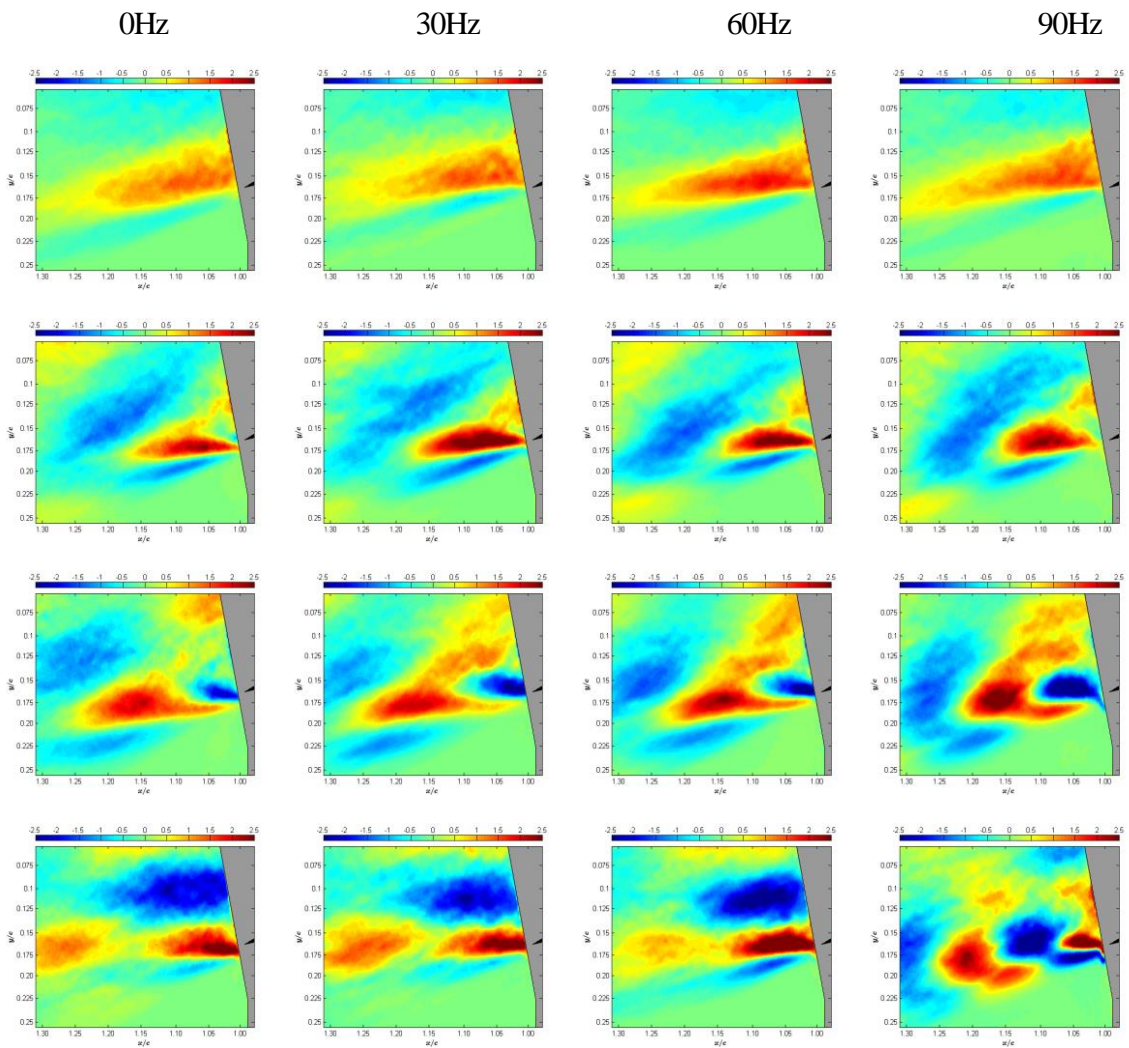
Figure 4.15: POD vorticity mode: comparing the first four POD modes (from top to bottom)
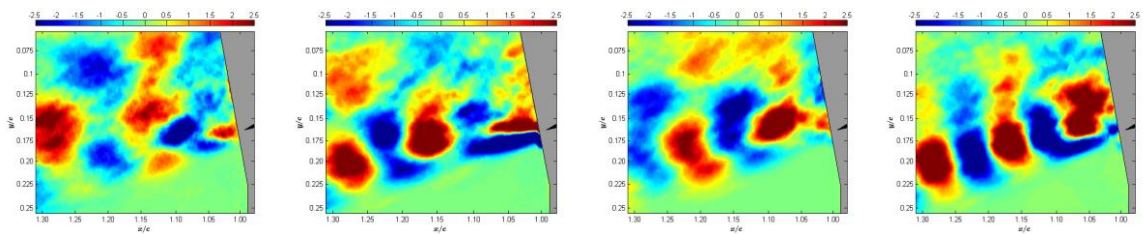
Figure 4.16: Higher POD vorticity modes: mode 15

0Hz 30Hz 60Hz 90Hz
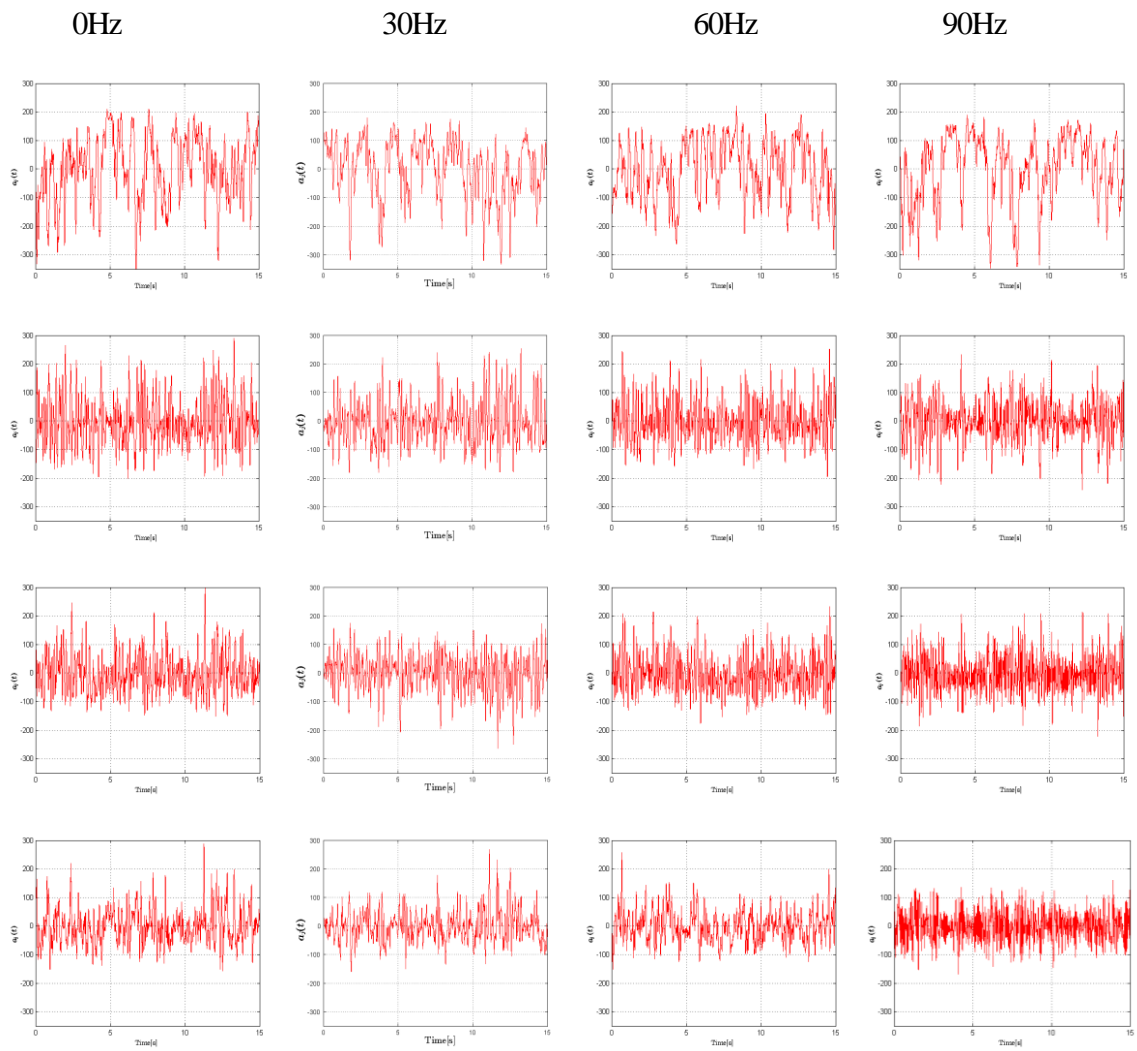
Figure 4.17: Comparing of the first four POD temporal modes (from top to bottom)

Figure 4.18: Spectra of temporal modes comparison: comparing of the first four POD modes (from top to bottom).
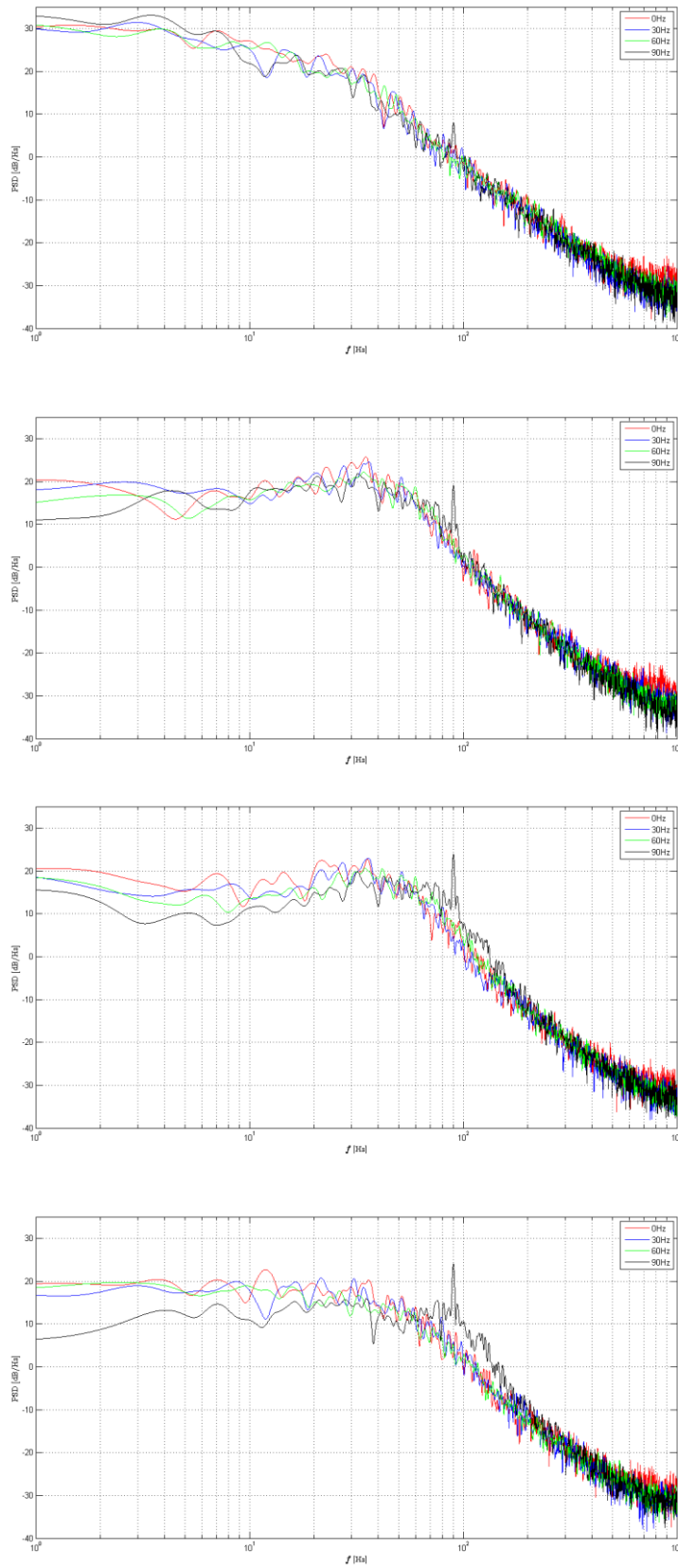
4.2 SMA large-amplitude at 60 Hz actuation

In this chapter an analysis of the near region past the trailing edge of the actuated airfoil, both high-amplitude low-frequency (SMA) and high-frequency low-amplitude (MFC), will be performed.
The large-amplitude actuation modify the recirculation area past the trailing edge, and the lift and drag characteristics of the airfoil in function of the aircraft's mission profile.
Whereas the high-frequency actuation has the capacity to act directly on the shear-layer resulting in a reduction of the Reynold's stress components (as shown in the previous chapter).

4.2.1 Trailing edge position

The trailing edge displacement is shown in Figure 4.19, illustrating the variation of the trailing edge position throughout the measurement interval. The figure also shows how the total measure sequences are divided in order to perform a phase-average of the velocity components.
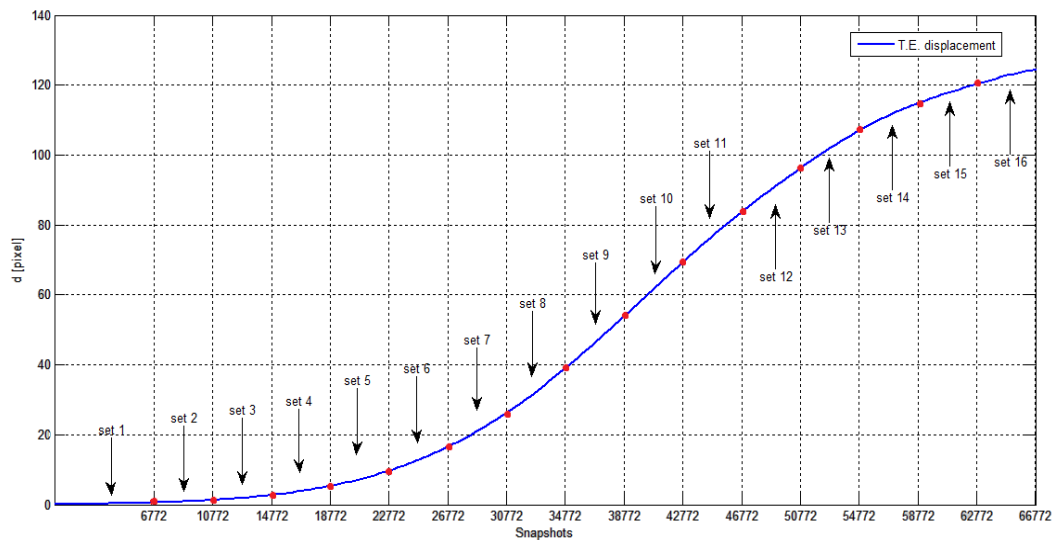
Figure 4.19: Trailing edge position evolution during the measurement interval

Each measurement sequence is divided in 16 set each of 4000 snapshots in order to guarantee a low displacement of the trailing edge. A total of 28.000 consecutive field were averaged for each position extracted from seven distinct measurement sequences.
Four different position of the trailing edge were selected (Figure 4.20) corresponding to the starting and the final positions set '1' and set '16' (respectively position '1' and position '4') and two intermediate positions corresponding to set '8' and set '11' (respectively position '2' and position '3').

55
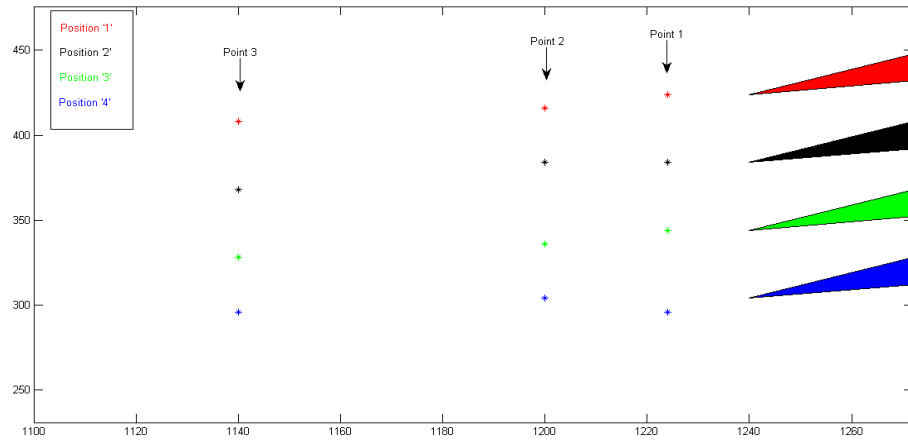
Figure 4.20: Selected different position of the trailing edge

For each position were selected three different point past the trailing edge where the convergence of *u,* *v* fluctuations and the Reynolds stress component was verified (Figure 4.24 and Figure 4.25).

4.2.2 Phase-averaged velocity components dynamic case

Figure 4.26 and Figure 4.27 shows the phase-averaged iso-contours of the longitudinal (U) and vertical (V) velocity components normalized by the freestream velocity. The modification of the trailing edge position is shown schematically on the right side of the figures.

As can be seen in the figure, the flow dynamic past the trailing edge are primarily contained into the shear-layer developed in the wake past the trailing edge.

Looking at the phase-averaged longitudinal field (see Figure 4.26) and in particular at the U velocity profile taken close to the trailing edge (see figure 4.21) can be seen a reduction of the wake size from the position '1' to the intermediate position '2' and '3'. Then the wake size grow again in the final position of the trailing edge (position '4'). This behaviour can be explained considering the dynamic actuation of the trailing edge, in particular by the additional kinetic energy provided by the dynamic actuation. The trailing edge displacement is higher in the intermediate positions, so the kinetic energy provided to the flow is higher than in the initial and final position, where the displacement is less than the intermediate cases (see Figure 4.19). This leads to a reduction of minimum velocity of the wake past the trailing edge during the actuation of the trailing edge.

Comparing the phase-averaged vertical field (see Figure 4.27) a decrease of the vertical velocity component especially above the airfoil can be observed, due to the increase of bending of the profile (see Figure 4.22).
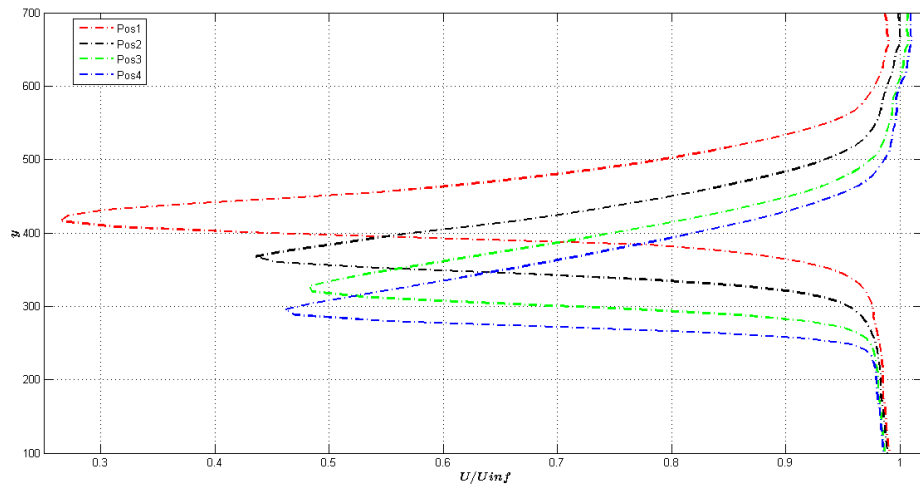
Figure 4.21: U velocity profile close to the trailing edge at $x/C = 1.02$
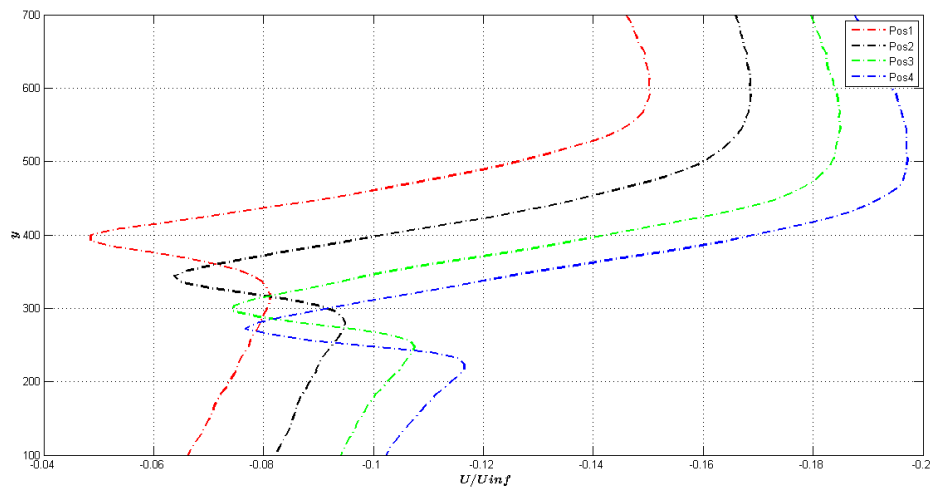
Figure 4.22: V velocity profile close to the trailing edge $x/C = 1.02$

4.2.3 Phase-averaged Reynolds stress tensor

The phase-averaged normalized Reynold stress field component u^2 is shown in Figure 4.28.
The maximum u^2 stress occurs in the shear layer. During the deformation of the airfoil an increase of maximum u^2 stress is visible and a spread from a single lobe (initial position) to a more evident two lobe configuration. The maximum u^2 stress occurs for the middle positions of the trailing edge.
The Reynolds stress v^2 component is shown in Figure 4.30, like for the u^2 the maximum can be found in the shear-layer. An increase of the v^2 component occurs through the deformation of the airfoil, due to the increase of bending of the profile and the increase of the module of the vertical velocity component (see Figure 4.23).
The shear-stress component uv shown in Figure 4.29, shows a two-lobe structure that characterizes the turbulent wakes, without changes by the increase of the profile bending.
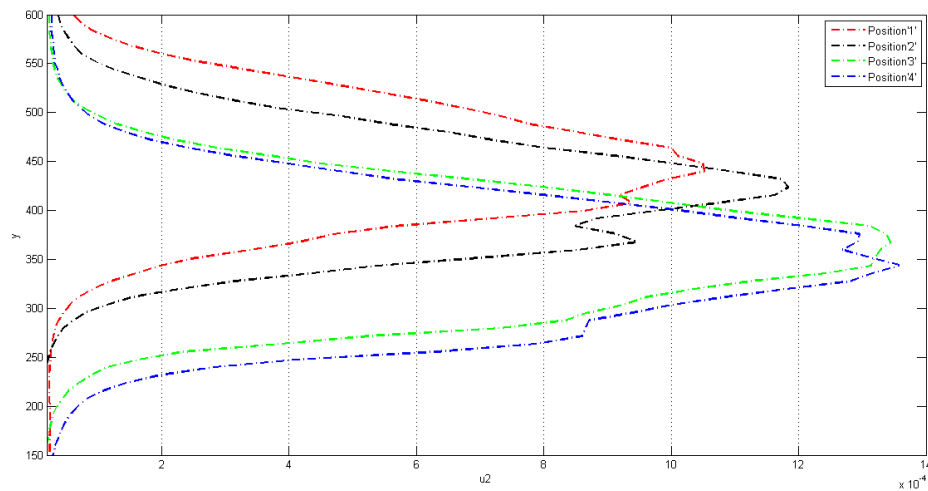
Figure 4.23: v^2 profile close to the trailing edge $x/C = 1.02$

4.2.4 Shear-layer dynamics past the trailing edge

Figure 4.31 shows the spectral density of the vertical velocity component V for the 'Position 1' of the trailing edge. As can been seen in Figure 4.31a, that represent the power spectra of the vertical velocity in the point close to the trailing edge, all the energy of the flow focuses onto the frequency actuation of 60 Hz. Otherwise, further the trailing edge (see Figure 4.31c), there is a clear peak in the energy density spectra at around 15.5 Hz.
Figure 4.32 shows the vorticity field at the same instant for the four different position. The fist wavelet past the trailing edge is of the order of 0.05 m. By combining the space-time tracking of these vortices and the energy density spectra of the vertical velocity, the shedding frequency of the shear layer has been assessed to be of the order of 150 Hz.
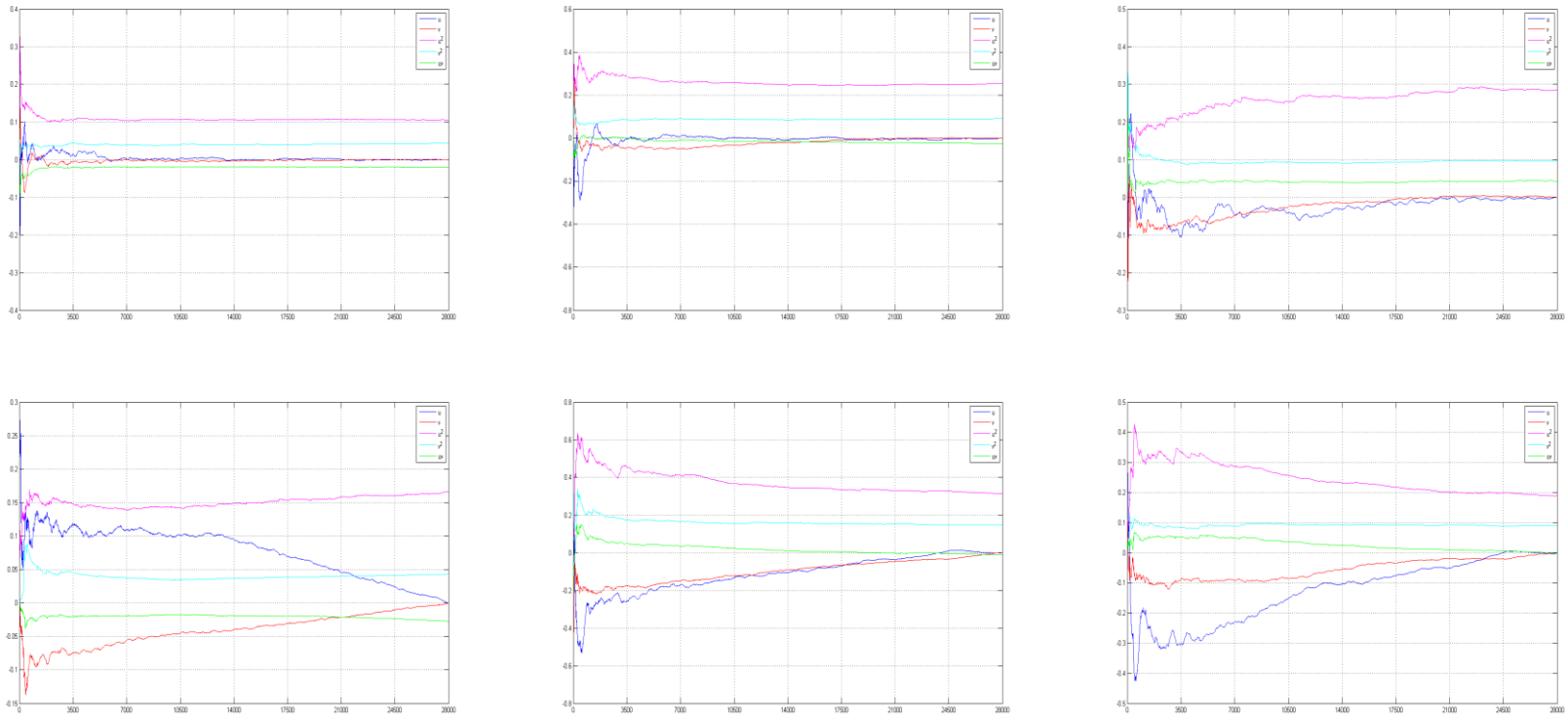
Figure 4.24: Convergence evaluation Position '1' and '2' (from top to bottom) for the point '1', '2' and '3' (from left to right)
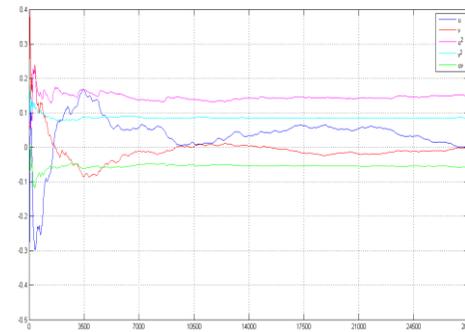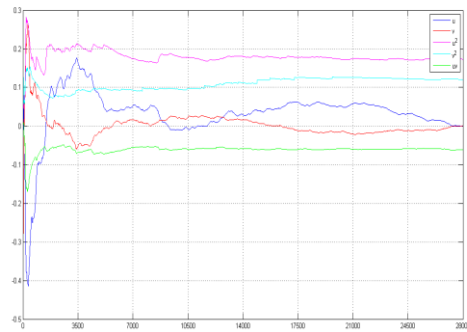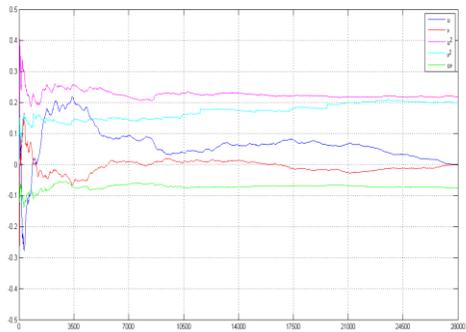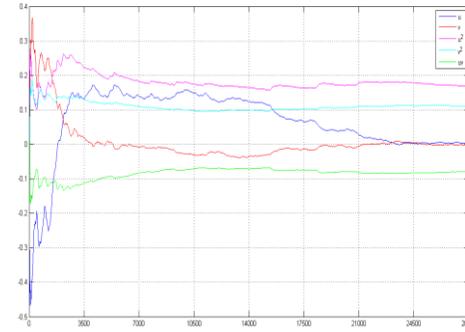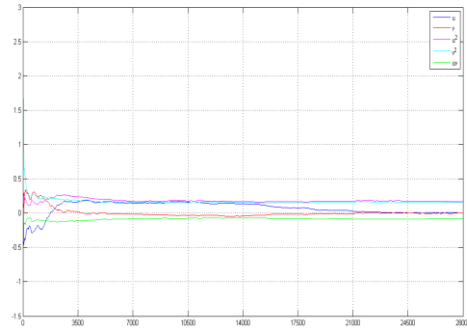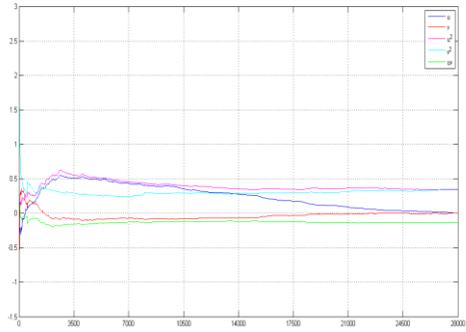
Figure 4.25: Convergence evaluation Position '3' and '4' (from top to bottom) for the point '1', '2' and '3' (from left to right)
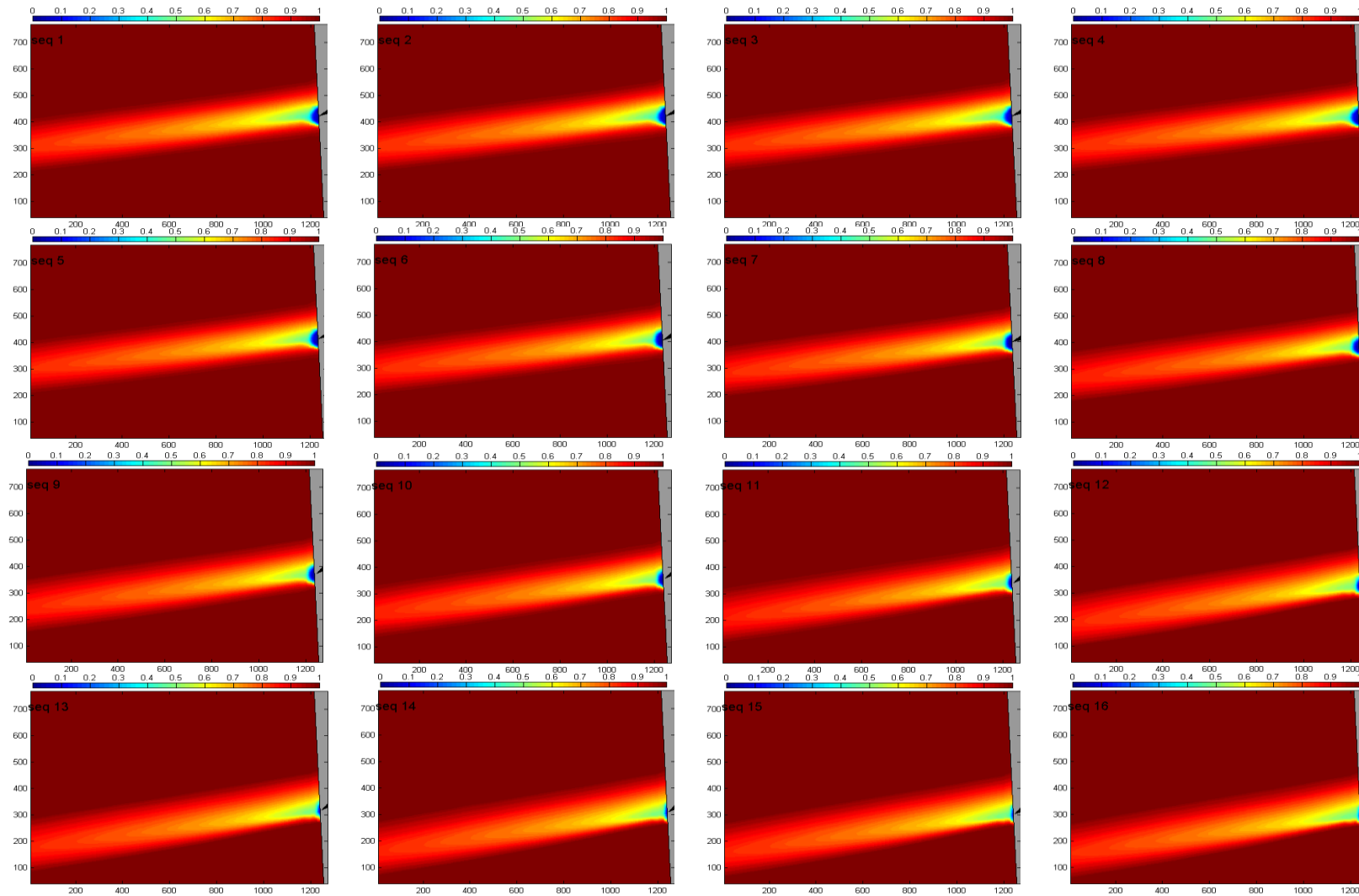
Figure 4.26: Comparison of $\langle \overline{U} \rangle / U_\infty$ SMA actuation
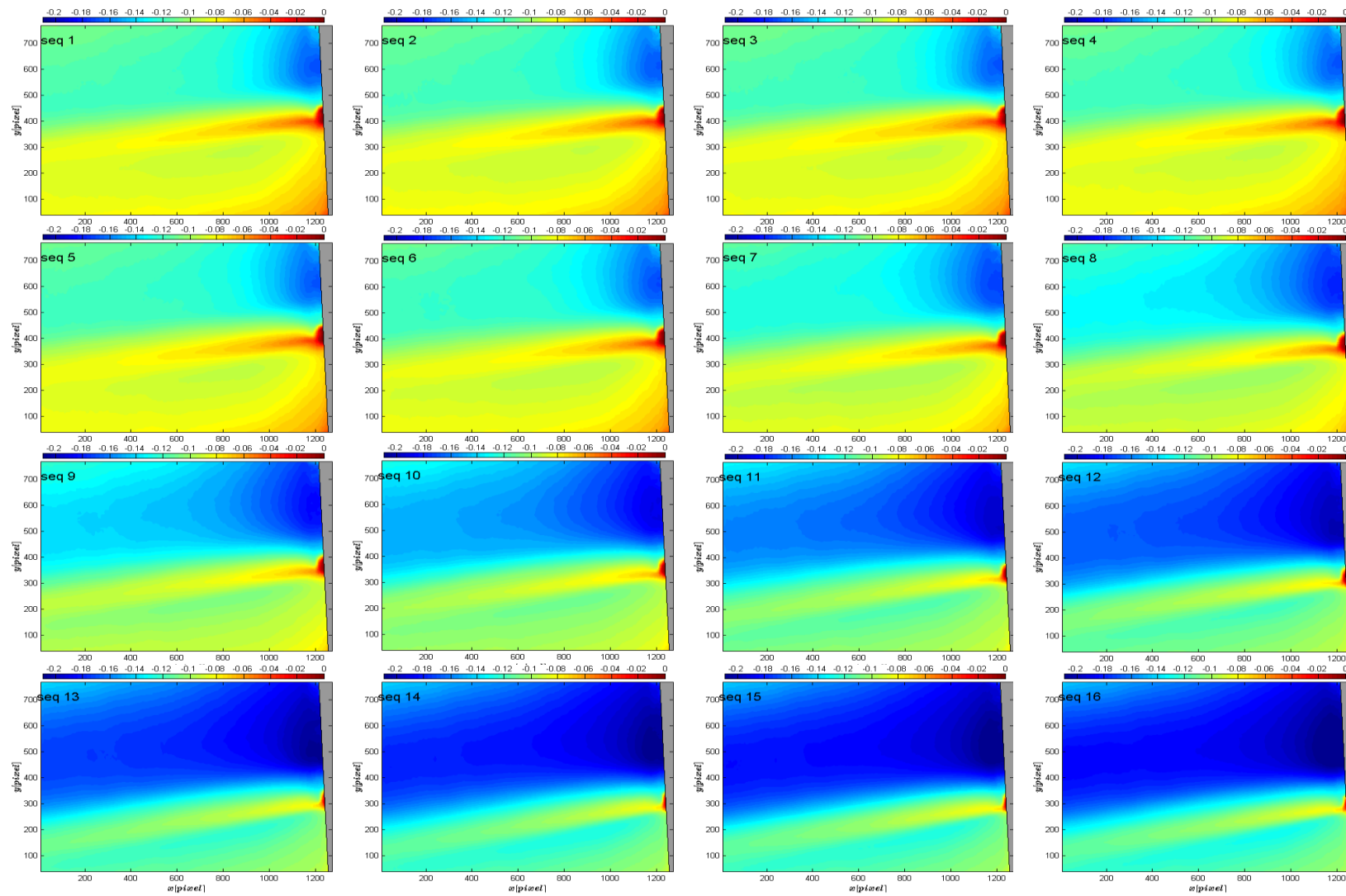
Figure 4.27 Comparison of $\langle \overline{V} \rangle / U_\infty$ SMA actuation
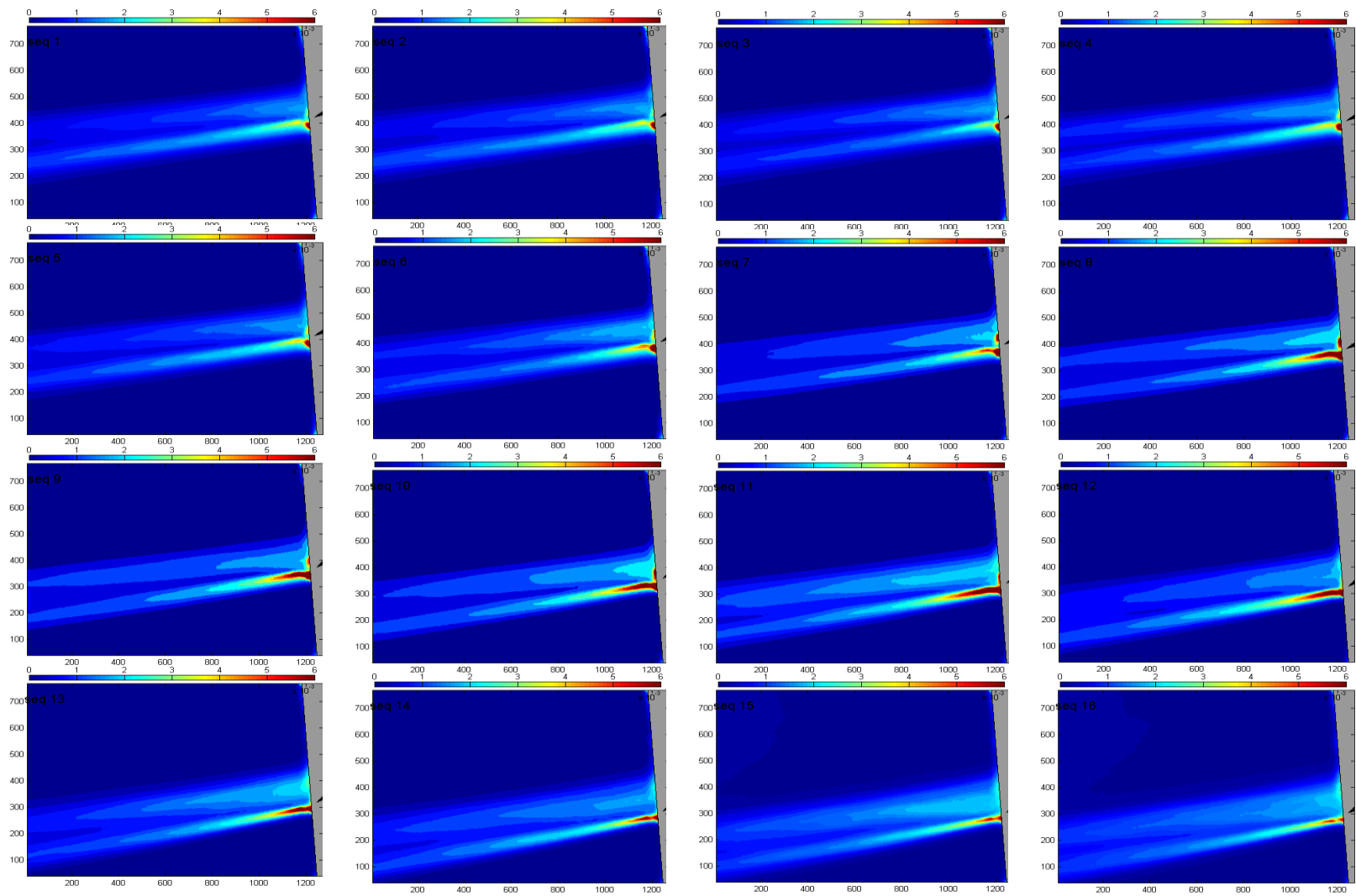
Figure 4.28: Comparison of $\langle \overline{u^2} \rangle / U_\infty^2$ SMA actuation
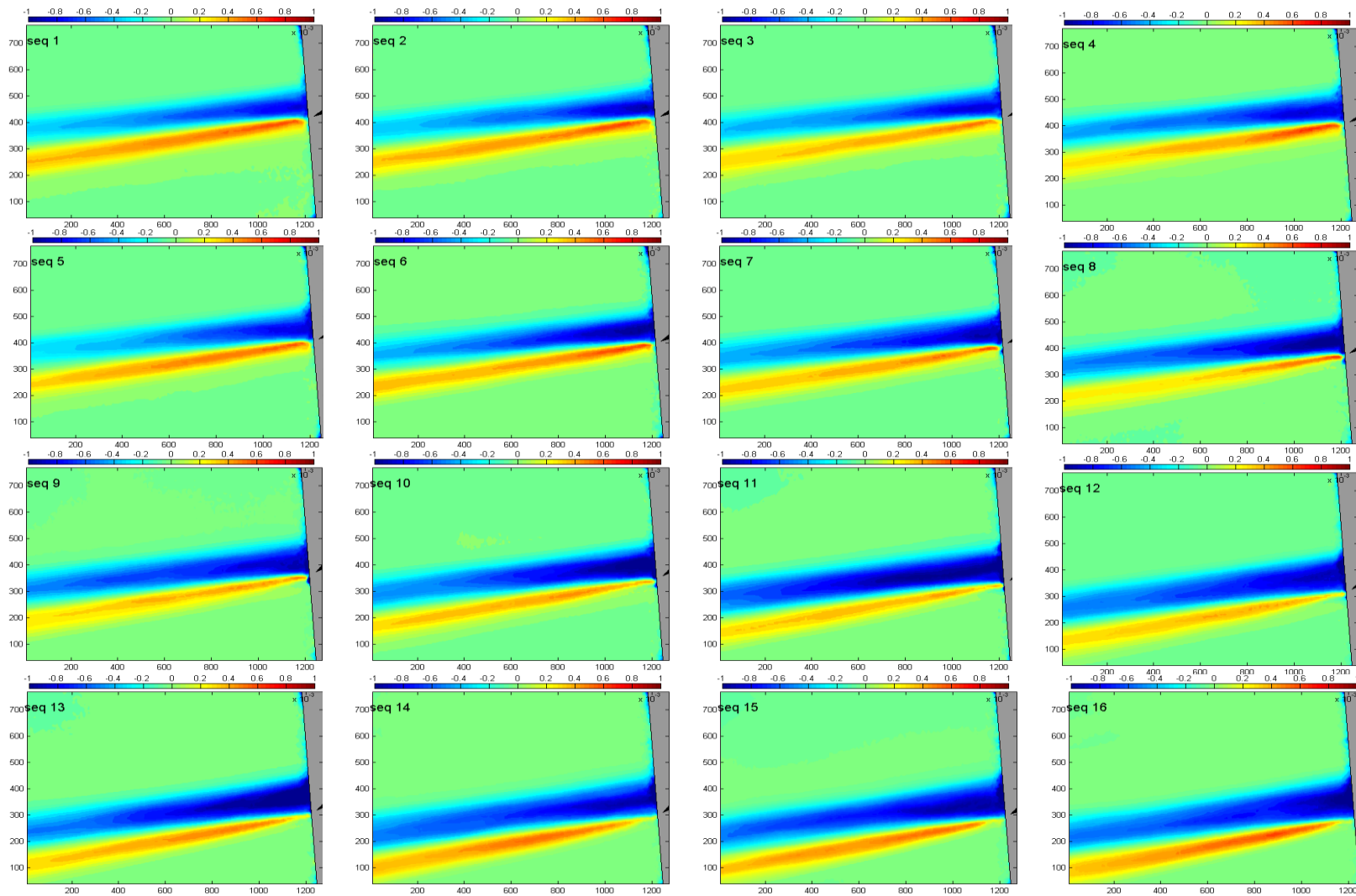
Figure 4.29: Comparison of $\langle \overline{uv} \rangle / U_\infty^2$ SMA actuation
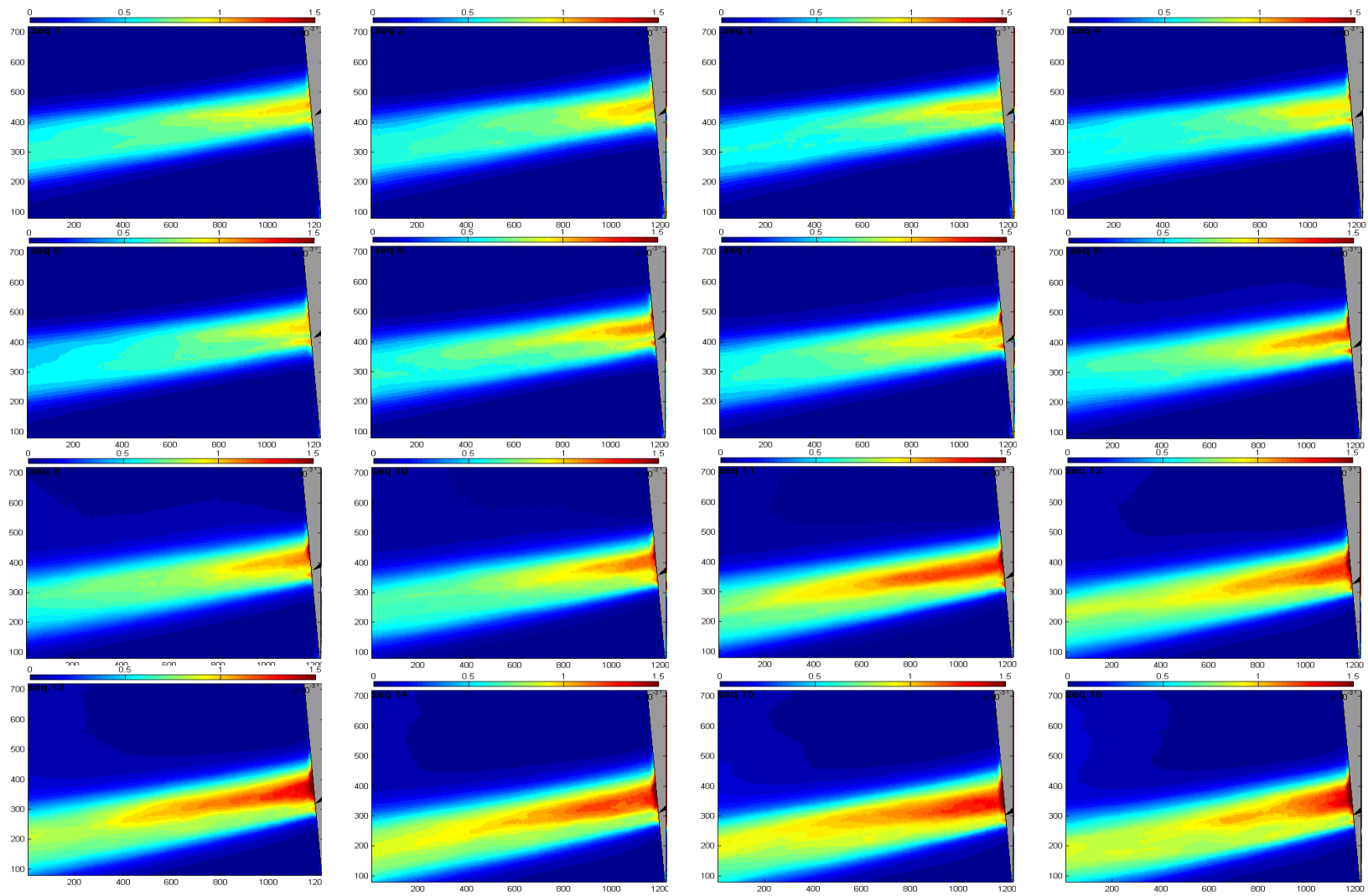
Figure 4.30: Comparison of $\langle \overline{v^2} \rangle / U_\infty^2$ SMA actuation
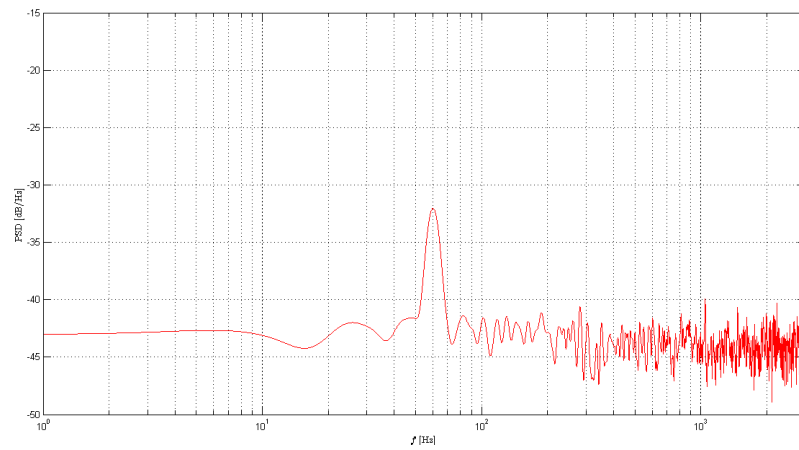
(a) Point 1
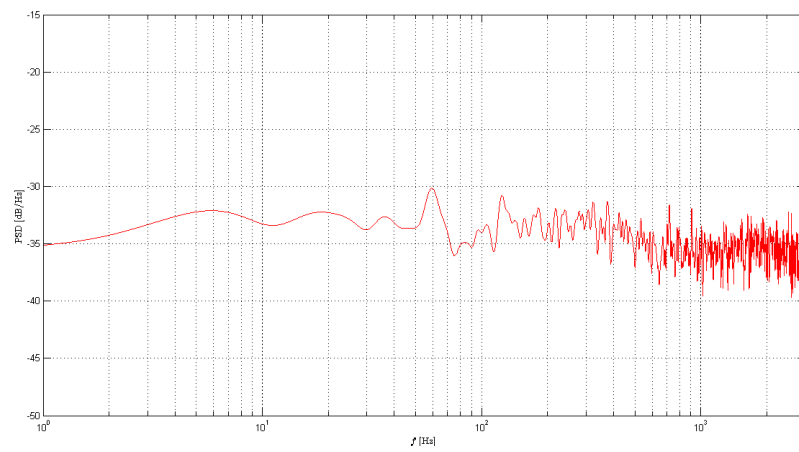
(b) Point 2
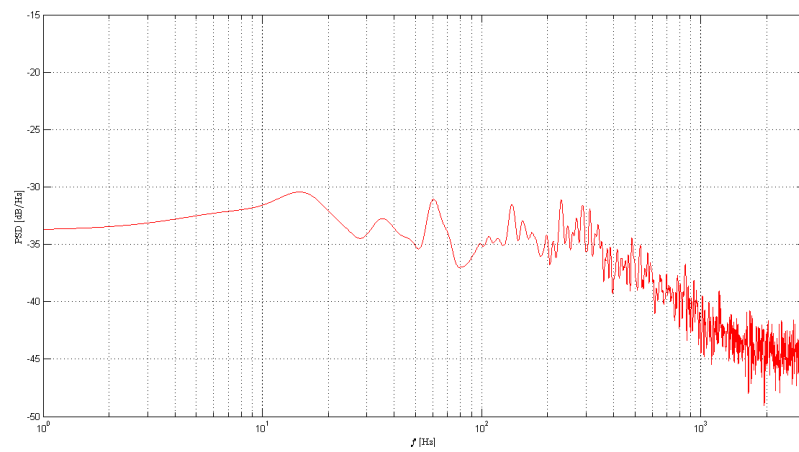
(c) Point 3

Figure 4.31: V velocity spectra 'Position 1'
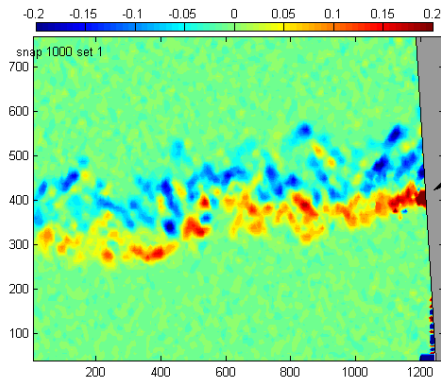
(a)Position 1
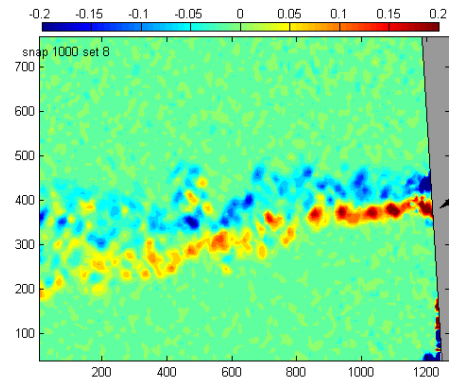
(b) Position 2
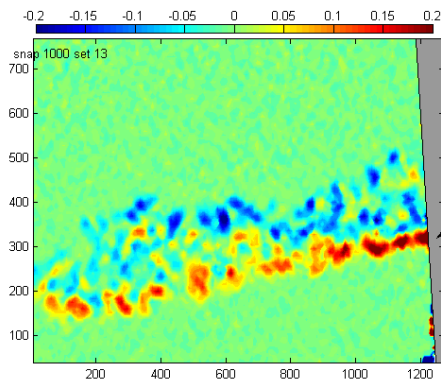
(c) Position 3
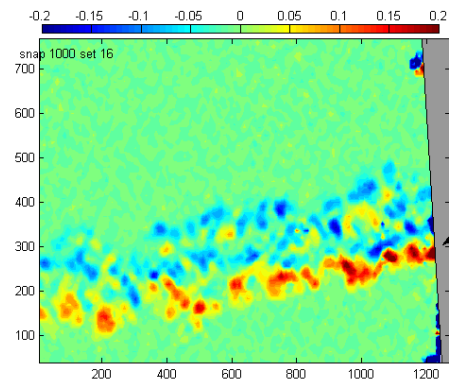
(d)Position 4

Figure 4.32: Vorticity field at the same instant for the four different position of the trailing edge

4.2.5 POD analysis

In this part, the behaviour of the flow at different trailing edge position is analysed using POD decomposition, in order to in depth analyse the propagation of coherent structure within the flow.
As descripted in the previous Chapter, the first two modes appears energetically uncoupled (see Figure 4.33), but in this case there isn't a clear link between the energy and the spatial representation of the modes. Furthermore no vortical structures can be observed into the flow. The spatial POD modes of the U velocity (Figure 4.34), clearly shows a shear-layer interaction especially for the intermediate positions. The energy level look similar for the first three position whereas for the last position it's a little bit lower.
This different behaviour, in respect of the previous results, can be explained considering that a larger deformation of the airfoil has a higher impact on the surrounding velocity field as can be seen comparing the U velocity spatial modes (see Figure 4.11 and Figure 4.34).

4.2.6 Conclusion

The goal of the result presented is to show the effect of a hybridization of high frequency piezoelectric actuation and a low-frequency SMA actuation mechanism integrated both in an airfoil prototype.
The actuation frequency of the trailing edge by piezoelectric clear impact on the variation of the local velocity field. As shown in the previous chapter the actuation frequency of 60 Hz leads to a reduction of the wake past the trailing edge and also a reduction of the Reynolds stresses components.
By exploiting this effect it might be possible to attenuate the high-frequency Kelvin-Helmholtz vortices which are the major source of noise and drag.
The results with respect to the large displacement low-frequency actuation shows the capacity of the hybrid airfoil to enable a real-time camber control in order to optimize the flight condition (lift and drag characteristics of the airfoil).
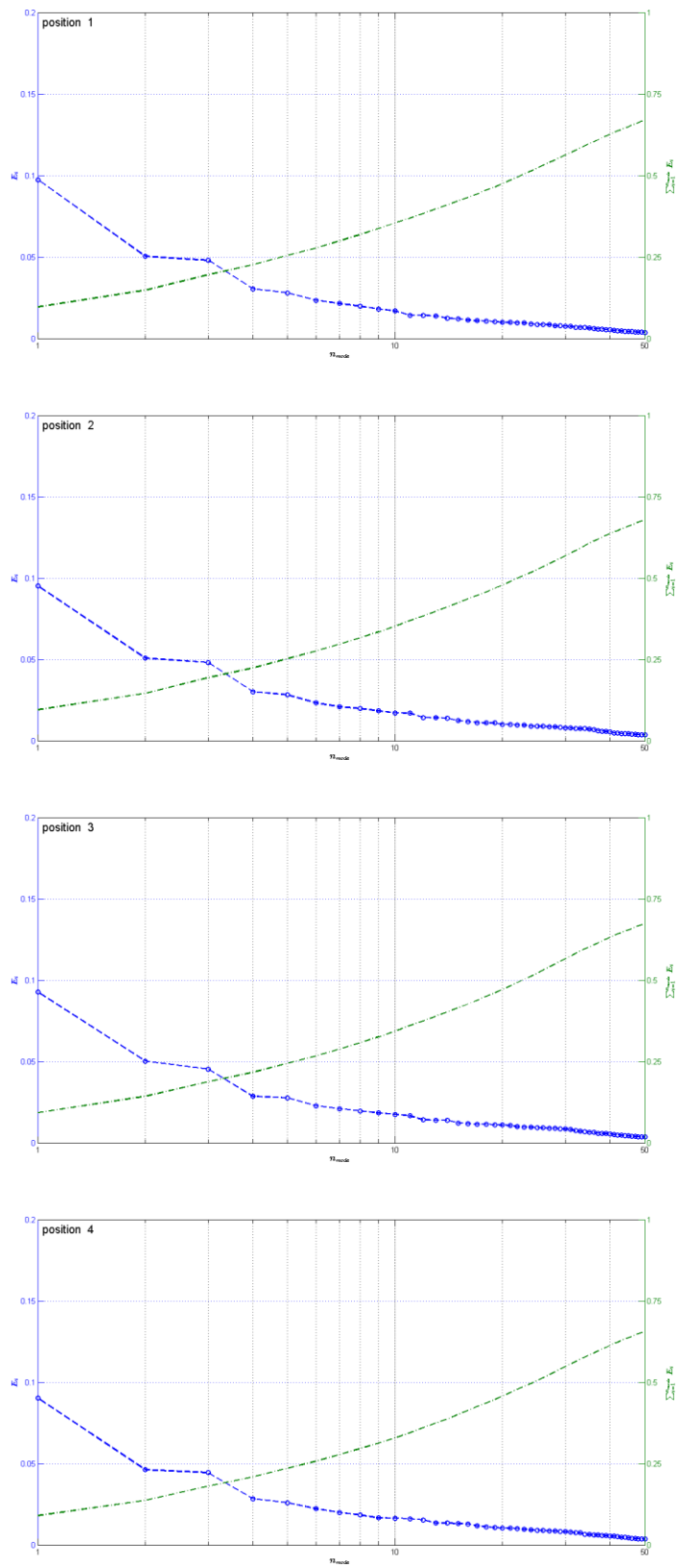
Figure 4.33: Energy of POD modes. Position '1' to '4' from top to bottom
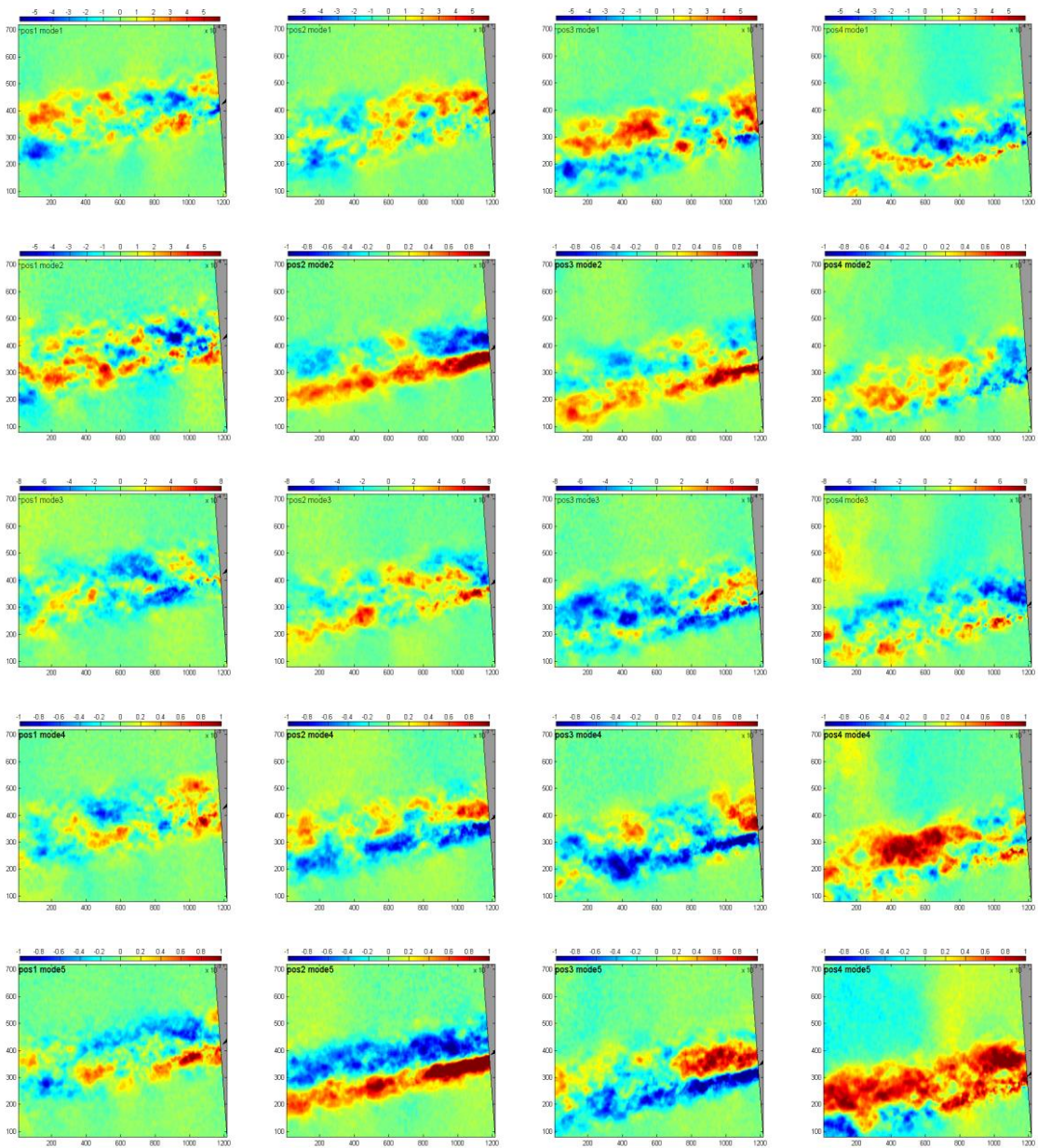
Figure 4.34: Comparing of the first five POD spatial U velocity modes (from top to bottom)

Conclusions

Throughout this thesis the validity of a prototype morphing wing via smart materials and the effect of this type of actuation on the flow at Reynolds number of about 200,000, that corresponds to a low-subsonic aileron's flight phase like landing, was investigated.

This hybrid prototype was studied associating SMAs and piezoelectric trailing edge actuators allowing a simultaneous large deformation at limited frequencies and high frequency vibrations to benefit the lift real-time control via SMAs, and reduction of the wake size using MFC actuators.

The effects of the trailing edge high frequency actuation (up to ≈100 Hz) on the turbulent structures has been examined in Chapter 4.1, and an optimum actuation frequency at 60 Hz has been identified.

The effect of piezoelectric actuation mechanism is clearly visible in the energy density spectra, with a reduction of the overall energy density up to 22 % and, and a reduction of the turbulent kinetic energy up to 16 %. These effects have been confirmed by proper orthogonal decomposition (POD) analysis that shows a modification of the spatial and temporal modes with the changing of the actuation frequency.

This allow reducing the shape drag up to 20 % as well as the pressure fluctuations associated to the aerodynamic noise downstream the trailing edge.

The camber deformation abilities of the low frequency SMAs actuation under realistic aerodynamic loads was demonstrated (Chapter 4.2). It was also shown the possibility to simultaneously actuate the prototype at low frequencies (order of ≈ 0.1 Hz by SMAs) and higher frequency vibration (order of ≈ 100 Hz by MFCs) in order to achieve a real time lift control and to influence the higher frequency aerodynamic phenomena, by comparing the phase-averaged dynamic and the time-averaged static positions. The POD analysis shows that a larger deformation of the airfoil has a higher impact on the surrounding velocity field.

In summary it can be said that the prototype morphing wing presented in this thesis allow to reduce the wake size, directly related to a reduction of the shape drag, as well as to reduce the overall energy density and turbulent kinetic energy, related to aerodynamic noise downstream the trailing edge. It also allow a real time control of the lift to drag ratio.

Future investigations aim to increase the prototype dimension in order to demonstrate the ability of SMA actuation in a real scale aerodynamic forces and to increase the Reynolds number up to a cruise flight phase.

Bibliography

J. Scheller, M. Chinaud, JF. Rouchon, E. Duhayon, S. Cazin, M. Marchal, M. Braza: Trailing-edge dynamics of a morphing NACA0012 aileron at high Reynolds number by high-speed PIV, Journal of Fluids and Structures, Volume 55, May 2015, Pages 42-51

J. Scheller, M. Chinaud, JF. Rouchon, E. Duhayon, S. Cazin, M. Marchal, M. Braza: Trailing-edge dynamics and morphing of a deformable flat plate at high Reynolds number by time-resolved PIV, Journal of Fluids and Structures, Volume 47, May 2014, Pages 41-54

P. J. Schmid, D. Violato, O. Pust, F. Scarano. Decomposition of time-resolved tomographic PIV. 15th International Symposium on Applications of Laser Techniques in Fluid Mechanics, Jul 2010, Lisbonne, Portugal. Instituto Superior Tecnico Center for Innovation, Technology and Policy Research, pp. 371, 2010

J. Scheller, K. Rizzo, G. Godin, E. Duhayon, JF. Rouchon, J. Hunt, M. Braza. Experimental investigation of the effect of high-frequency electroactive morphing on the shear-layer, 68th Annual Meeting of the APS Division of Fluid Dynamics Volume 60, Number 21Sunday–Tuesday, November 22–24, 2015; Boston, Massachusetts

Perrin, R., 2005. Analyse physique et modélisation d'écoulements incompressibles instationnaires turbulents autour d'un cylindre circulaire à grand nombre de reynolds. Ph.D. thesis

G. Berkooz, P. Holmes, J. L. Lumley: The proper orthogonal decomposition in the analysis of turbulent flows, Annual Review of Fluid Mechanics Vol. 25: 539-575 (Volume publication date January 1993)

S. Barbarino, O. Bilgen, R. M. Ajaj, M. I. Friswell, D. J. Inman: A Review of Morphing Aircraft, Journal of Intelligent Material Systems and Structures June 2011 vol. 22 no. 9823-877

S. Barbarino, E. I. Saavedra Flores, R. M. Ajaj, I. Dayyani, M. I. Friswell: A review on shape memory alloys with applications to morphing aircraft , Smart Materials and Structures, Volume 23, Number 6, April 2014

J. M. Jani, M. Leary, A. Subic , M. A. Gibson: A review of shape memory alloy research, applications and opportunities, Materials & Design, Volume 56, April 2014, Pages 1078-1113

G. Kerschen, J. Golinval, A. F. Vakakis, L. A. Bergman: The Method of Proper Orthogonal Decomposition for Dynamical Characterization and Order Reduction of Mechanical Systems: An Overview, Nonlinear dynamics, 2005-Springer

J. Scheller, K. Rizzo, G. Jodin, E. Duhayon, J.F. Rouchon, M. Braza: A hybrid morphing NACA4412 airfoil concept, Industrial Technology (ICIT), 2015 IEEE International Conference, March 2015, pp. 1974-1978

IEEE Standard on Piezoelectricity

R. Perrin, M. Braza, E. Cid, S. Cazin, A. Barthet, A. Sevrain, C. Mockett, F. Thiele: Obtaining phase averaged turbulence properties in the near wakeof a circular cylinder at high Reynolds number using POD, Experiments in Fluids, August 2007, Volume 43, Issue 2, pp 341-355

S. Prothin , H. Djeridi, J. Billard: Coherent and turbulent process analysis of the effects of a longitudinal vortex on boundary layer detachment on a NACA0015 foil, Journal of Fluids and Structures Volume 47, May 2014, Pages 2–20

E. Deri, M. Braza, E. Cid, S. Cazin, D. Michaelis, C. Degouet: Investigation of the three-dimensional turbulent near-wake structure past a flat plate by tomographic PIV at high Reynolds number, Journal of Fluids and Structures, Volume 47, May 2014, Pages 21–30

M. Chinaud, J.F.Rouchon, E.Duhayon, J.Scheller, S.Cazin, M. Marchal, M.Braza: Trailing-edge dynamics and morphing of a deformable flat plate at high Reynolds number by time-resolved PIV, Journal of Fluids and Structures, Volume 47, May 2014, Pages 41–54

D. Lengani, D. Simoni, M. Ubaldi, P. Zunino: POD analysis of the unsteady behaviour of a laminar separation bubble, Experimental Thermal and Fluid Science, Volume 58, October 2014, Pages 70–79

P. Holmes, J.L. Lumley, G. Berkooz, C.W. Rowley: Turbulence, Coherent Structures, Dynamical Systems and Symmetry, 2nd ed., Cambridge University Press, Cambridge, England, U.K., 2012, pp. 386

M. Raffel, C. E. Willert, S. T. Wereley, J. Kompenhans: Particle image velocimetry a practical guide-Springer 2007

J. Kostas, J. Soria, M. S. Chong: A comparison between snapshot POD analysis of PIV velocity and vorticity data, Experiments in Fluids, February 2005, Volume 38, Issue 2, pp 146-160

D. C. Lagoudas: Shape memory alloys, Springer 2008

Handbook of Experimental Fluid Mechanics, Springer 2007

N. Ursache, T. Melin, A. Isikveren, M. Friswell, Sep. 2007. Morphing Winglets for Aircraft Multi-Phase Improvement. In: 7th AIAA ATIO Conf, 2nd CEIAT Int'l Conf on Innov & Integr in Aero Sciences,17th LTA Systems Tech Conf; followed by 2nd TEOS Forum. Aviation Technology, Integration, and Operations (ATIO) Conferences. American Institute of Aeronautics and Astronautics

L. Sirovich. Turbulence and the dynamics of coherent structures. I—III. Quart. Appl. Math., 45(3):561–590, 1987.

D. Lengani, D. Simoni: Recognition of coherent structures in the boundary layer of a low-pressure-turbine blade for different free-stream turbulence intensity levels. International Journal of Heat and Fluid Flow, 2015, pp. 1-13

Appendix

POD script

```
%% Script calculate SNAPSHOT MATRIX and POD MODEs


%% snapshot matrix
xrange = 1:160;
yrange = 1:100;
dt = 1.66e-4; % [s] delta t
dx = 6950; % [pixel] --> [m] delta x
POD_nModes = 50; % number of POD modes
nj = size(U,1);
ni = size(U,2);
ns = size(U,3);% number of snapshots
x = x./(dx*10^-3); % [mm]
y = y./(dx*10^-3); % [mm]
u = mean(U,3); % mean velocity
v = mean(V,3); % mean velocity
mU = -(u*calib_factor)'; % U mean [m/s]
mV = (v*calib_factor)'; % V mean [m/s]


uv_all = zeros(2*ni*nj,ns); % snapshot matrix
 for i=1:ns;
    A = calib_factor*(-(U(:,:,i)-u)');
```

```matlab
    B = calib_factor*((V(:,:,i)-v)');

    uv_all(:,i) = single([reshape(A,ni*nj,1);reshape(B,ni*nj,1)]);

  end;


%% calculate the  Proper Orthogonal Decomposition


N = size(uv_all,2);

phi = zeros(size(uv_all,1),POD_nModes);

autocorr= (1/N)*single(uv_all'*uv_all); % Autocovariance matrix


[eV,D] = eig(autocorr); % diagonal matrix D eigenvalue,full matrix eV columns are the corresponding eigenvectors

[L,I] = sort(diag(D)); % sort eigenvalues in ascending order


eVector = eV(:,flipud(I));

eValue = L(flipud(I));% Eigenvalues sorted in descending order

eValue(length(eValue)) = 0;% last eigenvalue should be zero


energy = eValue/sum(eValue); % relative energy associated with mode m

energy_cum = zeros(size(energy)); % energy sum


  for i=1:POD_nModes

    tmp = uv_all*eVector(:,i); % find spatial mode mode m

    phi(:,i) = tmp/norm(tmp); % normalize spatial mode mode

    energy_cum(i) = sum(energy(1:i));

  end

lam = phi'*uv_all; % temporal mode
```